Modélisation mathématiques de l'activité de la mitochondrie cardiaque

Bachar Tarraf

université de BORDEAUX

THÈSE PRÉSENTÉE

POUR OBTENIR LE GRADE DE

DOCTEUR
DE L'UNIVERSITÉ DE BORDEAUX

ECOLE DOCTORALE MATHÉMATIQUES ET INFORMATIQUES

Par **Bachar TARRAF**

Modélisation mathématiques de l'activité de la mitochondrie cardiaque

Sous la direction de : **Yves COUDIÈRE**
Co-directeur : **Michael LEGUÈBE**

Date de soutenance: 02 février 2022

Membres du jury :

Mme. Frédérique CLÉMENT	Directrice de Recherche	Inria de Saclay	Rapporteuse
M. Thomas LEPOUTRE	Chargé de Recherche	Inria Rhone Alpes	Rapporteur
Mme. Magali RIBOT	Professeur des Universités	Université d'Orléans	Présidente du jury
M. Stéphane ARBAULT	Directeur de Recherche	CNRS	Examinateur
M. Yves COUDIÈRE	Professeur des Universités	Université de Bordeaux	Directeur
M. Michael LEGUÈBE	Chargé de Recherche	Inria Bordeaux	Directeur

Titre : Modélisation mathématiques de l'activité de la mitochondrie cardiaque

Résumé :

Les mitochondries cardiaques sont des organites intracellulaires qui ont de nombreux rôles cruciaux, notamment le métabolisme énergétique et la régulation du calcium cellulaire. Elles sont ainsi liées au cycle d'excitation-contraction de la cellule cardiaque. Un grand nombre de modèles mathématiques ont été proposés pour mieux comprendre la dynamique mitochondriale cardiaque, mais ils montrent généralement un haut niveau de complexité, et leurs paramètres sont très difficiles à recaler aux données expérimentales.

Dans ce travail, nous écrivons d'abord un modèle, qui inclut les mécanismes mitochondriaux de base, basé sur des principes thermodynamiques de transduction d'énergie libre et des résultats de la littérature. Nous proposons des expressions simples pour les réactions et les échanges ioniques gérés par la mitochondrie, qui permettent de réduire le nombre de paramètres au minimum. A partir de données expérimentales de respiration mitochondriale, nous procédons à une analyse de sensibilité globale sur les paramètres du modèle afin de quantifier leur influence sur la sortie du modèle. Les paramètres influents sont ensuite recalés à l'aide d'un algorithme génétique. Les résultats montrent que le modèle est capable de reproduire les taux de respiration des mitochondries avec une très faible variabilité des paramètres entre les différentes expériences.

Dans une seconde partie, nous incorporons au modèle un mécanisme complexe connu sous le nom de pore de transition de perméabilité mitochondriale (mPTP). Le fonctionnement de ce pore est mal connu de nos jours et on pense qu'il peut se comporter physiologiquement ou pathologiquement en fonction de son état d'ouverture. Ensuite, comme l'évaluation du modèle est coûteuse, nous utilisons un algorithme de classification supervisé par apprentissage automatique pour construire un méta-modèle capable de caractériser la sortie du modèle sans l'évaluer. Nous utilisons ensuite ce méta-modèle pour effectuer une inférence de paramètres à l'aide d'un algorithme itératif à maximum de vraisemblance. En utilisant des données expérimentales sur le type d'ouverture du mPTP, nous calculons des distributions statistiques adéquates pour certains des paramètres du modèle.

Dans l'ensemble, l'utilité d'un tel modèle en soi est qu'il peut être utilisé pour faire des prédictions de mécanismes d'intérêt liés à la respiration mitochondriale, ou encore pour effectuer des simulations de quelques expériences d'intérêt irréalisables. Le modèle garantit, au moins qualitativement, la capacité de représenter la population de mitochondries cardiaques. Il pourrait également être intéressant d'intégrer à terme ce modèle aux modèles d'excitation-contraction cardiaque. En effet, le modèle potentiel pourrait permettre d'explorer l'implication de ROS mitochondriaux et mPTP dans la régulation du couplage excitation-contraction en cardiomyocytes, dans des conditions physiologiques et pathologiques.

Mots clés : Modélisation biologique, mitochondries, équations différentielles ordinaires, estimation des paramètres, analyse de sensibilité, validation expérimentale, classification

Title : Mathematical modeling of the cardiac mitochondrial activity

Abstract :

Cardiac mitochondria are intracellular organelles that have many crucial roles, including energy metabolism and cellular calcium regulation. They are thus linked to the excitation-contraction cycle of the heart cell. A large number of mathematical models have been proposed to better understand the cardiac mitochondrial dynamics, but they generally show a high level of complexity, and their parameters are very hard to fit to experimental data.

In this work, we first derive a model, that includes the basic mitochondrial mechanisms, based on thermodynamics free energy-transduction principles and results from the literature. We propose simple expressions for the mitochondrial regulated ionic exchanges and reaction rates, that allow reducing the number of parameters to a minimum. Using experimental data of mitochondrial respiration, we proceed with global sensitivity analysis on the model parameters in order to quantify their influence on the output of the model. The influential parameters are then calibrated using a genetic algorithm. Results show that the model is able to reproduce respiration rates of mitochondria with very low variability of the parameters between the different experiments.

In a second part, we incorporate into the model a complex mechanism known as the mitochondrial permeability transition pore (mPTP). The functioning of this pore is poorly understood to our days and is thought to behave either physiologically or pathologically depending on its opening state. Next, since a model evaluation is time-consuming, we use a machine learning supervised classification algorithm to build a meta-model that is able to classify the output of the model without evaluating it. We then use this meta-model to perform parameter inference using a maximum likelihood iterative algorithm. Using experimental data on the mPTP opening type, we compute adequate statistical distributions for some of the parameters of the model.

Overall, the utility of such a model in itself is that it can be used to make predictions of mechanisms of interest related to mitochondrial respiration, or even to perform simulations of some unfeasible experiments of interest. The model guarantees, at least qualitatively, the ability to represent population of cardiac mitochondria. It could also be interesting to eventually incorporate this model into cardiac excitation-contraction models. That is because the potential model could make it possible to explore the involvement of mitochondrial ROS and mPTP in the regulation of the excitation-contraction coupling in cardiomyocytes, under physiological and pathological conditions.

Keywords : Biological modeling, mitochondria, ordinary differential equations, parameter estimation, sensitivity analysis, experimental validation, classification

Remerciements

Premièrement, je tiens à remercier mes deux directeurs de thèse, Michael Leguèbe et Yves Coudière, pour leur accompagnement durant ces trois années. J'ai trop apprécié vos conseils et vos encouragements tout au long de ma thèse, et surtout dans les moments de doutes. J'ai été extrêmement chanceux d'avoir des encadrants qui s'intéressent à mon travail et qui répondent à mes questions si rapidement.

Je voudrais aussi remercier énormément tous les membres de l'équipe CARMEN pour le bon accueil et l'ambiance sympa. Même si je vais pas pouvoir vous mentionner tous dans cette petite section de remerciements, sachez que je porte que du respect et d'amitié pour vous.

Je commencerai par Niami la nouvelle doctorante libanaise de l'équipe (qui va d'ailleurs me piquer le bureau et le drapeau libanais à mon départ). Même si elle est arrivée à l'équipe quand j'étais en fin de ma deuxième année, on s'est très rapidement devenue des très proches amis. Pas besoin que je détaille pourquoi je te remercie, t'en connais bien!

Je voudrais aussi remercier les autres membres de CARMEN qui sont devenue, pour moi, beaucoup plus que juste des collègues. En particulier, l'ancien trio Pauline, Mehdi et Amal, merci tout d'abord pour le bon accueil, l'agréable ambiance, et aussi pour les belles soirées pizza/bières en ville qu'on faisait de temps en temps. Un grand merci aussi pour le nouveau trio Narimane, Andony et Oumayma avec qui j'ai passé des magnifiques jours, durant ces dernières trois années, dans l'open space (avec le ballon d'Andony, les bêtises de Narimane et les horaires de Oumayma :')) mais aussi ailleurs. Sans oublier bien sûr Malal le post-doctorant brillant de l'équipe que je respecte beaucoup. Franchement, chaqu'un entre vous possède un caractère et une personnalité géniale qui m'a marqué et que je n'oublierai jamais.

Je finis par remercier ma famille au Liban: mes chers parents, ma sœur, et mon frère. Je vous remercie pour votre soutien, votre amour inconditionnel et d'avoir fait de moi la personne que je suis aujourd'hui. Mes amis ou bien la famille libanaise en France: David et Sam. Merci énormément pour votre soutien et surtout pour les soirées "SikoMiko"!

'Le succès n'est pas final. L'échec n'est pas fatal. C'est le courage de continuer qui compte.'

Winston Churchill

List of notations and abbreviations

Ca^{2+}	Calcium cation
Mg^{2+}	Magnesium
Mn^{2+}	Manganese(II)
Sr^{2+}	Strontium
SR	Sarcoplasmic reticulum
ER	Endoplasmic reticulum
ADP	Adenosine diphosphate
ATP	Adenosine triphosphate
Na^{+}	Sodium cation
mPTP	Mitochondrial permeability transition pore
ROS	Reactive oxygen species
NAD	Nicotinamide adenine dinucleotide
NAD^{+}	Oxidized form of NAD
NADH	Reduced form of NAD
FAD	Flavin adenine dinucleotide
$FADH_2$	Reduced form of FAD
ETC	Electron transport chain
PDH	Pyruvate dehydrogenase enzyme
ANT	Adenine nucleotide translocator
CVDs	Cardiovascular diseases
$O_2.^{-}$	Superoxide anion
Pi	Inorganic phosphate
CypD	Cyclophilin D
CsA	Cyclosporine A
TCA	Tricarboxylic acid
TMRM	Fluorescent dye tetramethylrhodamine methyl ester
EGTA	Egtazic acid

Contents

Chapter 1

Introduction

Contents

Cardiovascular diseases (CVDs) account for 29 % of deaths in the whole world. In the year 2019, an estimated number of 18.6 million people lost their lives due to CVDs. Unfortunately, this mortality number seems to be growing each year. One of most famous types of CVDs is heart failure, which means a heart unable to pump blood around the body properly. Heart failure is often the consequence of electrical heart diseases. Before moving to the electrical activity of the heart, and to its relation with the motivation behind this thesis, we will introduce some notions about the anatomy of heart and the cardiac cell.

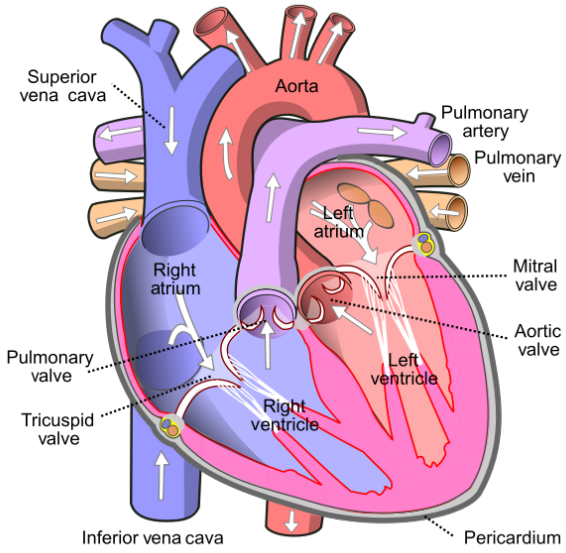

Figure 1.1: Illustration of the heart anatomy. Source: wikipedia.

1.1 Anatomy of the heart

The heart has four chambers: two upper chambers called the left and right atrium, and two lower chambers called the left and right ventricles (Fig. 1.1). The left and right parts of the heart are separated by a wall of muscle called septum. The right atrium collects the blood that has traveled through the body then expels it to the right ventricle which will then eject it towards the lungs. The left atrium collects blood from the lungs and sends it to the left ventricle which ejects the freshly oxygenated blood to the organs. The myocardium, which forms the wall of the heart, is made up of elongated cardiac muscle cells called **cardiomyocytes**. These are organized in fibers that superimpose, forming layers. The internal part of these layers is called the endocardium, and the external part is called the epicardium.

1.2 The cardiac muscle cells

Cardiac muscle cells, also known as cardiomyocytes, are the cells that make the heart muscle. These cells are able to shorten and lengthen their fibers, which is essential during a heart beat. The main difference between cardiac muscle and skeletal muscle is that the former exhibits

rhythmic involuntary contractions, which eventually leads the heart to continuously bump. For this reason cardiac cells need big quantities of energy.

As all the other type of cells in the body, cardiomyocytes contain intracellular organelles that insure their correct functioning. First of all, we have the cellular membrane, which is called the **sarcolemma** or also myolemma. This membrane has transverse tubules **T-tubules**, which are invaginations into the myocytes, that form a barrier between the extracellular and the intracellular spaces. Additionally, inside the cardiac cell, we have :

- one or more (up to four [58]) nucleus.
- the **sarcoplasmic reticulum**, usually abbreviated by SR, is the organelle that stores the most important reserve of calcium inside the cardiomyocyte. It pumps them out into the cytosol when the muscle fiber is stimulated.
- **the mitochondria**, usually represent 30% of the cellular volume, are often called "the power house of the cell". Besides producing ATP which is the energy currency of the cell, they actively participate in the ionic exchanges (in particular calcium) with the extra mitochondria medium. Cardiomyocytes contain many more mitochondria than other cell types in order to generate the needed energy for rhythmic contractions.
- the **myofibrils**, that constitute up to 60% of the cell volume, are composed of large number of **myofilaments**. These myofilaments repeat along the length of the myofibrils in sections called **sarcomeres**. Myosin and actin are the two most important proteins within sacromeres. Myosin has a long globular head that can bind to actin, but also to ATP, which is the source energy of muscle movement. Each sarcomere is delimited by two **Z-disc**. Actin are bound to the Z-disc. It is the shortening of these units that permit the contraction of the muscle. In fact, it is the complex interplay between ATP, myosin and actin, that causes a contraction.

The primary function of the cardiac cell is to contract periodically. This is a complex process regulated by calcium and triggered by electrical impulses.

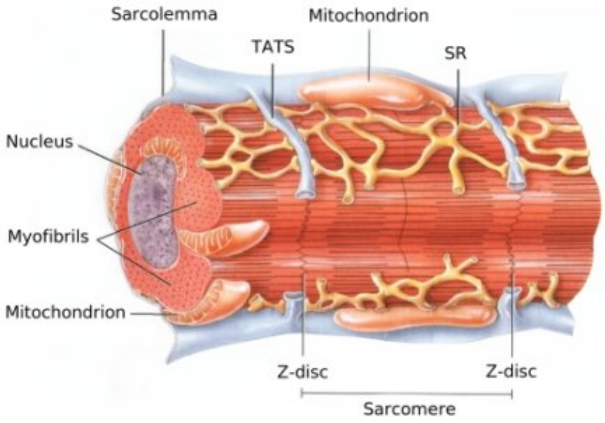

Figure 1.2: Illustration of a cardiomyocyte. Source: [73].

1.2.1 Excitation-contraction cycle

The excitation-contraction coupling of the cardiac cells is the process from electrical excitation of the myocyte to the contraction of the heart. The main stimulator is calcium, which is a direct activator of the myofilaments, that cause contraction.

First, the process starts with an electric action potential initiated by the sinoatrial node, which is a group of cells located in right atrium. The action potential propagates from one cell to another through gap junctions, leading to a synchronized depolarization of their membranes. When a cell sees an action potential, calcium then enters the cell, from the extracellular medium, through specific calcium channels. This entry triggers calcium release from the SR into the cytosol. This combination of mechanisms raises the amount of available calcium in the cytoplasm, that will then bind to the myofilaments to start the contraction process. In fact, calcium binding to myofilaments moves the troponin complex, which is a protein complex that makes muscle cells sensitive to calcium, away from the actin binding site. This removal frees the actin to be bound by myosin and initiates contraction. Indeed, the myosin head binds to ATP and pulls the actin filaments toward the center of the sarcomere, leading to the muscle contraction.

Second, the free calcium amount in the cytosol must decline in order for the relaxation to occur. This is done through several mechanisms such as SR Ca^{2+}-ATPase, sarcolemmal Na^{+}/Ca^{2+}exchange, sarcolemmal Ca^{2+}-ATPase and mitochondrial Ca^{2+}uniport.

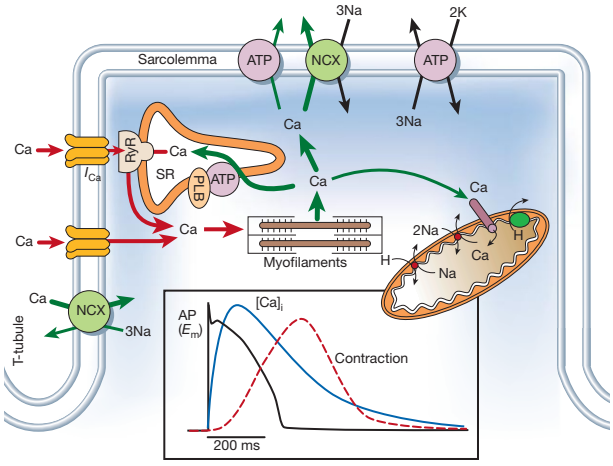

Figure 1.3: The opening of potential-sensitive channels in the sacrolemma triggers the contraction (red arrows). $Ca^{2+}$is then released from the SR and subsequentially activating the myofibrils. Relaxation (green arrows) follows the decrease of calcium concentration in the cytosol due to several mechanisms. Figure is taken from [4].

.

1.2.2 Role of mitochondria in the excitation-contraction coupling of the cardiomyocyte

Cardiac mitochondria are cell organelles that generate most of the energy needed for the cell contraction. This is by being the principle producer of adenine triphosphate (ATP) molecules through a process named oxidative phosphorylation.

Mitochondria are also considered one of several components that actively contribute in the regulation of the calcium cycle in the cardiomyocyte. This is done either through specific calcium ion carrier or exchanger (i.e calcium uniporter and calcium sodium exchanger), or through a non specific one such as the mitochondria permeability transition pore (mPTP). Details of the mitochondria functioning will be explained in the section 1.5.2.

1.3 Motivation

Up to this point, we see that mitochondria have an important role in the excitation-contraction coupling of the cardiomyocyte. This is due either to its contribution to the cellular Ca^{2+}cycle,

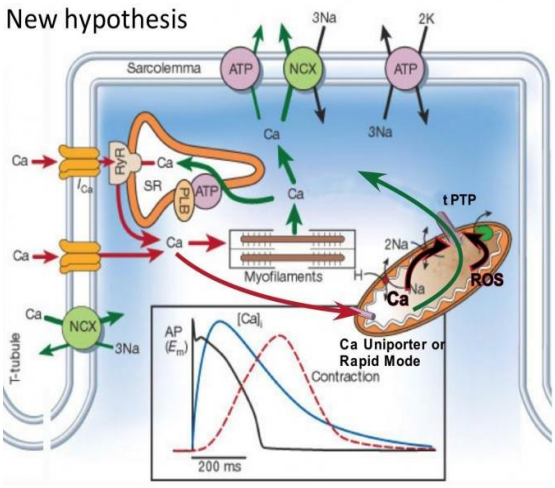

Figure 1.4: New hypothesis for the regulation of cardiac mitochondrial calcium handling. The figure is adapted from the work of Bers, D.M. et al nature 2002 [4].

or to the energy demand-supply of the cell. During a heart failure, the Ca^{2+}cycle and the energy demand-supply are both disrupted [36, 56]. In fact, several hallmarks of heart failure may be related to mitochondrial physiology and/or pathology such as: energy deficit, a defect in the excitation-contraction coupling and intracellular perturbation of calcium homeostasis. Additionaly, mitochondrial calcium overload has been claimed to have an important pathological role in heart failure [56]. The mitochondrial permeability transition pore (mPTP) is thought to be a key player, yet a poorly understood, mechanism of Ca^{2+}exchange between the mitochondria and the cell. In fact the opening of this pore is believed to have two operating modes (a physiological one and a pathological one). The pathological opening of this pore causes respiratory uncoupling, mitochondrial injury, and cell death as has been demonstrated during ischemia-reperfusion injury [19, 48]. These openings are known to be sensitive to the reactive oxygen species (ROS) [11, 39], produced also by the mitochondria. In addition, a new hypothesis for the regulation of cardiac mitochondrial calcium handling was proposed recently [22, 23]. It states that a parallel activation, by calcium, of the cardiac mitochondria occurs in the contraction phase (Fig. 1.4). This means that during contraction, in response to the high energy demand by the cardiac cell, cytoplasmic calcium enters the mitochondria and activates it in order to supply the cell with the needed energy. In the relaxation phase, this hypothesis, suggests that the

decrease in ATP demand by the cardiomyocyte causes an increase in ROS production by the respiratory chain, which stimulates mPTP opening and Ca^{2+}release from mitochondria.

The cardiac pathologies related to the dysfunction of the mitochondria, as well the biological assumptions related to its exact role in calcium signaling, make it clear that further understanding of the mitochondria is needed. But a legitimate question might be: how could developing a model of the cardiac mitochondria helps us understand more? The answer is simple, yet the procedure is a little bit long to achieve. In fact, cardiac ionic models do exist in the literature (such as Mitchell-Schaeffer [55] or Ten Tuscher-Panvilov [72]), but do not account explicitly for the mitochondrial activity. A starting point could be to develop a mathematical model that accounts for the biological features in question (such as mPTP and ROS), then to integrate it in a full ionic model and eventually try to understand the contribution of the mitochondria to some mechanisms of interest (such as calcium cycle and/or excitation contraction coupling).

However, since the different mitochondrial functions are coupled one to another (see sec. 1.5.2), modeling their activity is not trivial and usually results in complex models. A collection of mathematical models have been proposed to better understand this activity. Most of these models show a high level of complexity in terms of number of parameters and equations (see sec. 2). This is because they are generally developed following a cumulative approach. This complexity is not compatible with the inverse problem calibration techniques that can be used to validate the models with respect to data.

1.4 Overview of the thesis

In this thesis, my work is separated in two parts. The first part consists in developing a new model of cardiac mitochondria, that accounts for for the basic known mechanisms, and that has a number of parameters small enough to be fitted with available experimental data. The derivation of a simple model is motivated by the deciphering of the interplay between intra-cellular calcium dynamics, mitochondria and cardiac electrophysiology. To this aim, we need a model simple enough to be coupled to existing cardiac ionic models. Indeed, performing simulations at the tissue scale, requires storing information on the ionic state at several hundred thousands of

locations. So using a complex mitochondrial model, with dozens of state variables, would significantly increase the computational cost of the simulations. Therefore, there is interest in developing simple models that can yet reproduce the biological phenomena of interest. The mitochondrial activity can be described through ionic fluxes and reactions. These are modeled through expressions describing the ionic exchanges between the mitochondria and the cytosol or reactions that happen inside the mitochondria.

In the first part, we first had to revisit each flux expressions starting from the original work of Hill [35], which has been the base of the work of Magnus & Keizer [51], and most of the subsequent mitochondrial models in the literature. We then simplified these expressions by surface fitting to simpler analytical expressions (sec. 3.3). Additionally, we performed a two step global sensitivity analysis (sec. 4.2, and 4.4) on the parameters of the new model, to eliminate uninfluential parameters. In the final step, using the results from the sensitivity analysis, we calibrated the influential parameters to experimental data, using an optimization algorithm. Finally, the calibrated model was also tested on a new experimental data set for validation.

In the second part, we added two key state variables (mPTP and ROS) and their associated mechanisms to our model. The different types of the output of our model, in relation with the mPTP opening, were compared statistically to experimental observations from the work of Camille Colin [16]. In this part, in addition to performing sensitivity analysis, we used Machine Learning classification algorithms to build meta-models that are able sort the output of the model without the need of evaluating the original model (sec. 7.3.2). This was helpful for the exploration of a large high dimensional space of parameters, without accounting for the computational burden of evaluating the model. We were then able to compute the statistical distributions of the parameters, using statistical inference methods, to conclude with a range intervals of parameters were possible observed types are likely to occur.

1.5 Mitochondria structure and functioning

1.5.1 Structure

Mitochondria are organelles that are found in most eukaryotic cells. We can find up to 5000 mitochondrion per a cardiac cell. Their length generally ranges between 0.75 and 3 μm. They are semi autonomous organelles, meaning that they have a genetic heritage and capable of dividing independently of the cell. These characteristics were the first elements in support of the endosymbiotic theory, which supposes that intracellular mitochondria come from the incorporation of the cell by a certain bacteria with which it has maintained an endosymbiotic relationship. Mitochondria have a double layer membrane (**inner membrane, and outer membrane**). The two layers partition the organelle into four compartments (**the outer membrane**, **the intermembrane space**, **the inner membrane**, and **the matrix**) (Fig. 1.5). The outer membrane contains proteins-based pores (porins) that allow the movements of small ions and molecules, in two directions (inwards and outwards). The intermembrane space contains a protein that plays a role in mitochondrial energetics, that is the cytochrome c. In contrast to the outer membrane, the inner membrane is impermeable and most of ionic transfers are achieved via specific transporters or channels. The inner membrane is arranged into **cristae**, which are folds that increase the available surface. The matrix of the mitochondria contains its DNA, RNA, ribosomes, calcium granules, and enzymes of the tricarboxylic acid (TCA) cycle (also known as the citric acid cycle, or Krebs cycle), which metabolizes nutrients into products that mitochondria use for energy production.

1.5.2 Functioning

The primary function of mitochondria is to produce large quantities of ATP molecules. The process of ATP creation consists in several main stages. The chemical reactions in most of these stages happen with the help of specific enzymes localized in the inner mitochondrial membrane. Nevertheless, the first stage of metabolism begins in the cytoplasm, with substrate metabolization. The next steps including the electron transport chain, oxidative phosphory-

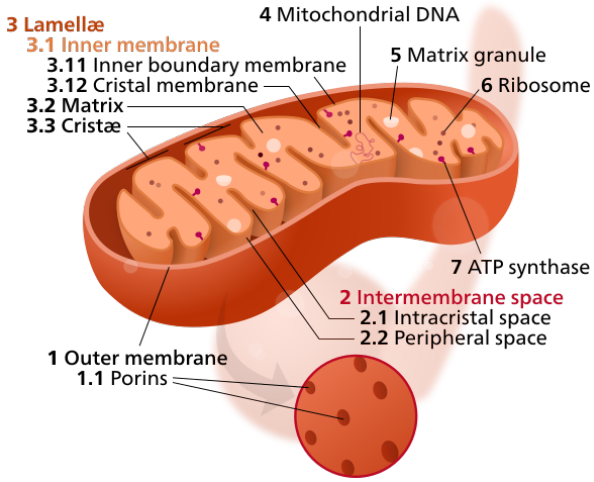

Figure 1.5: Composition of a classical mitochondrion. Source: wikipedia

lation, and proton leakage (sec. 1.5.2.2, and 1.5.2.3) occur inside the mitochondria or in the inner mitochondrial membrane. We should note that here we evoke only the principal mechanisms convenient to our modeling purpose. However the mitochondria have more complex and specific mechanisms that wont be discussed in this manuscript.

1.5.2.1 From glucose to NADH

The mitochondria need their "fuel", to be able to work correctly. This "fuel" is glucose. In the cytoplasm the glucose is metabolized into a primary product: pyruvate. Then, pyruvate enters the mitochondria through a carrier, where it is processed by the Krebs cycle, which is a series of complex chemical reactions, resulting mainly in the production of the reducing agent nicotinamide adenine dinucleotide (NADH). This agent is crucial in the next stages, in particular in the electron transport chain that will be explained in the next section.

1.5.2.2 Respiratory chain

The respiratory chain is a series of chemical reactions catalyzed by enzymatic complexes (complex I ,II,III, and IV) that are binded to the inner mitochondrial membrane. The respiratory chain couples the oxidation of NADH, from the electron transport chain (ETC), to the transformation of ADP to ATP, through a reaction called oxidative phosphorylation.

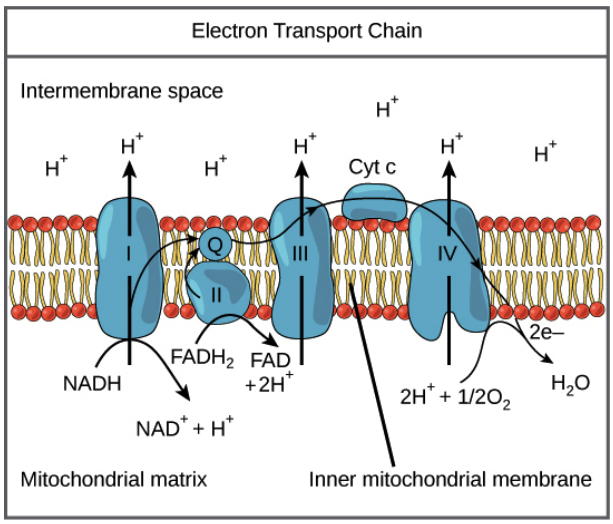

Figure 1.6: Scheme of the electron transport chain. Source: https://courses.lumenlearning.com

1.5.2.2.1 Electron transport chain (ETC) The ETC is a series of redox reactions, where electrons are passed from one component to another, to the endpoint of the chain where the electrons reduce molecular oxygen, producing water (Fig. 1.6). The ETC starts with the delivery of electrons by NADH and $FADH_2$, which are reduced electron carriers produced from previous steps of the respiratory chain (such as substrate metabolization). In the process, these two electron carriers turn back into NAD^+ and FAD. The electron transfer through the ETC is coupled with energy release that takes the form of proton pumps at complex I,III, and IV. $FADH_2$ is known to be a less good electron donor than NADH, meaning that its electrons are at lower energy level. For this reason it contributes significantly less than NADH in the proton pumps. In this manuscript, we will only consider NADH whenever ETC is discussed. The oxidation of NADH involves the transfer of two electrons through the ETC. The oxidation-reduction equation resulting from NADH oxidation is given by:

$$\mathrm{NADH} + \mathrm{H}^+ + \frac{1}{2}\mathrm{O}_2 \longrightarrow \mathrm{NAD}^+ + \mathrm{H}_2\mathrm{O}.$$

Actually, this equation summarizes three other reactions (occurring at complexes I,III, and IV) where protons are pumped, since the oxidation of NADH involves the previous three complexes. During this reaction, oxygen is consumed. Indeed, oxygen consumption is an important

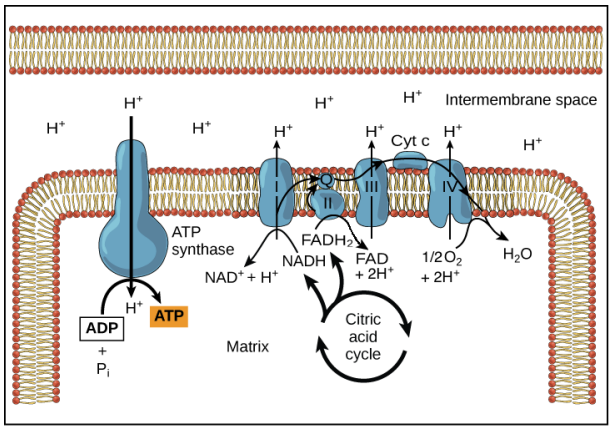

Figure 1.7: Schematic of the use of the proton gradient, pumped from the ETC, with the help of ATP-synthase to create ATP.Source: https://courses.lumenlearning.com

measure studied extensively in mitochondrial experiments. That is because it reflects the working state of the mitochondria. A significant part of the experimental data used in this thesis is somehow related to this measure (see sec. 3.5).

1.5.2.2.2 Oxidative phosphorylation The ETC creates a proton gradient across the inner mitochondrial membrane, with higher concentration of H^+ in the intermembrane space than in the matrix. This gradient, that is called sometimes proton-motive force, can be seen as a stored form of energy that is used in the synthesis of ATP. The phospholipid bilayer of the inner mitochondrial membrane prevents the pumped protons from entering the matrix. Instead, this protons move down their concentration gradient with the help of the ATP-synthase protein. The ATP-synthase catalyses the addition of a phosphate to ADP, using the energy from the proton gradient, to form ATP. This chemical reaction that forms ATP is called oxidative phosphorylation. The process, in which energy from the proton-motive force is used to make ATP, is sometimes called chemiosmosis.

1.5.2.3 Proton leak

Up to this point, we explained the coupling of the free energy produced from the transport of electrons, through the ETC, to the oxidative phosphorylation. However, this coupling is not complete. In fact, some of the protons that were pumped at the complexes I,III, and IV will

not need the ATP-synthase in order to migrate back to the matrix, a process named "proton leak". These protons, that did not use the ATP-synthase enzyme to enter the matrix, will not contribute in the ATP creation process, and thus result in the incomplete coupling between the proton pump and the creation of ATP.

1.5.2.4 Calcium contribution to the respiratory chain

In the previous part, we explained the basics of mitochondrial functioning, in particular substrate metabolism and the respiratory chain. In the cellular context, this organelle will be important in the contraction process by responding to the cellular energy demand. In fact, free cytoplasmic calcium will enter the mitochondria (via the calcium uniporter), and will act on different enzymes, mainly modulating the Krebs cycle. Indeed, in the Krebs cycle, calcium has an activation effect on two enzymes (Isocitrate dehydrogenase [20] and Alpha-ketoglutarate dehydrogenase [54]), that both contribute in the NADH production. Besides the above, calcium can act on the Krebs cycle by regulating the activity of the pyruvate dehydrogenase enzyme (PDH). This enzymes catalyses the reaction that transforms the pyruvate to Acetyl-CoA which is used, in the Krebs cycle, to produce NADH. We clearly see that calcium is an important player in affecting the concentrations of NADH. Hence calcium will have an indirect effect on the activity of the respiratory chain, since NADH is the substrate of the complex I, which is the start point of the respiratory chain.

1.5.2.5 Ionic transport and exchange

As previously mentioned, the inner mitochondria membrane is not permeable to ions and solutes. They generally need special carriers and channels to transport them. We will list those of interest in our model.

1.5.2.5.1 Adenine nucleotide translocator The ATP created in the matrix via the process of the respiratory chain needs to be transported to the cytoplasm to respond to the energy demand while in the contraction phase. In fact, the Adenine nucleotide translocator (ANT) is a carrier that exchanges free matrix ATP with free cytoplasmic ADP across the inner mitochondrial

membrane. The net process is denoted by:

$$ADP^{3-}_{cytoplasm} + ATP^{4-}_{matrix} \longrightarrow ADP^{3-}_{matrix} + ATP^{4-}_{cytoplasm}.$$

1.5.2.5.2 Calcium uniporter The mitochondrial calcium uniporter is a transmembrane protein, that allow free calcium in the cytoplasm to enters the mitochondria. It is the main source of calcium to the mitochondria. Its flow depends on the balance between the cytoplasmic and the matrix calcium concentrations, as well as on the mitochondrial membrane potential voltage.

1.5.2.5.3 Calcium/Sodium exchanger The calcium/sodium exchanger is an antiporter membrane protein that let the calcium out of the mitochondria while letting sodium in. Its flow depends naturally on the calcium and sodium concentrations. The dependace on the membrane potential is not well established as some studies suggests that its activity is eletcro-neutral (two Na + for one Ca 2+) [8, 53, 28], while other don't [60, 70, 57]. Together with the calcium uniporter, they are the main regulators of the calcium signaling between the mitochondria and the cell.

1.5.2.5.4 Mitochondrial permeability transition pore (mPTP) The mPTP is a key player in calcium regulation, in particular in the transport of calcium from the mitochondria to the cytoplasm. It is a non specific pore, whith an unknown clear molecular structure [31, 32]. When it opens, it allows all molecules with a size less than 1,5kDa to go through. It has two operating modes: the first one which is extensively studied, as it is believed to correspond to a pathological opening [19, 48], is a definitive opening that leads potentially to mitochondrial membrane collapse and eventually mitochondria swelling and cell death. The second one is a transitory opening, that is believed to be a physiological one, as it contributes in the healthy regulation of the intra-mitochondrial ions concentration, in particular calcium [24, 50, 25]. Many regulators of this pore were characterized [39], but the calcium concentration, the membrane potential, and the reactive oxygen species remain the most frequently identified.

Part I

A simple model of cardiac mitochondria with basic mechanisms

Note that most of the content evoked in this first part of the manuscript is taken from our previously published paper [71] in Mathematical Biosciences and Engineering, either in a direct way or in some reorganized manner. Sections of the paper that are used without modifications are highlighted in grey boxes.

Chapter 2

State of the art

Mathematical models of mitochondria have been an important tool for understanding its functionning. Most of these model focused on energy transduction and metabolsim, and were reviewed recently in two scientific papers in 2011 by Schmitz *et al.* [68], and in 2014 by Jafri *et al.*[40]. The first computer model of mitochondria energy transduction was developped in 1967 by Chance *et al.* [13]. Their model contained three main compartments: respiratory chain, phosphorylation and uncoupling, and energy linked transhydrogenase reactions (reactions in which hydrogen is transferred from one molecule to another). The chemical reactions inside these compartments, together with their common associated metabolic processes were modeled using nine state variables and seventeen parameters. The main purpose of this model was to investigate what controls the rate of oxidative phosphorylation and oxygen uptake by isolated mitochondria. The model was able to demonstrate quantitative relationships between competing metabolic processes in different steady states. An interesting feature in this model is its relative simplicity, especially in terms of the few number of parameters used. However, the lack of coupling of the model to the calcium component makes it irrelevant for studying cardiac mitochondria. That is because, as explained in the introduction (sec 1.2.2), the most interesting question when modeling cardiac mitochondria is how they contribute to the calcium cycle in the cardiac cell.

Another old model of mitochondria energy metabolism was developped by Achs and

Garfinkel [1] in 1979. This model was biologically more detailed than the former, in terms of incorporating many enzymatic mechanisms contributing to energy metabolism. The model was constructed using sixty-eight submodels of individual enzymes and membrane transport mechanisms covering mainly glycolysis, transaminases, the Krebs cycle, and their related metabolisms. These submodels were mainly constructed by fitting simple algebraic rate laws to literature data for the isolated in vitro species, and sometimes to data corresponding to intact system of perfused dog hearts. The aim of the model was to study ischemic metabolism. It was able to show changes in metabolite concentrations and pH during ischemia, and deciphered the mechanisms of metabolic oscillations which is also observed during ischemia. The idea of writing equations for fluxes or reaction rates based on fitting simple algebraic expressions to data from the literature is interesting, and was later on adopted by Bertram *et al.* [5]. This is because these expressions are mathematically easy to manipulate, and in addition could be parameterized if corresponding data are available. Nevertheless, sometimes this methodology could be misleading especially when literature data are inadequate to the context, are incomplete, or present errors.

Subsequently, several other authors developped mathematical models for mitochondrial oxydative phosphorylation [44, 6], but none of them included calcium exchanges between the mitochondria and the cytoplasm, nor its known effect on respiration. Calcium being a stimulator of mitochondrial respiration by contributing to the creation of mitochondrial NADH, which is an essential input element of the respiratory chain. That is until 1977, when Magnus & Keizer [51] developed a model (denoted MK model later on) that includes calcium signaling and mitochondrial respiratory chain for the β-cell. The MK model has six main mechanisms :

- pyruvate dehydrogenase
- proton pumping via the respiratory chain
- proton uptake by the F1F0-ATPase
- proton leak
- adenine nucleotide exchange
- calcium uniporter and Na^+/Ca^{2+}exchange.

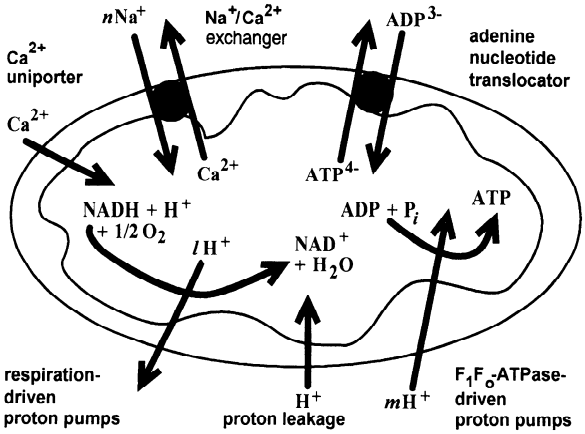

Figure 2.1: The different mechanisms that are considered in the MK model.

These mechanisms are either ionic transport through the mitochondrial inner membrane or chemical reactions inside the mitochondria. They are modeled by flux equations that are functions of the model state variables and some parameters associated to their mechanisms of action. Overall the MK model has fifty-two parameters and three state variables. Its flux equations will be detailed in the next section since, as it will shown later on, our new model will be strongly based on this model.

The Magnus & Keizer (MK) model

As we previously mentioned, six main mechanisms were considered in the MK model (Fig. 2.1). In this section, we will show how these expressions are derived in the MK model. But before that we state the classical conservation hypothesis that is often used in mitochondrial models.

It is the conservation of total concentrations of nicotinamide dinucleotide (NAD) and adenine nucleotide in the mitochondrial matrix:

$$N_{\text{tot}} = [\text{NADH}]_{\text{m}} + [\text{NAD}^+]_{\text{m}}, \tag{2.0.1}$$

$$A_{\text{tot,m}} = [\text{ATP}]_{\text{m}} + [\text{ADP}]_{\text{m}}. \tag{2.0.2}$$

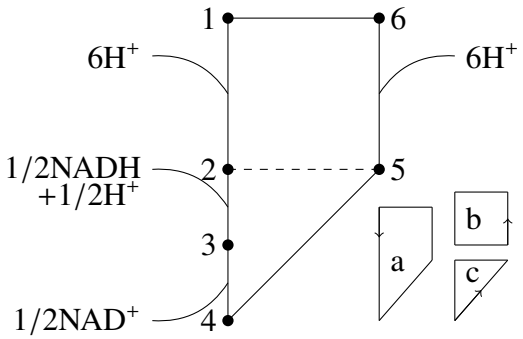

Figure 2.2: The six state Altman-King-Hill diagram used to illustrate the respiration driven proton pump. More details appear in the text.

2.0.1 MK flux expressions

In this section, we explain the biological role of each of the six considered mechanisms in the MK model, and we summarize the derivation of their associated flux expressions.

2.0.1.1 Oxygen consumption and proton pump

During the oxidation of the electron carrier NADH, two electrons are transported through the electron transport chain (ETC) following the oxidation-reduction equation:

$$\mathrm{NADH} + \mathrm{H}^+ + {}^1\!/_2\,\mathrm{O}_2 \longrightarrow \mathrm{NAD}^+ + \mathrm{H}_2\mathrm{O}. \tag{2.0.3}$$

This transport is coupled with proton pumping across the inner mitochondrial membrane, which generates a proton gradient. The gradient is then used to power the oxidative phosphorylation through the ATP synthase complex.

Magnus & Keizer considered a model of a respiration driven proton pump that is adapted from the six-state proton pump model of Pietrobon & Caplan [64]. This model is constructed using the more general theory of coupled flows and membrane transport, developped by Hill [35], that is extended from the Altman and King diagrams method to be later on known as Altman-King-Hill diagram method.

The reaction 2.0.3 is in fact a sum of three other reactions (occurring at complexes I,III,IV) where protons are pumped, since the oxidation of NADH involves the previous three complexes. Hence, this proton pump model takes into consideration all the protons pumped at three different energy conserving sites. MK considered that for each electron transferred through the ETC, the total number of protons pumped in the three energy conserving sites is 6.

The whole reaction can be represented schematically by the diagram in Fig. 2.2. On this diagram:

- The nodes represent possible states of the enzymatic complex.
- The edges represent possible transitions between these possible states.
- States on the left side are in the matrix and states on the right side are on the exterior of the mitochondria.
- The interval between the two sides can be seen as the mitochondrial membrane thickness.
- To each edge we can associate two rate constants α_{ij} and α_{ji} that represent the two possible transitions between states i and j. These rates can be either constants or functions of a variable of the ODE system.
- The arcs associated with some edges represent the binding or unbinding of molecules to the enzymatic complex.
- The completion of a single cycle in the counter clockwise direction lead to the ejection of $6H^+$ from inside the matrix to the outside.

The dashed edge associating states 2 and 5 illustrates the possibility of reaction slip, also known as intrinsic uncoupling. Pietrobon and Caplan as well as Magnus and Keizer

considered those slips in their models.

With this method, taking into consideration the intrinsic uncoupling, MK obtained the following expression for the rates of proton ejection $J_{\mathrm{H,resp}}$ and oxygen consumption J_{O}:

$$J_{\mathrm{H,resp}} = 6 \times 60\rho_{\mathrm{resp}}(J_{\mathrm{cycle,a}} + J_{\mathrm{cycle,b}}), \tag{2.0.4}$$

$$J_{\mathrm{O}} = \frac{1}{2} \times 60\rho_{\mathrm{resp}}(J_{\mathrm{cycle,a}} + J_{\mathrm{cycle,c}}), \tag{2.0.5}$$

where $J_{\mathrm{cycle,a}}$, $J_{\mathrm{cycle,b}}$, and $J_{\mathrm{cycle,c}}$ are a highly complex expressions with 12, 8, and 8 parameters respectively, and are in unit of s^{-1}. The coefficients 6 and $\frac{1}{2}$ account for the stoichiometry of reaction (2.0.3) between electrons, protons and oxygen atoms. The multiplication factor 60 transforms the unit from s^{-1} to /min. The parameter $\rho_{\mathrm{resp}} = 0.4$ nmol mgprot^{-1} is the concentration of proton pumps introduced by Magnus & Keizer [51]. The contribution of $J_{\mathrm{cycle,a}}$ and $J_{\mathrm{cycle,b}}$ in $J_{\mathrm{H,resp}}$ indicates that the proton ejection could happen either in association to the reaction (2.0.3) or alone through leaking. Similarly, the contribution of $J_{\mathrm{cycle,a}}$ and $J_{\mathrm{cycle,c}}$ in J_{O} indicates that reaction slip could lower the efficiency of the pump. The derivation of $J_{\mathrm{cycle,a}}$, $J_{\mathrm{cycle,b}}$, and $J_{\mathrm{cycle,c}}$ and their parameters will be detailed in section 3.2, where we adapt this diagram method to write down the oxygen consumption rate, and the associated proton pump flux expressions for our model. Magnus & Keizer approximated, to within 10% accuracy, the expressions (2.0.4), (2.0.5) by two simpler algebraic expressions as follows :

$$J_{\mathrm{H,resp}} = 360\rho_{\mathrm{resp}} \frac{r_a 10^{6\Delta pH} e^{\frac{F}{RT}\Delta E_{\mathrm{resp}}} - [r_a + r_b] e^{\frac{6gF}{RT}\Delta\psi}}{[1 + r_1 e^{\frac{F}{RT}\Delta E_{\mathrm{resp}}}] e^{\frac{6F}{RT}\Delta\psi_B} + [r_2 + r_3 e^{\frac{F}{RT}\Delta E_{\mathrm{resp}}}] e^{\frac{6gF}{RT}\Delta\psi}}, \tag{2.0.6}$$

$$J_{\mathrm{O}} = 30\rho_{\mathrm{resp}} \frac{[r_a 10^{6\Delta pH} + r_{c1} e^{\frac{6F}{RT}\Delta\psi_B}] e^{\frac{F}{RT}\Delta E_{\mathrm{resp}}} - r_a e^{\frac{6gF}{RT}\Delta\psi} + r_{c2} e^{\frac{F}{RT}\Delta E_{\mathrm{resp}}} e^{\frac{6gF}{RT}\Delta\psi}}{[1 + r_1 e^{\frac{F}{RT}\Delta E_{\mathrm{resp}}}] e^{\frac{6F}{RT}\Delta\psi_B} + [r_2 + r_3 e^{\frac{F}{RT}\Delta E_{\mathrm{resp}}}] e^{\frac{6gF}{RT}\Delta\psi}}, \tag{2.0.7}$$

where

$$\Delta E_{\mathrm{resp}} = \frac{RT}{F} \ln\left(K_{\mathrm{resp}} \sqrt{\frac{[\mathrm{NADH}]_{\mathrm{m}}}{[\mathrm{NAD}^+]_{\mathrm{m}}}} \right).$$

These two expressions are function of two state variables $[\mathrm{NADH}]_{\mathrm{m}}$ and $\Delta\psi$, and the values of their parameters and rate constants, as well as their descriptions, are listed in Table 2.1.

Table 2.1: Parameters and rate constants for the oxygen consumption rate and the proton pump flux in equations (2.0.6), and (2.0.7).

Parameter	Description	Value	Unit	Reference
K_{resp}	Equilibrium constant for Eq. (2.0.3)	1.35×10^{18}	dimensionless	[51]
ρ_{resp}	proton pump concentration	0.4	nmol mgprot^{-1}	[51]
r_1	Function of α_{ij}	2.077×10^{-18}	dimensionless	[51]
r_2	Function of α_{ij}	1.728×10^{-9}	dimensionless	[51]
r_3	Function of α_{ij}	1.059×10^{-26}	dimensionless	[51]
r_a	Function of α_{ij}	6.394×10^{-10}	s^{-1}	[51]
r_b	Function of α_{ij}	1.762×10^{-13}	s^{-1}	[51]
r_{c1}	Function of α_{ij}	2.656×10^{-19}	s^{-1}	[51]
r_{c2}	Function of α_{ij}	8.632×10^{-27}	s^{-1}	[51]
$\Delta\psi_B$	Total phase boundary potential	50	mV	[51]
g	Fitting factor	0.85	dimensionless	[51]

2.0.1.2 ADP phosphorylation and proton uptake

The proton electrochemical gradient created by the respiratory chain is used by the F1F0-ATPase complex to synthesize ATP by phosphorylation of ADP. Using the fact that ATP hydrolysis is coupled to proton ejection, Pietrobon and Caplan [64] modeled the mitochondrial F1F0-ATPase by a six-states proton pump driven by the reaction:

$$\text{ATP} + \text{H}_2\text{O} \longrightarrow \text{ADP} + \text{H}_2\text{PO}_4^-. \tag{2.0.8}$$

MK built the ADP phosphorylation flux from this model, adopting the same modeling approach as for the respiratory chain.

Similar calculations as in the previous section were repeated to obtain the expressions of the rate of ATP hydrolysis and its associated proton pumping. The oxidative phosphorylation rate and the rate of proton uptake by mitochondria can then be expressed as the opposite of the two former rates as follows:

$$J_{\text{H,ATP}} = -3 \times 60\rho_{F1}(J_{\text{cycle,a}} + J_{\text{cycle,b}}), \tag{2.0.9}$$

$$J_{\mathrm{F1F0}} = -60\rho_{F1}(J_{\mathrm{cycle,a}} + J_{\mathrm{cycle,c}}), \tag{2.0.10}$$

where the coefficient 3 corresponds to the stoichiometry between ATP hydrolysis and its associated proton pump. Here also the expression of $J_{\mathrm{cycle,a}}$, $J_{\mathrm{cycle,b}}$, and $J_{\mathrm{cycle,c}}$ wont be detailed, and it will be given in sec 3.2, in the context of our model. Here also Magnus & Keizer simplified these two expressions as follows:

$$J_{\mathrm{H,ATP}} = -180\rho_{\mathrm{F1}}\frac{p_a 10^{3\Delta pH}e^{\frac{F}{RT}\Delta G_{\mathrm{p,m}}} - [p_a + p_b]e^{\frac{3F}{RT}\Delta\psi}}{[1 + p_1 e^{\frac{F}{RT}\Delta G_{\mathrm{p,m}}}]e^{\frac{3F}{RT}\Delta\psi_B} + [p_2 + p_3 e^{\frac{F}{RT}\Delta G_{\mathrm{p,m}}}]e^{\frac{3F}{RT}\Delta\psi}}, \tag{2.0.11}$$

$$J_{\mathrm{F1F0}} = -60\rho_{\mathrm{F1}}\frac{[p_a 10^{3\Delta pH} + p_{c1}e^{\frac{3F}{RT}\Delta\psi_B}]e^{\frac{F}{RT}\Delta G_{\mathrm{p,m}}} - p_a e^{\frac{3F}{RT}\Delta\psi} + p_{c2}e^{\frac{F}{RT}\Delta G_{\mathrm{p,m}}}e^{\frac{3F}{RT}\Delta\psi}}{[1 + p_1 e^{\frac{F}{RT}\Delta G_{\mathrm{p,m}}}]e^{\frac{3F}{RT}\Delta\psi_B} + [p_2 + p_3 e^{\frac{F}{RT}\Delta G_{\mathrm{p,m}}}]e^{\frac{3F}{RT}\Delta\psi}}, \tag{2.0.12}$$

where

$$\Delta G_{\mathrm{p,m}} = \frac{RT}{F}\ln\left(K_{\mathrm{F1}}\frac{[\mathrm{ATP}]_{\mathrm{m}}}{[\mathrm{ADP}]_{\mathrm{m}}[\mathrm{Pi}]_{\mathrm{m}}}\right).$$

These two expressions are function of two state variables $[\mathrm{ADP}]_{\mathrm{m}}$ and $\Delta\psi$, and the values of their parameters and rate constants, as well as their descriptions, are listed in Table 2.2.

2.0.1.3 Adenine nucleotide translocator (ANT)

The ANT transports the mitochondrial ATP from the matrix to the cytoplasm, and the cytoplasmic ADP to the matrix. Magnus & Keizer wrote down an expression for the rate of this translocator:

$$J_{\mathrm{ANT}} = J_{\mathrm{max,ANT}}\frac{1 - \dfrac{0.05[\mathrm{ATP}]_{\mathrm{c}} \times 0.45 \times 0.8[\mathrm{ADP}]_{\mathrm{m}}}{0.45[\mathrm{ADP}]_{\mathrm{c}} \times 0.05[\mathrm{ATP}]_{\mathrm{m}}}\exp\left(-\frac{F}{RT}\Delta\psi\right)}{\left(1 + \dfrac{0.05[\mathrm{ATP}]_{\mathrm{c}}}{0.45[\mathrm{ADP}]_{\mathrm{c}}}\exp\left(-f\frac{F}{RT}\Delta\psi\right)\right)\left(1 + \dfrac{0.45 \times 0.8[\mathrm{ADP}]_{\mathrm{m}}}{0.05[\mathrm{ATP}]_{\mathrm{m}}}\right)}. \tag{2.0.13}$$

This rate depends primarily on the membrane potential $\Delta\psi$, as well as on the concentration of mitochondrial and cytoplasmic ATP and ADP respectively. In the expression (2.0.13), the coefficients leading the adenine nucleotide concentrations are the fractions of unbound ATP and ADP, existing in ionized form, in the matrix and cytoplasm compartments. Other parameters are listed in Table 2.3.

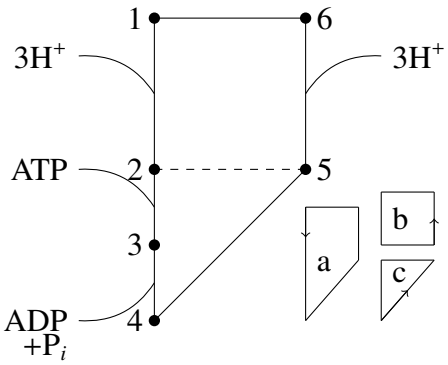

Figure 2.3: The six state Altman-King-Hill diagram used to illustrate the ATP hydrolysis.

Table 2.2: Parameters and rate constants for the ATP synthesis rate and the proton uptake flux in equations (2.0.11), and (2.0.12).

Parameter	Description	Value	Unit	Reference
K_{F1}	Equilibrium constant for Eq. (2.0.8)	1.71×10^{6}	mM	[51]
$[Pi]_m$	Phosphate concentration in the matrix	20	mM	[51]
ρ_{F1}	proton pump concentration	0.7	nmol mgprot^{-1}	[51]
p_1	Function of α_{ij}	1.346×10^{-18}	dimensionless	[51]
p_2	Function of α_{ij}	7.739×10^{-7}	dimensionless	[51]
p_3	Function of α_{ij}	6.65×10^{-15}	dimensionless	[51]
p_a	Function of α_{ij}	1.656×10^{-5}	s^{-1}	[51]
p_b	Function of α_{ij}	3.373×10^{-7}	s^{-1}	[51]
p_{c1}	Function of α_{ij}	9.651×10^{-14}	s^{-1}	[51]
p_{c2}	Function of α_{ij}	4.845×10^{-19}	s^{-1}	[51]

2.0.1.4 Calcium handling

Calcium is exchanged between mitochondria and the cytoplasm through membrane channels and pores such as the Ca^{2+}uniporter, the Na^{+}/Ca^{2+}exchanger and the mitochondrial permeability transition pore (mPTP). The exact role of the mPTP remains currently not fully understood (check part II of the manuscript). In the MK model, they considered only the Ca^{2+}uniporter and the Na^{+}/Ca^{2+}exchanger as calcium regulators.

Table 2.3: Adenine nucleotide translocator parameters of Eq. (2.0.13).

Parameter	Description	Value	Unit	Reference
$J_{max,ANT}$	Maximum exchange rate	1000	nmol mgprot^{-1} min^{-1}	[51]
f	Fraction $\Delta\psi$	0.5	dimensionless	[51]

Table 2.4: Na^+/Ca^{2+}exchanger parameters of Eq. (2.0.14).

Parameter	Description	Value	Unit	Reference
$J_{max,NaCa}$	Maximum rate for the Na/Ca exchanger	25	nmol mgprot^{-1} min^{-1}	[51]
K_{Na}	Michaelis-Menten constant	9.4	mM	[51]
b	Dependence on $\Delta\psi$	0	dimensionless	[51]
K_{Ca}	Michaelis-Menten constant	0.003	nmol mgprot^{-1}	[51]
$[Na]_c$	Cytoplasmic sodium concentration	30	mM	[51]

The expression of the Na^+/Ca^{2+} exchange flux is given as:

$$J_{NaCa} = J_{max,NaCa} \frac{\exp\left(\frac{bF(\Delta\psi-\Delta\psi^*)}{RT}\right)}{\left(1+\left(\frac{K_{Na}}{[Na]_c}\right)^2\right)\left(1+\frac{K_{Ca}}{[Ca^{2+}]_m}\right)} \tag{2.0.14}$$

For the calcium uniporter, Magnus and Keizer modeled the ionic flux using the Nernst-Planck equation, and then added the calcium dependence to the equation through an allosteric model [51]. The rate of the calcium internalized by the Ca^{2+}uniporter J_{uni} depends on the transmembrane voltage $\Delta\psi$ and on the cytoplasmic calcium concentration $[Ca^{2+}]_c$, as follows:

$$J_{uni} = J_{max,uni} \frac{\frac{[Ca^{2+}]_c}{K_{trans}}\left(1+\frac{[Ca^{2+}]_c}{K_{trans}}\right)^3}{\left(1+\frac{[Ca^{2+}]_c}{K_{trans}}\right)^4 + L\left(1+\frac{[Ca^{2+}]_c}{K_{act}}\right)^{-n_a}} \cdot \frac{2\frac{F}{RT}(\Delta\psi-\Delta\psi^*)}{1-\exp\left(-2\frac{F}{RT}(\Delta\psi-\Delta\psi^*)\right)}. \tag{2.0.15}$$

The parameters of the calcium uniporter and the Na^+/Ca^{2+}exchanger flux are given in Table 2.5 and 2.4 respectively.

Table 2.5: Calcium uniporter parameters of Eq. (2.0.15).

Parameter	Description	Value	Unit	Reference
$J_{\text{max,uni}}$	Maximum rate for the Ca^{2+}uniporter	300	$\text{nmol mgprot}^{-1}\,\text{min}^{-1}$	[51]
K_{trans}	Dissociation constant for uniporter translocated calcium	19	µM	[51]
K_{act}	Dissociation constant for uniporter activating calcium	0.38	µM	[51]
n_a	Activation cooperativity parameter	2.8	dimensionless	[51]
L	Equilibrium constant for uniporter conformations	110	dimensionless	[51]
$\Delta\psi^*$	$\Delta\psi$ offset	91	mV	[51]

2.0.1.5 External proton leakage

The MK model and some of the models based on it (*e.g.* Cortassa *et al.* [17], and Bertram *et al.* [5]) consider the external leakage of protons across the mitochondrial membrane to be a linear function of the transmembrane potential or the proton-motive force. However it has been shown that this leakage increases exponentially with the proton-motive force [10, 9]. We chose such an exponential function to model the protons leakage, as described in section 3.3.

The differential equation system

The MK model considered only three state variables : the membrane potential $\Delta\psi$, the matrix ADP concentration $[\text{ADP}]_\text{m}$, and the matrix calcium concentration $[Ca^{2+}]_\text{m}$. Then the dynamics of the mitochondrial activity can be modeled using the following ordinary differential equation system:

$$\begin{cases} \dfrac{\text{d}}{\text{d}t}[\text{ADP}]_\text{m} &= (J_\text{ANT} - J_\text{F1F0})\,, \\ \dfrac{\text{d}}{\text{d}t}\Delta\psi &= \left(J_\text{H,resp} - J_\text{H,ATP} - J_\text{ANT} - J_\text{leak} - 2J_\text{uni}\right)/C_\text{m}, \\ \dfrac{\text{d}}{\text{d}t}[Ca^{2+}]_\text{m} &= f_\text{m}\,(J_\text{uni} - J_\text{NaCa})\,, \end{cases} \tag{2.0.16}$$

where C_m and f_m are the mitochondrial membrane capacitance and the fraction of matrix free calcium respectively.

The second equation of the system 2.0.16 comes from applying Kirchhoff's current

law to mitochondrial membranes. The capacitance C_m, which is usually in units of Farad, is expressed in nmol mV^{-1} $mgprot^{-1}$ to match the unit of the ionic fluxes through the membrane. The values of C_m and f_m are given in Table 3.1.

The pioneering work of Magnus & Keizer led to many subsequent models that were adapted from the MK model. These models were all built based on a cumulative approach, adding biological component of interest from one model to another.

The Cortassa *et al.* model

An example of such a model was proposed in 2003, by Cortassa *et al.* [17]. The authors adapted the MK model to represent cardiac mitochondria instead of the β-cell. Additionally, they integrated a detailed description model for the TCA cycle (Fig. 2.4). The key regulatory enzymes included in their description of the TCA cycle are :

- Citrate synthase (CS)
- Aconitase (ACO)
- Isocitrate dehydrogenase (IDH)
- Alpha-ketoglutarate dehydrogenase (KGDH)
- Succinyl CoA lyase (SL)
- Succinate dehydrogenase (SDH)
- Fumarate hydratase (FH)
- Malate dehydrogenase (MDH)
- Aspartate amino transferase (AAT).

The cumulative addition of details in Cortassa's model made it complex. Overall, it has twelve state variables and ninety-nine parameters. Eight out of all the state variables included in their model were representing TCA cycle intermediates.

Besides the TCA cycle, all the flux expressions used in the MK model, were reused in the Cortassa model, sometimes with small modifications :

- replacement of the dependence of the respiratory fluxes on the proton motive force Δp, which is a linear combination of the membrane potential and ΔpH, instead of only the membrane potential $\Delta\psi$ in the MK model,
- making the NADH concentration, which is the main input for the respiratory chain, a state variable in contrast to the MK model where it was kept constant,
- adding an explicit dependence on the cytoplasmic calcium concentration of the expression of the calcium uniporter to account for its reversible activity under pathological conditions.

Their main interest was to study the effect of changes in substrate delivery and metabolic inhibition on the mitochondria, as well as the effect of calcium stimulation on the respiration of the mitochondria. Their model was able to reproduce qualitatively experimental data on respiratory control, calcium dynamics, and mitochondrial bioenergetics.

Subsequent versions of the Cortassa model were developped, in the same cumulative way, to account for the different mechanisms of interest for the authors. For example, in 2004, Cortassa *et al.* [18], extended their previously discussed model. In this new model, they included a description of mitochondrial ROS production, cytoplasmic ROS scavenging, as well as activation of inner membrane anion channels. In the new model, four new state variables and twenty-five new parameters were added to the previous one. This model will be discussed in more details, later on in chapter 5, when we will introduce the mPTP and ROS to our model.

From the biological point of view, the Cortassa *et al.* models are interesting since almost all the interplaying biological mechanisms in the mitochondria can be well identified in the model. Additionally, the parameters used in their model usually represent a biologically known particular submechanism or quantity (*e.g.* rate constants, dissociation constants, fraction of specific enzyme ...). However, in this kind of models, almost all the parameter values are adopted from literature. This is because the very high number of parameters that comes from the cumula-

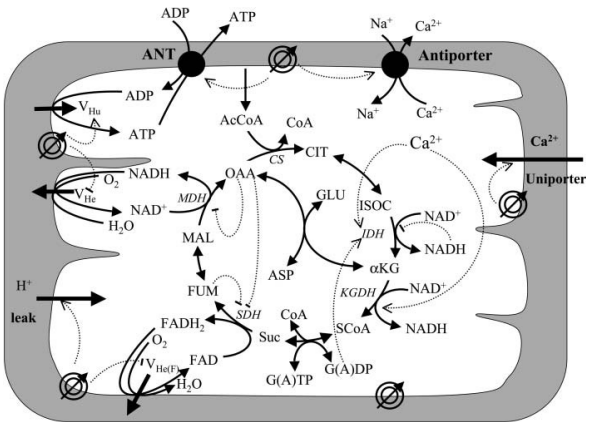

Figure 2.4: Schematic representation of the different mechanisms that are considered in the Cortassa model [17].

tive modeling approach, makes it almost impossible to calibrate these models to experimental data. In addition, complex algebraic expressions of flux, may lead to transcription errors when reusing them from one work to another. For example, here we highlight one transcription error, in the calcium uniporter flux, when using the MK expression in the Cortassa model :

$$J_{\text{uni}} = J_{\text{max,uni}} \frac{\dfrac{[\text{Ca}^{2+}]_c}{K_{\text{trans}}}\left(1+\dfrac{[\text{Ca}^{2+}]_c}{K_{\text{trans}}}\right)^3 \dfrac{2F\,(\Delta\psi - \Delta\psi^*)}{RT}}{\left(1+\dfrac{[\text{Ca}^{2+}]_c}{K_{\text{trans}}}^4\right) + L\left(1+\dfrac{[\text{Ca}^{2+}]_c}{K_{\text{act}}}\right)^{-n_a}\left(1-\exp\left(-2\frac{F}{RT}(\Delta\psi-\Delta\psi^*)\right)\right)}. \tag{2.0.17}$$

By comparing the MK expression of the calcium uniporter flux (2.0.15) with the Cortassa's expression (2.0.17) of the same flux, one can easily identify the transcription error in the denominator.

Because of the extreme complexity of these kind of models, that comes from the detailed biological mechanisms added (see Fig. 2.4), other authors such as Bertram *et al.* [5] proposed a different modeling approach.

The Bertram *et al.* model

In 2006, Bertram *et al.* took some components of the model of Cortassa (that was initially built from the MK model), and simplified its flux expressions by fitting simpler analytical expres-

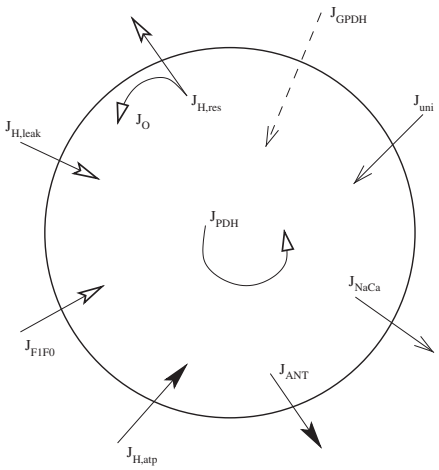

Figure 2.5: Schematic illustration of the fluxes and reactions used in the Betram *et al.* [5] model. Calcium fluxes are represented by arrows with line-type heads, whereas nucleotide fluxes and pre-phosphorylation associated protons uptake are represented with closed-head arrows. Proton fluxes are illustrated by open-heads arrows, and the production or oxidation of NADH are represented by curved arrows. Finally, the input of mitochondria from glycolysis is represented by a dashed arrow.

sions to the original ones. This methodology allows the reduction of the number of parameters of the model, while still capturing the mitochondrial dynamics. This can be mathematically useful especially when the objective is to calibrate the model parameters to experimental data. The Bertram model was used to assess the pancreatic $\beta-$cell mitochondrial response to calcium and glycolytic input. Unlike Cortassa *et al.* work, Bertram *et al.* did not add detailed description of the TCA cycle. Indeed, the Krebs cycle, glycolysis, and the pyruvate dehydrogenase complex were all modeled as one compartment leading mainly to the creation of mitochondrial NADH. Besides that, Bertram *et al.* kept almost the same biological mechanisms used in the MK model, but made the mitochondrial NADH concentration a state variable in their model. Overall, this model describes the dynamics of four state variables ($[NADH]_m$, $\Delta\psi$, $[ADP]_m$, and $[Ca^{2+}]_m$) using a system of ordinary differential equations. Using curve fitting to simpler analytical expressions, they were able to reduce the number of parameters of the MK model to twenty-six. The model was later used by Deikman *et al.* [21], who integrated more components such as astrocyte membrane potential and calcium handling by the ER. It was used to predict how the mitochondrial energy production is affected by some specific calcium release (IP_3-

mediated calcium release).

Even though the Bertram *et al.* model is relatively simple, and thus it is plausible mathematically speaking, it contains some hypothesis that are not relevant at least to our context. For example, to simplify the MK adenine tranlocator flux expression (2.0.13), they hypothesized that the ratio of adenine nucleotide in the matrix is equal to the same ratio in the cytoplasm ($\frac{[ATP]_m}{[ADP]_m} = \frac{[ATP]_c}{[ADP]_c}$). This could be of major concern, especially if the model is going to be used to asses mitochondrial respiration following cytoplasmic ADP additions. Additionally, the curve fitting procedure was not performed on the whole state variables space. Besides that, their model also presented transcription errors when copying the flux expressions from the Cortassa's model to their model. These errors and some potential corrections were discussed later on by Saa *et al.* in [66].

Discussion

To recapitulate, most of the mitochondrial models used nowadays are somehow based on the MK model, but surprisingly none of them reviewed closely how the original equations were written. That is why we previously detailed each flux expression starting from the original work of Hill [35], which has been the base of the work of Magnus & Keizer, and most of the subsequent mitochondrial models.

Additionally, in the exception of the Bertram *et al.* model, most of the mitochondrial models generally show a high level of complexity. This is because these models are generally developed following a cumulative approach, adding new mechanisms and biological reactions to previous models, which leads to dozens of state variables and hundreds of parameters (Table. 2.6). This large number of equations and parameters is not compatible with calibration techniques required for validation against experimental data. Indeed, using too large sets of parameters, which all have uncertainties, reduces the identifiability of the parameters, and often results in cases of overfitting. One important, advantage of these kind of models is that their parameters are directly related to biophysical rates. This is interesting because one could improve these existing models if more accurate measurements of these rates become available.

Table 2.6: Summary of the number of parameters and state variables for various mitochondrial models in the literature.

Model (year)	No. of state variables	No. of parameters	Reference
Chance (1967)	9	17	[13]
Bohnensack (1981)	8	20	[6]
Magnus & Keizer (1997)	3	52	[51]
Cortassa *et al.* (2003)	12	99	[17]
Cortassa *et al.* (2004)	16	124	[18]
Bertram *et al.* (2006)	4	26	[5]
Bazil *et al.* (2010)	73	359	[2]

On the other hand, in simplified models such as the model written by Bertram *et al.* , parameters do not necessarily represent a biophysical quantity. That is because they are developed using curve fitting to more complex models. However, they are more handy in a mathematical sense. Indeed, these kind of models are more comprehensible, and they could be clearer than complex models when assessing the effect of a certain parameter on a certain output of the model (state variables, fluxes or even reaction rates) for example. Also, these models are numerically convenient especially when they describe part of a larger cellular model. That is because they reduce considerably the computational cost when performing simulation on the larger scale model. Finally, we think that both complex and simplified models are important to understand the functions of the mitochondria. The choice between these two paradigms depends on the modeler's objectives.

Chapter 3

Our new cardiac mitochondrial model

Contents

The MK model is a good starting point for writing down the model we aim for since it is one of the most tested models in the literature. Nevertheless, several new considerations related to our context should be taken. In addition, we want to create a minimal model in term of number of parameters, so it can be mathematically possible to calibrate it to experimental data. In section 3.3 we show how we simplify the original model by fitting its fluxes to simpler analytical expressions with less parameters , whenever it is possible. Section 3.4 is devoted for solving the ODE system of our model. Then in section 3.5 we explain one part of the available experimental data we had access on, and we make a link between the data and our model so that these data can be used in the next chapter for the calibration of our model.

3.1 New considerations

New state variables added

Unlike in the MK model where NADH was only a constant, it is now a state variable of our model. This is because mitochondrial respiration is closely related to the ratio of NAD concentrations, and also because this ratio is dependent on calcium which is a crucial component in our context. Beside being dependent on calcium, NADH concentration is also strongly dependent on the substrate metabolization activity (see 1.5.2.1). The dynamics of NADH concentration can be modeled by the following differential equation:

$$\frac{\mathrm{d}}{\mathrm{d}t}[\mathrm{NADH}]_\mathrm{m} = J_\mathrm{PDH} - J_\mathrm{O}, \tag{3.1.1}$$

where J_PDH is the rate of NADH production, and will be derived in details later in section 3.2, and J_O is oxygen consumption rate discussed earlier in section 2.0.1.1.

In addition, we also considered the **cytoplasmic calcium concentration** ($[Ca^{2+}]_c$), and the cytoplasmic ADP concentration ($[ADP]_c$). These two variables were added because they are the controllable inputs of the experiments. Since we add the variable $[ADP]_c$ to the model, we assumed the following conservation relation:

$$A_\mathrm{tot,c} = [\mathrm{ATP}]_\mathrm{c} + [\mathrm{ADP}]_\mathrm{c}. \tag{3.1.2}$$

Change of variable: From concentrations to thermodynamics variables

In addition to those considerations, we also chose to express the mitochondrial behavior in terms of thermodynamic variables (actually related to an electrochemical force induced by chemical gradients of concentrations), instead of the concentrations. That is because they are more informative to biologists than absolute concentrations. Our model uses the state variables in bold face within this section.

NADH redox potential. It is a logarithmic function of the redox couple NADH and NAD^+, and is expressed in units of mV as follows:

$$\Delta E_{\text{resp}} = \frac{RT}{F} \ln\left(K_{\text{resp}} \sqrt{\frac{[\text{NADH}]_{\text{m}}}{[\text{NAD}^+]_{\text{m}}}} \right), \tag{3.1.3}$$

where $K_{\text{resp}} = 1.35 \times 10^{18}$ is the redox equilibrium constant of the reaction (2.0.3) [51].

Using the conservation relation (2.0.1), the NADH redox potential reads:

$$\Delta E_{\text{resp}}([\text{NADH}]_{\text{m}}) = \frac{RT}{F} \ln\left(K_{\text{resp}} \sqrt{\frac{[\text{NADH}]_{\text{m}}}{N_{\text{tot}} - [\text{NADH}]_{\text{m}}}} \right). \tag{3.1.4}$$

Mitochondrial Gibbs free energy. It describes the energy balance between mitochondrial ATP and ADP. It is expressed in units of mV as follows:

$$\Delta G_{\text{p,m}} = \frac{RT}{F} \ln\left(K_{\text{F1}} \frac{[\text{ATP}]_{\text{m}}}{[\text{ADP}]_{\text{m}}[\text{Pi}]_{\text{m}}} \right), \tag{3.1.5}$$

where $K_{\text{F1}} = 1.71 \times 10^6$ mM is the equilibrium constant for the ATP hydrolysis reaction [51], and the inorganic phosphate concentration $[\text{Pi}]_{\text{m}}$ is considered as a fixed parameter.

The conservation relation (2.0.2) gives:

$$\Delta G_{\text{p,m}}([\text{ADP}]_{\text{m}}) = \frac{RT}{F} \ln\left(K_{\text{F1}} \frac{A_{\text{tot,m}} - [\text{ADP}]_{\text{m}}}{[\text{ADP}]_{\text{m}}[\text{Pi}]_{\text{m}}} \right). \tag{3.1.6}$$

Cytoplasmic Gibbs free energy.

$$\Delta G_{\text{p,c}} = \frac{RT}{F} \ln\left(K_{\text{F1,c}} \frac{[\text{ATP}]_{\text{c}}}{[\text{ADP}]_{\text{c}}[\text{Pi}]_{\text{c}}} \right). \tag{3.1.7}$$

that could also be rewritten, using the conservation relation (3.1.2), as follows:

$$\Delta G_{\text{p,c}} = \frac{RT}{F} \ln\left(K_{\text{F1,c}} \frac{A_{\text{tot,c}} - [\text{ADP}]_{\text{c}}}{[\text{ADP}]_{\text{c}}[\text{Pi}]_{\text{c}}} \right). \tag{3.1.8}$$

We kept the variables for the **transmembrane potential** $\Delta\psi$ and the **mitochondrial calcium concentration** $[\text{Ca}^{2+}]_{\text{m}}$ since they are of main interest for us.

New ODE system.

The new ODE system that models the cardiac mitochondrial activity was then written as follows:

$$\begin{cases} \dfrac{\mathrm{d}}{\mathrm{d}t}\Delta E_{\mathrm{resp}} &= \varphi_1(\Delta E_{\mathrm{resp}})\,(J_{\mathrm{sub}} - J_{\mathrm{O}})\,, \\ \dfrac{\mathrm{d}}{\mathrm{d}t}\Delta G_{\mathrm{p,m}} &= \varphi_2(\Delta G_{\mathrm{p,m}})\,(J_{\mathrm{F1F0}} - J_{\mathrm{ANT}})\,, \\ \dfrac{\mathrm{d}}{\mathrm{d}t}\Delta G_{\mathrm{p,c}} &= \varphi_3(\Delta G_{\mathrm{p,c}})\left(\gamma J_{\mathrm{ANT}} - \dfrac{\mathrm{d}}{\mathrm{d}t}J_{\mathrm{ADP,ext}}(t)\right), \\ C_{\mathrm{m}}\dfrac{\mathrm{d}}{\mathrm{d}t}\Delta\psi &= 12J_{\mathrm{O}} - 3J_{\mathrm{F1F0}} - J_{\mathrm{ANT}} - J_{\mathrm{leak}} - 2J_{\mathrm{uni}}, \\ \dfrac{\mathrm{d}}{\mathrm{d}t}[\mathrm{Ca}^{2+}]_{\mathrm{m}} &= f_m(J_{\mathrm{uni}} - J_{\mathrm{NaCa}}), \\ \dfrac{\mathrm{d}}{\mathrm{d}t}[\mathrm{Ca}^{2+}]_{\mathrm{c}} &= f_c\tilde{\gamma}(J_{\mathrm{NaCa}} - J_{\mathrm{uni}}) + \dfrac{\mathrm{d}}{\mathrm{d}t}[\mathrm{Ca}^{2+}]_{\mathrm{ext}}(t) \end{cases} \tag{3.1.9}$$

where

$$\varphi_1(\Delta E_{\mathrm{resp}}) = \frac{1}{2}\frac{RT}{F}\frac{\left(K_{\mathrm{resp}}^2 + \exp\left(2\frac{F}{RT}\Delta E_{\mathrm{resp}}\right)\right)^2}{K_{\mathrm{resp}}^2 N_{\mathrm{tot}}\exp\left(2\frac{F}{RT}\Delta E_{\mathrm{resp}}\right)}, \tag{3.1.10}$$

$$\varphi_2(\Delta G_{\mathrm{p,m}}) = \frac{RT}{F}\frac{\left(1 + [\mathrm{Pi}]_{\mathrm{m}}K_{\mathrm{F1}}^{-1}\exp\left(\frac{F}{RT}\Delta G_{\mathrm{p,m}}\right)\right)^2}{A_{\mathrm{tot,m}}[\mathrm{Pi}]_{\mathrm{m}}K_{\mathrm{F1}}^{-1}\exp\left(\frac{F}{RT}\Delta G_{\mathrm{p,m}}\right)}, \tag{3.1.11}$$

and

$$\varphi_3(\Delta G_{\mathrm{p,c}}) = \frac{RT}{F}\frac{\left(1 + [\mathrm{Pi}]_{\mathrm{c}}K_{\mathrm{F1,c}}^{-1}\exp\left(\frac{F}{RT}\Delta G_{\mathrm{p,c}}\right)\right)^2}{A_{\mathrm{tot,c}}[\mathrm{Pi}]_{\mathrm{c}}K_{\mathrm{F1,c}}^{-1}\exp\left(\frac{F}{RT}\Delta G_{\mathrm{p,c}}\right)}, \tag{3.1.12}$$

are functions that come from the derivation chain rule when mapping concentrations to thermodynamical variables. These functions have units of $\mathrm{mV\,nmol^{-1}\,mgprot}$. The functions $J_{\mathrm{ADP,ext}}$ and $[\mathrm{Ca}^{2+}]_{\mathrm{ext}}$ are source terms for external ADP and Ca^{2+} respectively, al-

lowing us to mimic various experimental conditions.

The scalar parameter γ regroups two factors: the mitochondria over cytoplasm volume ratio, and a unit conversion factor from nmol mgprot^{-1} to mM. The parameter $\tilde{\gamma}$ is simply $10^3 \times \gamma$ to account for the unit of $[Ca^{2+}]_c$ in µM. The values of the parameters used in equations (3.1.9), (3.1.10), (3.1.11) and (3.1.12) are listed in Table 3.1.

Table 3.1: Parameters associated to the ODE system (3.1.9) and Equations (3.1.10), (3.1.11), (3.1.12).

Parameter	Description	Value	Unit	Reference
f_m	Fraction of free matrix calcium concentration	3×10^{-4}	dimensionless	[51]
γ	Volume ratio × flux unit conversion	0.0105	dimensionless	Calibrated (sec. 4.5)
N_{tot}	Total NADH/NAD$^+$ concentration	8	nmol mgprot^{-1}	[51]
$A_{\text{tot,m}}$	Total mitochondrial adenine nucleotide concentration	12	nmol mgprot^{-1}	[51]
$A_{\text{tot,c}}$	Total cytoplasmic adenine nucleotide concentration	2	mM	[52]
f_c	Fraction of free cytosolic calcium concentration	1×10^{-2}	dimensionless	[52]
C_{m}	Membrane capacitance	1.450×10^{-3}	nmol mV^{-1} mgprot^{-1}	[51]

3.2 Derivation of fluxes and reactions rate expressions

Overall, with the three added states variables, our model has six state variables and takes into consideration the following mitochondrial mechanisms: substrate metabolization, oxygen consumption by the respiratory chain, ATP synthesis trough phosphorylation, ATP/ADP translocation, Ca^{2+} regulation through the calcium uniporter and the Na^+/Ca^{2+} exchanger and finally proton leakage (see Figure 3.1).

These mechanisms are modeled by ionic flux expressions that are functions of the state variables and parameters of the model. In this section, we explain the biological role of each of the seven considered mechanisms, and we detail the derivation of their associated flux functions. Expressions from the current literature were derived by successive contributions, starting from

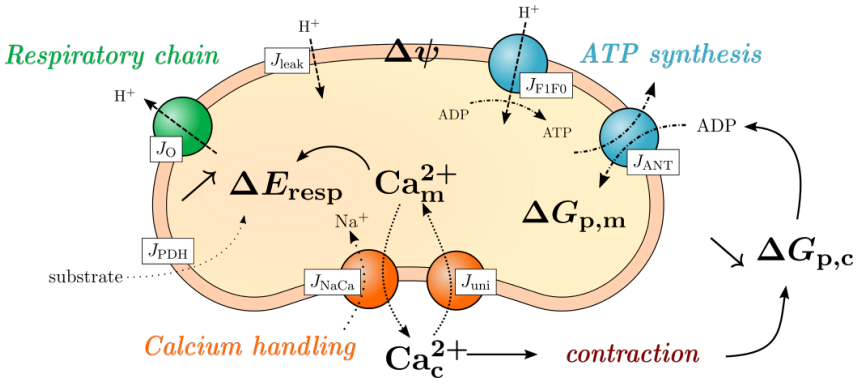

Figure 3.1: The seven reactions and flux described by our model, indicated by boxes. State variables are indicated by bold font.

first mathematical statements of the various biochemical processes involved. Consequently, these processes and their current expressions are difficult to relate. Hence, we started our derivation process from the original papers.

Substrate metabolization

In the cytoplasm, glucose is metabolized to pyruvate, which enters the mitochondria through a carrier. Then, pyruvate enters the Krebs cycle through the help of the pyruvate dehydrogenase (PDH) enzyme, which leads subsequently to NADH production. PDH has an active form (PDH_a) that becomes completely inactivated when phosphorylated (PDH-P). The conversion between these two forms is regulated by the kinase and phosphatase enzymes. Magnus and Keizer [52] discussed the dependence of the fraction of PDH_a on mitochondrial calcium, as it is believed to stimulate the phosphatase reaction that produces PDH_a. They proposed an expression of the fraction of PDH_a:

$$f_{PDH_a} = \frac{1}{1 + u_2\left[1 + u_1\left(1 + \frac{[Ca^{2+}]_m}{K_{Ca}}\right)^{-2}\right]}, \tag{3.2.1}$$

where u_1 is the dependence of PDH-P dephosphorylation on Mg^{2+}, u_2 is the ratio between the maximal rate of kinase and the maximal rate of phosphatase, and K_{Ca} is the Ca^{2+}-

dependant affinity of the PDH-P phosphatase. Bertram *et al.* [5] then used this expression, with the addition of an explicit dependence on the ratio $[\text{NADH}]_\text{m}/[\text{NAD}^+]_\text{m}$, to model the mitochondrial NADH production considering glycolysis, pyruvate dehydrogenase and its process through the Krebs cycle as a single compartment. This rate of production is denoted by J_PDH and has the following expression:

$$J_\text{PDH} = J_\text{max} \times \frac{1}{1 + u_2\left[1 + u_1\left(1 + \frac{[\text{Ca}^{2+}]_\text{m}}{K_\text{Ca}}\right)^{-2}\right]} \times \frac{1}{\frac{[\text{NADH}]_\text{m}}{[\text{NAD}^+]_\text{m}} + K_\text{PDHnad}}, \tag{3.2.2}$$

which parameters J_max, u_1, u_2, K_Ca, and K_PDHnad are given in Table 3.2. The value of the parameter J_max depends on the external substrate: glutamate, malate or both.

Table 3.2: Parameters of the rate of production of NADH by pyruvate dehydrogenase (3.2.2).

Parameter	Description	Value	Unit	Reference
u_1	Dependence of PDH-P dephosphorylation on Mg^{2+}	1.5	dimensionless	[52]
u_2	Maximal rate of kinase / phosphatase	1	dimensionless	[52]
K_Ca	Affinity for the PDH-P phosphatase	0.5×10^{-1}	µM	[52]
J_max	Maximum rate for PDH flux	7.157×10^{1}	nmol mgprot^{-1} min^{-1}	[5]
k_PDHnad	Parameter for the dependence of J_PDH on NAD	1	dimensionless	[5]

Oxygen consumption and proton pump

The expressions of the respiration and the associated proton pump flux were adapted by Magnus and Keizer from a previously published proton pump model of Pietrobon and Caplan [64], who used the Hill-diagram method [35] to derive their equations (check section 2.0.1.1). In this section we will explain how these were derived using the diagram method. In contrast with the MK model (Fig. 2.2), and for simplicity, we made the assumption that the reaction is fully coupled to the outward proton flow, and all possible proton leaks are taken into account in the inward leak added in section 3.2. This means that the dashed edge associating states 2 and 5 in Fig. 2.2 are no longer considered in our

version of the proton pump model (Fig. 3.2).

The expression of the cycle rate (the average number of occurrences of the complete cycle per second) was discussed by Hill [35], and is given by:

$$J_{\text{cycle}} = 60N\frac{\Pi_+ - \Pi_-}{\Sigma} \tag{3.2.3}$$

where N is the total number of respiratory enzymatic complexes in the inner membrane and the coefficient 60 converts s^{-1} to min^{-1}. $\Pi_\pm$ are the product of the rate constants of the complete cycle, in the counter clockwise and clockwise directions respectively:

$$\Pi_+ = \alpha_{12}\alpha_{23}\alpha_{34}\alpha_{45}\alpha_{56}\alpha_{61}, \quad \Pi_- = \alpha_{16}\alpha_{65}\alpha_{54}\alpha_{43}\alpha_{32}\alpha_{21}. \tag{3.2.4}$$

In order to define Σ, we need to introduce the Hill definition of what are called directional diagrams. For each state i of the cycle (in our case 6 states), we can associate a collection of directional diagrams for this state i, which illustrates all the possible ways leading to the state i taking into consideration 2 rules:

- The path towards state i must not be a complete cycle.
- The maximum number of edges must be used (5 in our case).

As example, Figure 3.3 lists the six possible directional diagrams leading to state 1. States 2 to 5 also have six similar diagrams, built following the same principles. To each diagram corresponds a coefficient that is the product of the rates associated to the edges that constitute the path to state i. Then, we define Σ_i as the sum of these coefficients. For example:

$$\begin{aligned}\Sigma_1 = {} & \alpha_{23}\alpha_{34}\alpha_{45}\alpha_{56}\alpha_{61} + \alpha_{65}\alpha_{54}\alpha_{43}\alpha_{32}\alpha_{21} + \alpha_{34}\alpha_{45}\alpha_{56}\alpha_{61}\alpha_{21} \\ & + \alpha_{61}\alpha_{54}\alpha_{43}\alpha_{32}\alpha_{21} + \alpha_{56}\alpha_{61}\alpha_{43}\alpha_{32}\alpha_{21} + \alpha_{45}\alpha_{56}\alpha_{61}\alpha_{32}\alpha_{21}.\end{aligned} \tag{3.2.5}$$

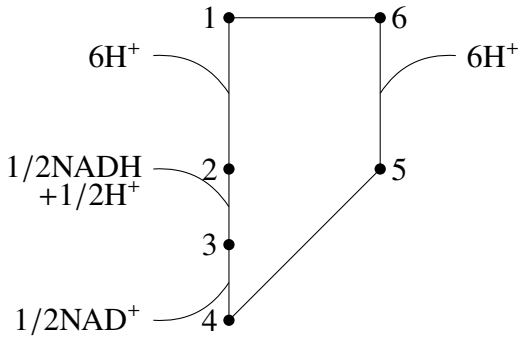

Figure 3.2: The six state Altman-King-Hill diagram used to illustrate the respiration driven proton pump in our model. Intrinsic uncoupling, illustarted by the transitions from states 2 to 5 and vice versa, is removed from the original Pietrobon & Caplan model [64] and also the subsequent MK model [51].

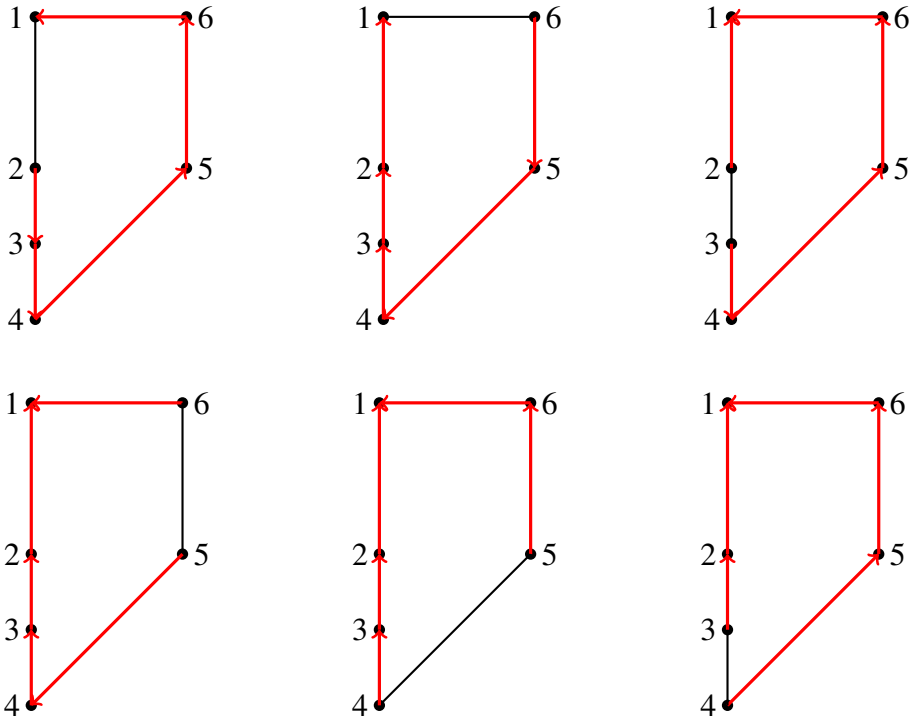

Figure 3.3: The six possible directional diagrams that lead to state 1.

The denominator Σ in (3.2.3) is then obtained as the sum of coefficients for all states:

$$\Sigma = \Sigma_1 + \Sigma_2 + \Sigma_3 + \Sigma_4 + \Sigma_5 + \Sigma_6 \tag{3.2.6}$$

Basically, Σ is the sum of $6\times6 = 36$ elements, and each element is the product of 5 rate constants. Even though that is a very large number of terms, it is still a simplification as we did not consider the intrinsic uncoupling in our model (i.e the slip transitions between the states 2 and 5), contrary to the original models of Pietrobon and Caplan or Magnus and Keizer.

The reaction rate is hence a function of all rates of the cycle. Those can be either of first order (constants) or pseudo-first order (function of the ODE variables). Typically, the binding of a molecule to the enzymatic complex is associated to a pseudo first order rate constant. In our case, and since the respiratory variable is NADH, that would be the case for transitions (2)→(3) and (4)→(3). We can then write

$$\alpha_{23} = \alpha^*_{23}\sqrt{\mathrm{NADH}}, \quad \alpha_{43} = \alpha^*_{43}\sqrt{\mathrm{NAD^+}}.$$

The membrane potential plays a role in the (1)↔(6) transitions since it is where the conformational change in the enzymatic complex happens i.e the reorientation of the binding sites. Following thermodynamics considerations, Pietrobon and Caplan were able to give expressions of the rate constants α_{16} and α_{61} as function of the membrane potential $\Delta\psi$ and the boundary potential parameter $\Delta\psi_B$:

$$\begin{aligned} \alpha_{16} &= \alpha_{16,0}e^{(nF/2RT)(\Delta\psi-\Delta\psi_B)} = \alpha_{16}(0)e^{(3\frac{F}{RT})(\Delta\psi-\Delta\psi_B)}, \\ \alpha_{61} &= \alpha_{61,0}e^{(-nF/2RT)(\Delta\psi-\Delta\psi_B)} = \alpha_{61}(0)e^{(-3\frac{F}{RT})(\Delta\psi-\Delta\psi_B)}, \end{aligned} \tag{3.2.7}$$

where $F = 96480$ Cmol^{-1} is the Faraday constant, $R = 8.315$ VCmol^{-1}, K^{-1} is the perfect gaz constant and $T = 310.1$ K is the temperature. The parameters $\alpha_{16,0}$ and $\alpha_{61,0}$ are the values of the rate constants α_{16} and α_{61}, when $\Delta\psi = \Delta\psi_B$, respectively. All other rates are considered constant as in the MK model.

A summary of parameters involved in the expression of J_{cycle} is given in Table 3.3. In the final expression of the respiration flux, the parameter N is replaced by the concentration of proton pumps $\rho_{\text{resp}} = 0.4$ nmol mgprot^{-1} introduced by Magnus and Keizer.

Finally, as 6 protons are ejected and half an oxygen is consumed during one cycle, the expressions of the rates used in our model are:

$$J_{\text{H,resp}} = 12 \times J_{\text{O}} = 6\rho_{\text{resp}} J_{\text{cycle}}. \tag{3.2.8}$$

Table 3.3: Parameters of the respiration driven proton pump flux and the oxygen consumption rate, involved in expressions (3.2.3) to (3.2.8). R.C := rate constant.

Parameter	Description	Value	Unit	Reference
α_{12}	Unimolecular R.C for the transition 1→2	400	s^{-1}	[64]
α_{21}	Unimolecular R.C for the transition 2→1	5	s^{-1}	[64]
α^*_{23}	Bimolecular R.C for the transition 2→3	3.405×10^4	nmol$^{-1/2}$ mgprot$^{1/2}$ s^{-1}	[51]
α_{32}	Unimolecular R.C for the transition 3→2	8.0×10^4	s^{-1}	[64]
α_{34}	Unimolecular R.C for the transition 3→4	400	s^{-1}	[64]
α^*_{43}	Bimolecular R.C for the transition 4→3	1.59×10^2	nmol$^{-1/2}$ mgprot$^{1/2}$ s^{-1}	[51]
α_{45}	Unimolecular R.C for the transition 4→5	40	s^{-1}	[64]
α_{54}	Unimolecular R.C for the transition 5→4	0.4	s^{-1}	[64]
α_{56}	Unimolecular R.C for the transition 5→6	100	s^{-1}	[64]
α_{65}	Unimolecular R.C for the transition 6→5	1.0×10^5	s^{-1}	[64]
$\alpha_{16,0}$	R.C for the transition 1→6 at $\Delta\psi = 0$	130	s^{-1}	[64]
$\alpha_{61,0}$	R.C for the transition 6→1 at $\Delta\psi = 0$	1.0×10^{12}	s^{-1}	[64]
ρ_{resp}	Proton pump concentration	0.4	nmol mgprot^{-1}	[51]
$\Delta\psi_B$	Boundary potential parameter	50	mV	[64]

ADP phosphorylation and proton uptake

We used the same method to derive the proton flux occurring during ATP synthesis as for the respiratory chain. The Hill-diagram used for this reaction correspond to a model of a six-state proton pump proposed by Pietrobon and Caplan [64] (see Fig. 3.4). We made the same assumption as for the respiratory chain, by neglecting the leakage and slippage of

the proton pump.

We note β_{ij} the rate constants associated to this diagram. As for the respiration driven proton pump model, all rates are first order, except those related to our ODE system variables. The latter ones are pseudo-first order rates, and they can be written as function of the state variables $(\Delta\psi, [\text{ADP}]_\text{m})$ as follows:

$$\begin{aligned}
\beta_{23} &= \beta^*_{23}(A_{\text{tot},m} - [\text{ADP}]_\text{m}),\\
\beta_{43} &= \beta^*_{43}[\text{ADP}]_\text{m}[\text{Pi}]_\text{m},\\
\beta_{16} &= \beta_{16}(0)\exp\left(1.5\frac{F}{RT}(\Delta\psi - \Delta\psi_B)\right)\\
\beta_{61} &= \beta_{61}(0)\exp\left(-1.5\frac{F}{RT}(\Delta\psi - \Delta\psi_B)\right).
\end{aligned}$$

The intermediate quantities Π_+, Π_-, Σ, and J_cycle are calculated the same way as in section 3.2, only replacing the rate constants α_{ij} by the β_{ij} associated to the diagram 3.4.

Since we express the rate of the oxidative phosphorylation and the proton uptake by mitochondria, a minus sign is added to the rates of ATP hydrolysis and its associated proton pump:

$$J_\text{H,ATP} = 3J_\text{F1F0} = -3\rho_\text{F1}J_\text{cycle}, \tag{3.2.9}$$

where ρ_F1 is the concentration of the F1F0-ATPase-driven proton pump, in replacement of N in the definition (3.2.3) of J_cycle. The parameters associated to the flux expressions (3.2.9) are given in Table 3.4.

External proton leakage

As previously explained in section 2.0.1.5, we use an exponential function (3.3.7) to model the external proton leakage across the inner mitochondrial membrane.

$$J_\text{leak}(\Delta\psi) = p_{20}\exp\left(p_{21}\Delta\psi\right). \tag{3.2.10}$$

The parameter p_{20} and p_{21} associated the the proton leakage flux were computed by fitting the expressions (3.3.7) to the data from [45].

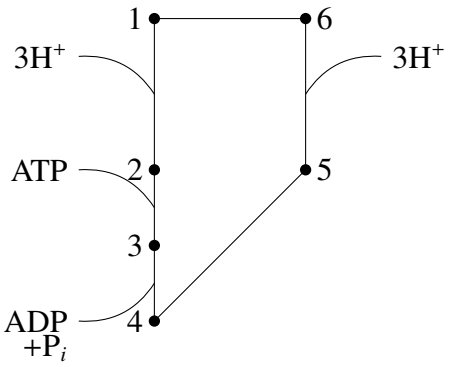

Figure 3.4: Our modified version of the six-state Altman-King-Hill diagram for an ATPase-driven proton pump. The proton stoichiometry is taken from the work of Pietrobon and Caplan [64].

Table 3.4: Parameters of the oxidative phosphorylation rate and the proton uptake flux, involved in expressions (3.2.9). R.C := rate constant.

Parameter	Description	Value	Unit	Reference
β_{12}	Unimolecular R.C for the transition 1→2	400	s^{-1}	[64]
β_{21}	Unimolecular R.C for the transition 2→1	40	s^{-1}	[64]
β^*_{23}	Bimolecular R.C for the transition 2→3	5×10^3	mgprot $nmol^{-1}$ s^{-1}	[64]
β_{32}	Unimolecular R.C for the transition 3→2	5×10^3	s^{-1}	[64]
β_{34}	Unimolecular R.C for the transition 3→4	100	s^{-1}	[64]
β^*_{43}	Bimolecular R.C for the transition 4→3	5×10^4	M^{-1} mgprot $nmol^{-1}$ s^{-1}	[51]
β_{45}	Unimolecular R.C for the transition 4→5	100	s^{-1}	[64]
β_{54}	Unimolecular R.C for the transition 5→4	100	s^{-1}	[64]
β_{56}	Unimolecular R.C for the transition 5→6	1000	s^{-1}	[64]
β_{65}	Unimolecular R.C for the transition 6→5	1000	s^{-1}	[64]
$\beta_{16,0}$	R.C for the transition 1→6 at $\Delta\psi = 0$	4.98×10^7	s^{-1}	[64]
$\beta_{61,0}$	R.C for the transition 6→1 at $\Delta\psi = 0$	100	s^{-1}	[64]
ρ_{F1}	Proton pump concentration	0.7	nmol $mgprot^{-1}$	[51]

Na^+/Ca^{2+} exchange rate

We assume that the Na^+/Ca^{2+}exchanger is electro-neutral (two Na^+ for one Ca^{2+}) [8, 53, 28]. Thus the flux does not depend on the membrane potential of the mitochondria, and we modeled the exchanger by a two-substrates Michaelis-Menten kinetic model (see Table 2.4 for parameters):

$$J_{\mathrm{NaCa}} = J_{\mathrm{max,NaCa}} \frac{1}{\left(1 + \left(\frac{K_{\mathrm{Na}}}{[\mathrm{Na}]_{\mathrm{c}}}\right)^2\right)\left(1 + \frac{K_{\mathrm{Ca}}}{[\mathrm{Ca}^{2+}]_{\mathrm{m}}}\right)} \tag{3.2.11}$$

Several studies proposed similar expressions for the Na^+/Ca^{2+} exchanger using different modeling approaches [77, 51].

Other flux expressions. We use the same flux expressions of the MK model, for the adenine nucleotide translocator (2.0.13) and the calcium uniporter (2.0.15) flux.

3.3 Simplification of fluxes and reactions rate expressions with new thermodynamical variables

The model discussed in section 3.2 is rather complex in terms of number of parameters and non-linearity of the flux expressions, which makes the fitting to experimental data mathematically impossible.

In this section we propose a model with simplified flux functions, which involve a reduced number of parameters, but still capture the same dynamics as the complete model. Indeed, each flux expression J_i derived previously in section 3.2 is a function of 1 or 2 model variables, except the ANT flux, function of 3 variables. So, it was possible to derive simpler expression for each of these flux by surface fitting, using as few parameters as possible.

More practically, we first plotted these flux expressions as function of their state variables. The shapes of these graphs lead us to propose simpler expressions, with fewer parameters, that

can reproduce the same dependencies. We then calibrated the parameters of the simplified expressions so as they fit the original ones. Bertram *et al.* had a similar approach [5]. However, we used surface fitting instead of several unidimensional fits, and performed the identification using a least-squares method on the whole domain spanned by the state variables. The simplified expressions are stated below and the calibrated set of parameters is listed in Table 3.5.

We also use the new state variables discussed in section 3.1 instead of concentrations, to write down the expressions of the simplified flux.

Oxygen consumption rate.

The oxygen consumption rate J_O defined in Equation (3.2.8) has a sigmoidal shape when plotted as a function of its variables $(\Delta E_{resp}, \Delta\psi)$. The proposed simplified expression for this rate is:

$$\tilde{J}_O(\Delta E_{resp}, \Delta\psi) = \sigma\left(\Delta E_{resp}, 0, \sigma\left(\Delta\psi, p_0, 0, p_1, p_2\right), p_3, \sigma\left(\Delta\psi, p_4, p_5, p_1, p_2\right)\right), \quad (3.3.1)$$

where

$$\sigma(x, s_1, s_2, k, x_0) = s_1 + \frac{s_2 - s_1}{2}\left(1 + \tanh\left(k\left(x - x_0\right)\right)\right)$$

is a sigmoid function transitioning from s_1 to s_2 around the threshold x_0 with slope k.

We restricted the fitting interval of ΔE_{resp} to $\left[\Delta E_{resp}(\varepsilon), \Delta E_{resp}(N_{tot} - \varepsilon)\right]$, with $\varepsilon = 10^{-2}$, as this variable goes to $\pm\infty$ for very low concentrations of NADH or NAD^+. The range of $\Delta\psi$ was set to $[100, 200]$ mV. In this state space, the relative l_2 error of the fit, which is given by $\frac{\|J_{original} - \tilde{J}_{fitted}\|_{l^2}}{\|J_{original}\|_{l^2}}$, was 0.014 (see Figure 3.6(a)).

ADP phosphorylation rate.

Similarly, the ADP phosphorylation rate J_{F1F0} from Equation (3.2.9) has a sigmoidal profile as function of each of its variables $\Delta G_{p,m}$ and $\Delta\psi$. We proposed the following simpli-

fied expression:

$$\tilde{J}_{\mathrm{F1F0}}(\Delta G_{\mathrm{p,m}}, \Delta\psi) = \sigma\left(\Delta G_{\mathrm{p,m}}, p_{10}, 0, p_{11}, p_{12}\right)\sigma\left(\Delta\psi, 1, p_{15}, p_{13}, p_{14}\right). \tag{3.3.2}$$

The fit was performed on the same interval for $\Delta\psi$, and $\left[\Delta G_{\mathrm{p,m}}(\varepsilon), \Delta G_{\mathrm{p,m}}(A_{\mathrm{tot,m}} - \varepsilon)\right]$ for the Gibbs free energy. The relative l_2 error for this fit was 0.056 (see Figure 3.6(b)).

Substrate metabolization.

The substrate metabolization flux expression (3.2.2) has 5 parameters. Using the change of variable (3.1.4), and plotting the resulting expression as function of its variables $([\mathrm{Ca}^{2+}]_{\mathrm{m}}, \Delta E_{\mathrm{resp}})$, we observed that it could be fitted by a simplified expression with 4 parameters:

$$\tilde{J}_{\mathrm{sub}} = p_6\left(1 - p_7\exp\left(-p_8[\mathrm{Ca}^{2+}]_{\mathrm{m}}\right)\right)\frac{1}{\exp\left(\frac{F}{RT}\Delta E_{\mathrm{resp}} - \ln(K_{\mathrm{resp}})\right) + p_9} \tag{3.3.3}$$

The mitochondrial calcium concentration range of variability was set to $[0, 4\times10^{-4}]$ nmol mgprot^{-1}, and the l_2 relative difference due to the fit was 0.006 (see Figure 3.5(a)).

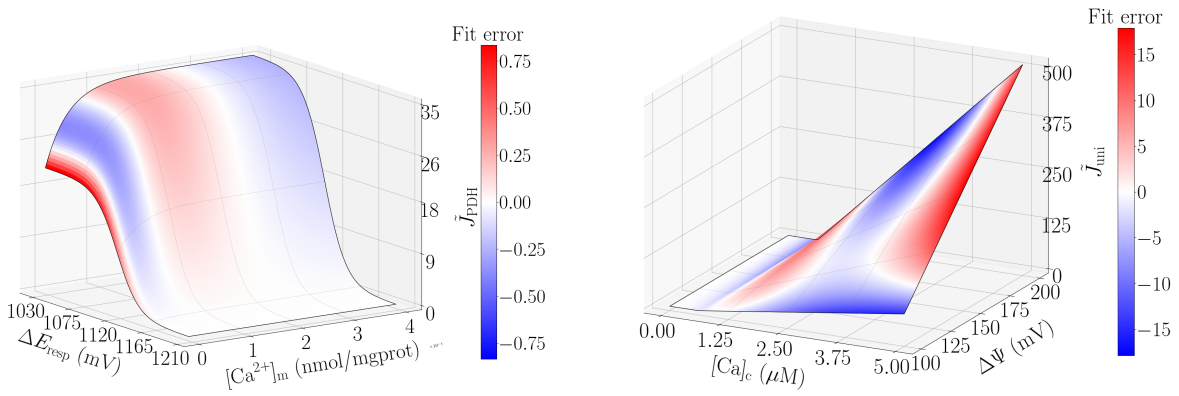

(a) (b)

Figure 3.5: Fit of the flux J_{sub} (3.5(a)) and J_{uni} (3.5(b)) defined in Equations (3.3.3) and (3.3.4), respectively.

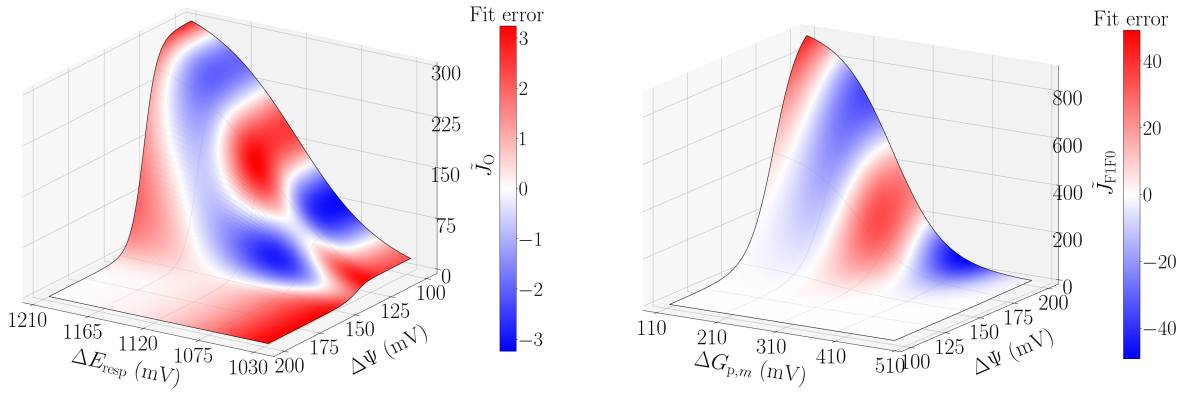

(a) (b)

Figure 3.6: Fit of the flux J_O (3.6(a)) and J_{F1F0} (3.6(b)) defined in Equations (3.3.1) and (3.3.2), respectively. The surface height quantifies the value of the flux and the fit error is computed as the absolute difference between the fitted and the original expressions.

Calcium uniporter.

Plotting the flux through the calcium uniporter as a function of $\Delta\psi$ and $[Ca^{2+}]_c$ suggested a product of two linear functions as a simplification. A limitation is that the calcium uniporter operates generally in one direction (from the cytoplasm to the matrix), and thus takes only positive values. For this reason, we chose to take only the positive part of that product:

$$\tilde{J}_{uni}([Ca^{2+}]_c, \Delta\psi) = \max\left(0, p_{24}(\Delta\psi - p_{25})([Ca^{2+}]_c - p_{26})\right) \tag{3.3.4}$$

Even though the simplified expression is not differentiable everywhere in its range of state variables, the original values were properly fitted with a relative l_2 error of 0.037 (see Figure 3.5(b)). The range of variation of the cytoplasmic calcium concentration was set to $[\varepsilon, 5]$ µM.

Other expressions.

The remaining flux expressions J_{NaCa}, J_{ANT} and J_{leak} were kept unchanged, with adaption to the new variables and grouping of their parameters:

$$\tilde{J}_{\mathrm{NaCa}}([\mathrm{Ca}^{2+}]_{\mathrm{m}}) = \frac{p_{22}[\mathrm{Ca}^{2+}]_{\mathrm{m}}}{p_{23} + [\mathrm{Ca}^{2+}]_{\mathrm{m}}}, \tag{3.3.5}$$

$$\tilde{J}_{\mathrm{ANT}}(\Delta G_{\mathrm{p,m}}, \Delta\psi, \Delta G_{\mathrm{p,c}}) = \frac{p_{16}\left(1 - p_{17}\exp\left(\frac{F}{RT}(\Delta G_{\mathrm{p,c}} - \Delta G_{\mathrm{p,m}} - \Delta\psi)\right)\right)}{\left(1 + \frac{p_{17}}{p_{18}}\exp\left(\frac{F}{RT}(\Delta G_{\mathrm{p,c}} - p_{19}\Delta\psi)\right)\right)\left(1 + p_{18}\exp\left(-\frac{F}{RT}\Delta G_{\mathrm{p,m}}\right)\right)}, \tag{3.3.6}$$

$$J_{\mathrm{leak}}(\Delta\psi) = p_{20}\exp\left(p_{21}\Delta\psi\right). \tag{3.3.7}$$

The parameter p_{20} and p_{21} associated the the proton leakage flux were computed by fitting the expressions (3.3.7) to the data from [45].

By deriving the ODE system (3.1.9) with the flux expressions described in the previous section, we rewrote a classic model of mitochondrial respiration and calcium handling with thermodynamical variables instead of concentrations. The complex functions from biochemical modeling describe all the molecular mechanisms involved in all flux. They were replaced by simpler phenomenological functions, in which the molecular mechanisms cannot be identified anymore. Yet these functions compare to the original ones up to a 5.6% difference in relative l^2 error and allowed for easier parameter calibration.

3.4 Solving the new ODE system

In order to solve numerically the ODE system (3.1.9) with the simplified flux expressions, we chose a robust, yet simple, numerical predictor-corrector scheme. The numerical method is described as follows: consider a system of first order ordinary differential equations

$$y' = f(t, y), \qquad y(t_0) = y_0,$$

an initial guess is computed via the Euler method, then this guess is improved using trapezoidal rule:

$$\begin{aligned} \tilde{y}_{i+1} &= y_i + hf(t_i, y_i), \\ y_{i+1} &= y_i + \frac{1}{2}h\left(f(t_i, y_i) + f(t_{i+1}, \tilde{y}_{i+1})\right), \end{aligned}$$

where h is the time step and was chosen equal to 10^{-5} min. This solver was implemented from scratch in Python, and produced an output in $\sim$ 100 seconds. Special care was taken for the variables ΔE_{resp} and $\Delta G_{\text{p,m}}$, since the change of variable introduced in section 3.1 maps the variables $[\text{NADH}]_{\text{m}}$ and $[\text{ADP}]_{\text{m}}$ in the bounded intervals $(0, N_{\text{tot}})$ and $(0, A_{\text{tot},m})$ to ΔE_{resp} and $\Delta G_{\text{p,m}}$ respectively, which both belong to the unbounded interval $(-\infty, \infty)$. Hence it could be numerically problematic if not treated with caution, especially for very low values of NADH and ADP.

3.5 Available experimental data, how it is linked to our model

Experiments

This section is written, in its entirety, by Emmanuel Suraniti, our collaborator, and a coauthor of the paper [71] from which this part A of the manuscript is adapted.

The experimental data were obtained as detailed in [16]. Cardiac mitochondria were extracted from Wistar Male rats (from Janvier Labs, France). Populations of isolated mitochondria were analyzed within the day following their preparation and subsequent determination of protein concentration by the Bratford method. All effectors of the respiratory chain used herein were first prepared as concentrated mother solutions (500 mM for the substrates of the respiratory chain, glutamate and malate, and 100 mM for ADP;

all compounds were purchased from Sigma France) in the specific respiration buffer for mammalian cardiac mitochondria. All solutions were kept on ice during the experiments.

The mitochondrial oxygen consumption rates were collected by chronoamperometry with a Clark electrode [59], which is the gold standard in bioenergetics. This electrochemical system determines the dissolved oxygen concentration of a liquid medium by measuring the current resulting from the 4-electron reduction of O_2 to H_2O on a platinum disk (at a potential of -0.8 V vs the internal Ag/AgCl reference electrode). O_2 diffused towards the platinum through a Teflon membrane protecting it from the solution. The Clark electrode was inserted in an oxygraphy chamber filled with 6 mL of respiration buffer under constant stirring, and thermostated at 28 degree C with a water gasket. Substrates of the respiratory chain were injected at 5 mM final concentration, then mitochondria were injected to reach a concentration of 0.4 mgprot mL^{-1} in the respiration buffer. ADP was further introduced at various concentrations (0.166 to 1 mM). The current at the Clark electrode was continuously measured, and the oxygen concentration determined by a simple proportionality factor (210 µM of O_2 maximum concentration). Figure 3.7 shows the experimental setup used to acquire data.

Among the available data, we selected those with substrates containing glutamate and malate. We could not select the data with succinate because it activates another complex of the respiratory chain that was not included in our model. We calibrated our model to the data of 5 representative experiments with different time instants and concentrations of ADP additions. A sixth data set was used to challenge the predictive properties of the model. Each data set gathers observations on the complete population of mitochondria in the oxygraphy chamber.

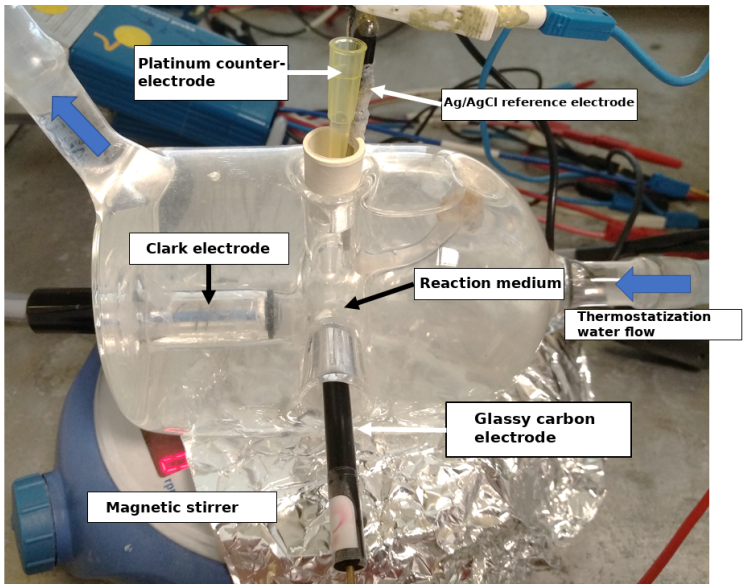

Figure 3.7: Oxygraphy chamber used to collect respiration data.

Link with our model

As explained in section 3.5, the measured experimental data reflect the evolution of the concentration of O_2 due to mitochondrial respiration, following successive ADP additions. Since the cytoplasmic calcium is not taken into account in this set of experiments, the calcium source term $[Ca^{2+}]_{ext}(t)$ is set to zero in the ODE system (3.1.9).

Each cytoplasmic ADP addition is modeled through the source term $J_{ADP,ext}(t)$, where

$$J_{ADP,ext} = [ADP]_c(t=0) + \sum_i [ADP]^+_{c,i}\left(1 - \exp\left(-\frac{t - t^+_{ADP,i}}{\tau^+_{ADP}}\right)\right)\mathbb{1}_{t>t^+_{ADP,i}}(t), \qquad (3.5.1)$$

with parameters $[ADP]^+_{c,i}$ and $t^+_{ADP,i}$ representing the ADP concentration and the time instant of the i-th ADP addition into the system, respectively. The parameter τ^+_{ADP} accounts for the diffusion of the ADP from the tip of the syringe to the mitochondria. This time is short (< 5 seconds) compared to the duration of the experiment, as there is an agitator at the bottom of the chamber. Although the parameters $[ADP]^+_{c,i}$ and $t^+_{ADP,i}$ are given by the experimental protocol, τ^+_{ADP} is an uncertain parameter since it depends on the way the

addition was executed, and can vary from one experiment to another. Nevertheless, in our simulations we set $\tau^{+}_{\mathrm{ADP}} = 0.05$ min, a reasonable constant value, since this parameter appeared not to be influential on the output of our model (see Fig. 4.5).

In order to complete the link between the experimental data and the observables of our model, we first computed the solution of the system (3.1.9) over the time interval $[t_0, t_f]$, where t_0 is the time where isolated mitochondria were added and t_f the end of the experiment. Then, substituting the state variables $(\Delta E_{\mathrm{resp}}(t), \Delta\psi(t))$ of the solution in (2.0.4), we computed the single oxygen atom consumption rate over the time interval.

In general, the results we obtained from simulations were close to the experimental data up to a multiplicative factor (usually between 30 and 40), accounting for various elements of the experiments that are not included in the model (*e.g.*the electrochemical process at the O_2 electrode). Moreover, our model does not account for the variability shown by mitochondria populations between experiments (different solutions, different life times, etc). For these reasons, our analysis focused on reproducing the ratios of respiration rates between different mitochondrial states rather than the absolute values of these rates.

Table 3.5: Parameters associated to the rates and flux of our model (section 3.3) computed from fitting to the original expressions (section 3.2).

Parameter	**Value**	**Unit**
p_0	3.222×10^2	nmol mgprot^{-1} min^{-1}
p_1	1.093×10^{-1}	mV^{-1}
p_2	1.330×10^2	mV
p_3	1.507×10^{-2}	mV^{-1}
p_4	1.119×10^3	mV
p_5	1.082×10^3	mV
p_6	3.530×10^1	nmol mgprot^{-1} min^{-1}
p_7	4.038×10^{-1}	dimensionless
p_8	2.300×10^4	mgprot nmol^{-1}
p_9	1	dimensionless
p_{10}	9.791×10^2	nmol mgprot^{-1} min^{-1}
p_{11}	1.171×10^{-2}	mV
p_{12}	2.588×10^2	mV
p_{13}	-5.596×10^{-2}	mV^{-1}
p_{14}	1.761×10^2	mV
p_{15}	-3.613×10^{-5}	nmol mgprot^{-1} min^{-1}
p_{16}	1×10^3	nmol mgprot^{-1} min^{-1}
p_{17}	8×10^{-1}	dimensionless
p_{18}	6.156×10^5	dimensionless
p_{19}	5×10^{-1}	dimensionless
p_{20}	2.740×10^{-3}	nmol mgprot^{-1} min^{-1}
p_{21}	5.245×10^{-2}	mV^{-1}
p_{22}	2.276×10^1	min^{-1}
p_{23}	3×10^{-3}	nmol mgprot^{-1}
p_{24}	1.006	min^{-1} mV^{-1}
p_{25}	8.4×10^1	mV
p_{26}	6.25×10^{-1}	nmol mgprot^{-1}

Chapter 4

Sensitivity analysis (SA) and calibration of parameters

Contents

Even though our model developed in the previous chapter is relatively simple, it involves 32 parameters overall. Hence, it remains very challenging to fit all these parameters to experimental data. Consequently, we proposed a calibration methodology that starts with a global sensitivity analysis, using Sobol indices, to eliminate parameters with small influence on the flux functions (sec. 4.2). In a second step, we performed the sensitivity analysis on the output of the model that can be directly linked to experimental data (sec. 4.4), which consisted in our case of oxygen consumption rates by isolated mitochondria (sec. 3.5). Finally (sec. 4.5), we used the results of this sensitivity analysis to calibrate the remaining parameters to experimental respiratory rates, using a genetic optimization algorithm.

4.1 Sobol analysis

Even though the proposed model in section 3.3 is simple and has only 32 parameters, some of these parameters may have small influence on the output of the flux or on the respiratory rates computed through the model. Setting these parameters to a fixed value somewhere in their range of variability reduces the number of uncertain parameters and hence is helpful for the calibration procedure. Among the wide variety of tools to perform sensitivity analysis, the Sobol method is effective for quantifying the influence of a certain parameter on the output of a model. Using the concept of variance decomposition of the output with respect to the parameters [67], it allows for global exploration of the parameters space, while taking into account their statistical distribution.

In practice, our model is an equation that can be written as $Y = f(p_1, p_2, \ldots, p_k)$ where Y is the output and $p_i, i \in \{1, \ldots, k\}$ are the parameters. The total Sobol index for a parameter p_i is $S_{T_i} = E[V(Y/p_{\sim i})]/V(Y)$, where $p_{\sim i}$ denotes all the parameters except p_i. This index quantifies the influence of the parameter p_i on the output of the model Y, relatively to the other parameters: the larger the value of the index, the larger the influence on the output. If $S_{T_i} \simeq 0$, then p_i can be fixed to any value in its distribution, without significantly affecting $V(Y)$.

Calculating the Sobol index associated to a parameter p_i is computationally expensive, because a large sampling of parameters is required, leading to a large number of model evaluations. To overcome this, we used the Saltelli sampling method [67] which reduces the total number of evaluations of f to $(k + 2)N_s$, where N_s is the number of parameter samples. All the Sobol indices were computed using a sample size $N_s = 2000$, thanks to the SALib Python library [34]. In the next sections, we first report the Sobol analysis on our simplified flux and rates expressions, then on the whole system (3.1.9). The first step gave us an indication on the relative influence of each parameter on its associated rate expression. The second step highlighted which parameters had an influence on the

respiration rates from the model, that were compared to the experimental ones thanks to the cost function D, given in section 4.3.

4.2 SA applied on fluxes and reactions rate expressions

In this section, we consider each flux from section 3.3 as a separate model that depends on state variables and some parameters. For each flux and each parameter, Sobol indices were computed using the same ranges of state variables as for the surface fitting procedure (*e.g.* Figures 4.2, 4.3, and 4.1). For the adenine translocator flux (3.3.6), it is not possible to plot trajactories in the phase space since its expression depend on three state variables. To integrate the sensitivity analysis performed on this flux expression with the other flux expressions, we computed the average and maximum of the total Sobol indices along a batch of 50 trajectories that were generated with random sets of parameters, each parameter being picked in a range of ±10 % around the value determined previously from the fits. The resulting indices are presented in Figure 4.4. From this bar graph, we set a minimum Sobol index of 0.1, under which parameters were considered constant without changing the outcome of the model. We then excluded the parameters p_0 ,p_1, p_3, p_8, p_{10}, p_{13}, p_{15}, p_{20} and p_{24} from our analysis.

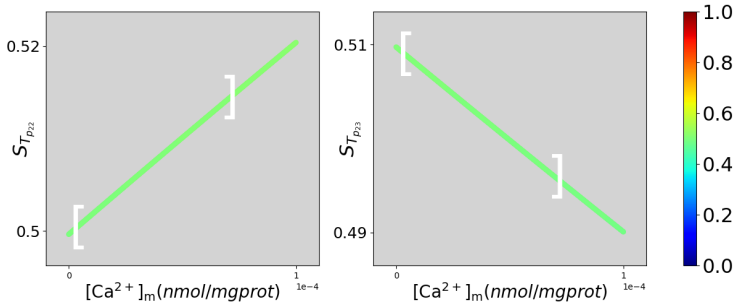

Figure 4.1: Total Sobol index for the parameter p_{22} (left) and p_{23} (right) of $\tilde{J}_{\mathrm{NaCa}}$ defined in Equation (3.3.5) plotted in function of its state variable $[Ca^{2+}]_m$. The white interval represents the domain of variation of trajectories computed with random samples of the whole set of parameters, on which we measured the Sobol index.

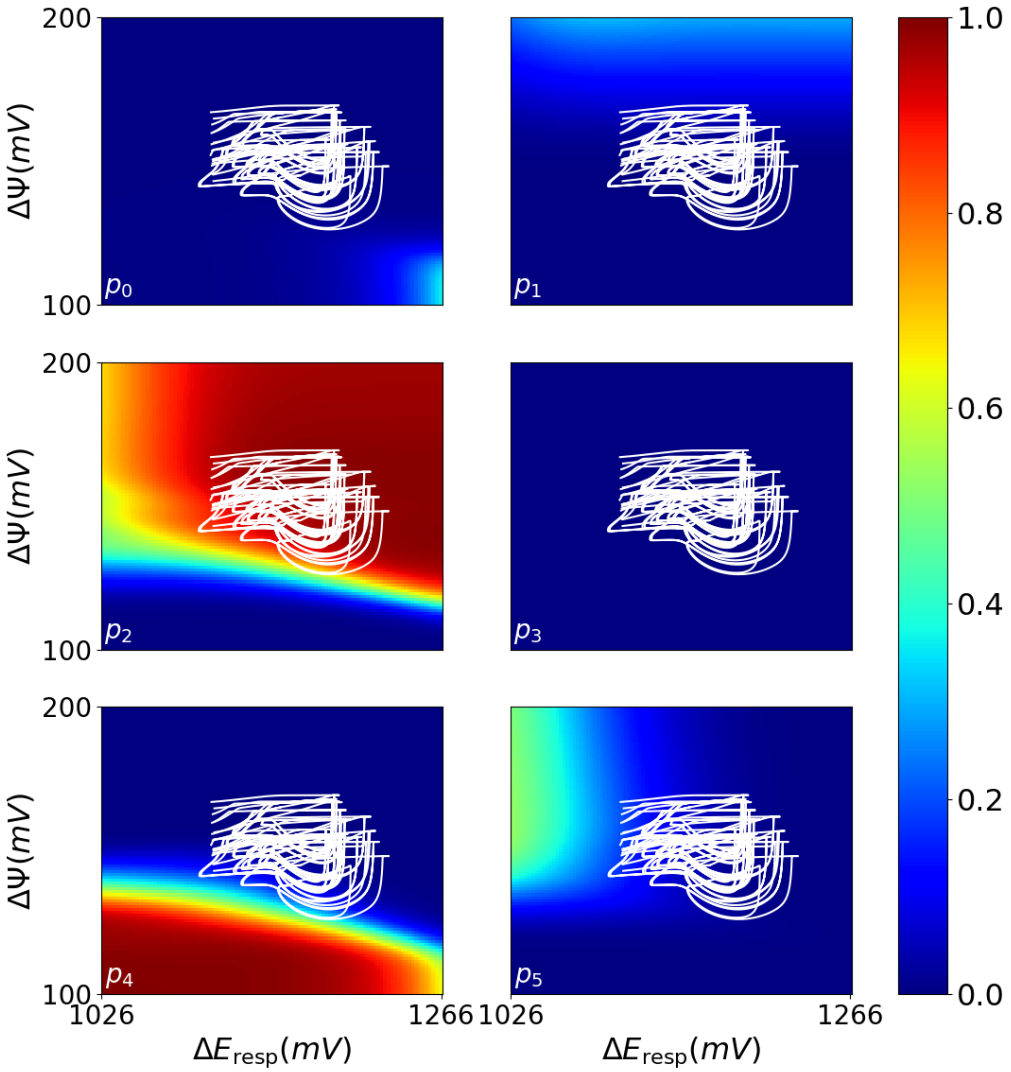

Figure 4.2: Total Sobol index for the parameter p_0 to p_5 of $\tilde{J}_O$ defined in Equation (3.3.1) plotted in the phase space $(\Delta E_{\text{resp}}, \Delta\psi)$. White lines are trajectories computed with random samples of the whole set of parameters, on which we measured the Sobol index.

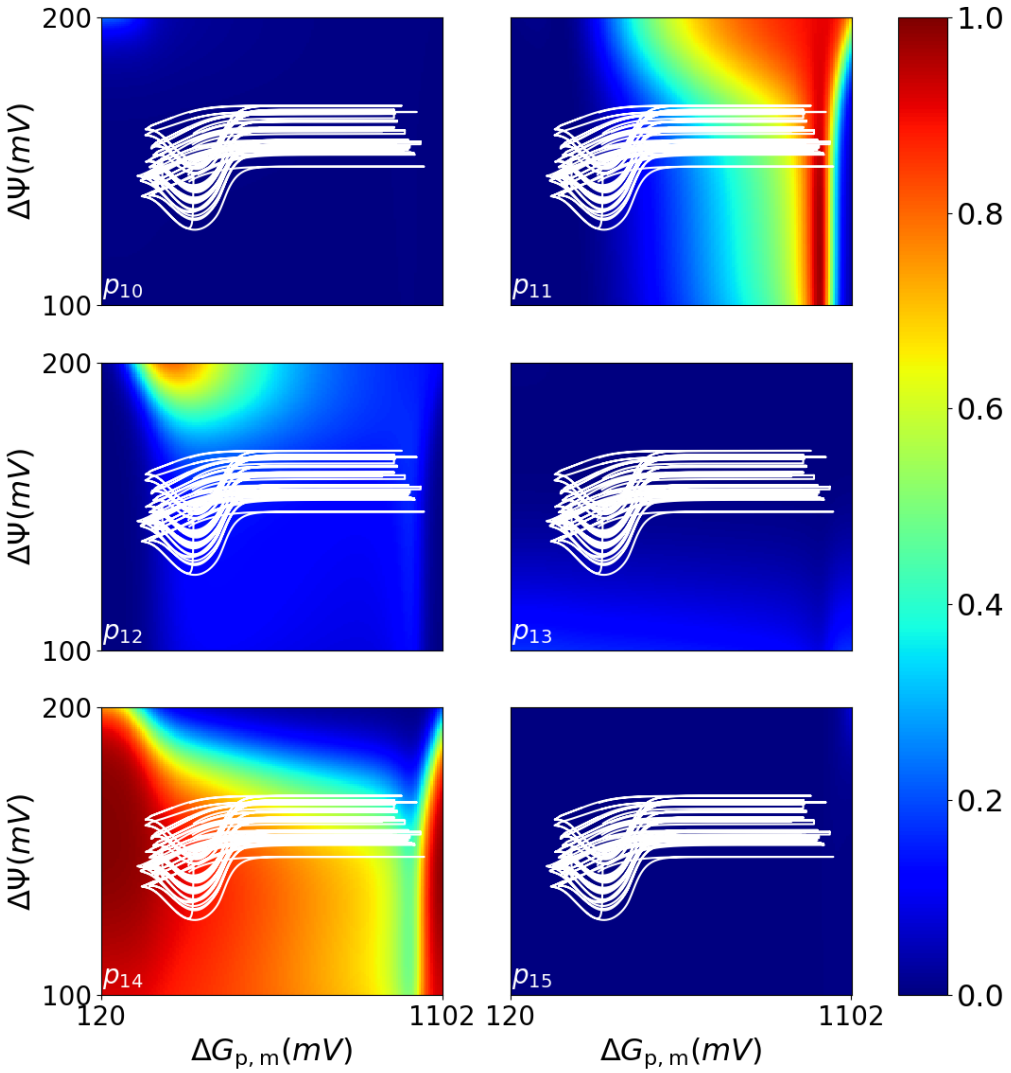

Figure 4.3: Total Sobol index for the parameter p_{10} to p_{15} of $\tilde{J}_{\mathrm{F1F0}}$ defined in Equation (3.3.2) plotted in the phase space $(\Delta G_{\mathrm{p,m}}, \Delta\psi)$. White lines are trajectories computed with random samples of the whole set of parameters, on which we measured the Sobol index.

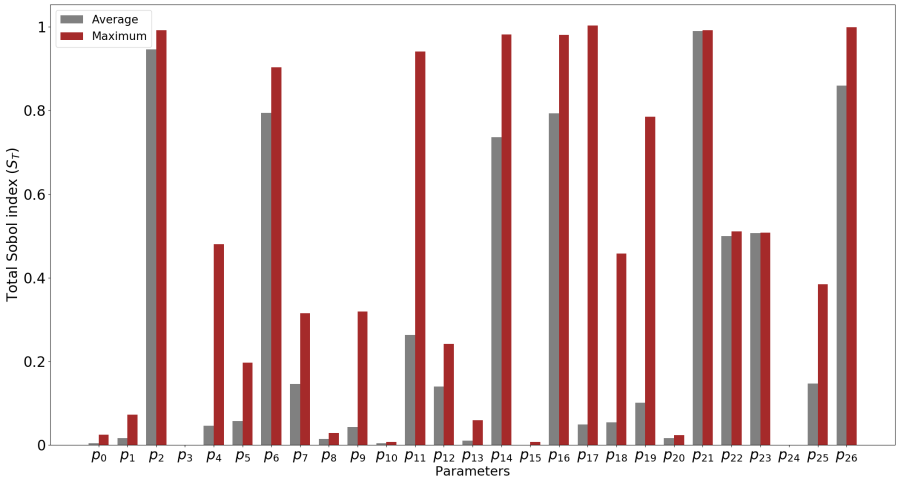

Figure 4.4: Average and maximum values of total Sobol indices for all parameters appearing in a flux function (Equations (3.3.1) to (3.3.7)). Each parameter contributes to a single flux function. Sobol indices were evaluated on 50 trajectories generated with random parameters.

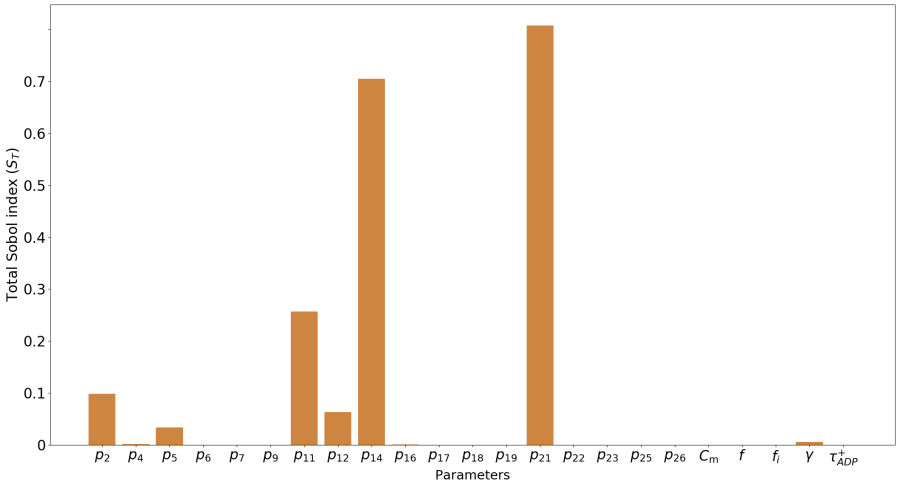

Figure 4.5: Total Sobol index representing the sensitivity of the cost function D defined in Equation (4.3.1) with respect to its parameters. The conditions used to compute these indices are of two consecutive additions of ADP at concentrations of 0.66 mM and 1 mM.

4.3 Choice of cost function for sensitivity analysis and data fitting.

The parameter sensitivity analysis and the calibration algorithm that will be described in sections 4.4 and 4.5 both rely on a cost function, which in our case will measure the discrepancy between the output of our model and experimental data. The choice of a cost function for these methods determines the properties of the solution. In particular, we are interested in reproducing the mitochondrial states that can be clearly identified on the experimental data (see Figure 4.6). These states are characterized by activity rates that are nearly constant and by short transitions that occur in between [12]. We then used a cost function designed specifically to reproduce those states.

Let us note I_k the intervals on which mitochondrial states can be identified and $J^*_{O,k}$ the corresponding respiration rates, which are obtained by linear fitting of the experimental data over the interval I_k. As explained in the previous section, we cannot compare directly the simulated and experimental absolute values of $J^*_{O,k}$, therefore each rate for $k > 0$ is normalized by the value for $k = 0$.

Our goal is to obtain simulated respiration rates $J_{O,k}$, $k > 0$, that are nearly constant on each interval I_k, with an accurate value. Then, the cost function can be formally written as:

$$D(P) = w_1 \sum_{k>0} \left(\frac{\overline{J_{O,k}}(P)}{\overline{J_{O,0}}(P)} - \frac{J^*_{O,k}}{J^*_{O,0}} \right)^2 + w_2 \sum_{k>0} \frac{1}{|I_k|} \int_{I_k} \mathbb{1}_{\frac{d}{dt} J_{O,k}(P) > \varepsilon}(s) \mathrm{d}s. \tag{4.3.1}$$

The first term of D is the difference between the experimental rates fitted over each interval I_k, and the simulated rates ($\overline{J_{O,k}}$) fitted over the same intervals. The second term measures the relative duration for which the derivative of $J_{O,k}$ is larger than a tolerance ε. The smaller this term gets, the more linear $J_{O,k}(P, t)$ is. The weights w_1 and w_2 balance the two terms. They were set to $w_1 = 0.04$ and $w_2 = 1$.

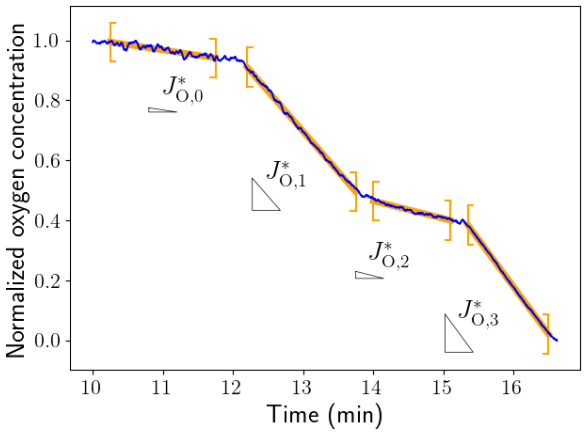

Figure 4.6: Targeted oxygen consumption rates $J^*_{O,k}$ (orange slopes) are plotted on top of experimental data (blue). Intervals I_k on which linear regressions were performed were picked manually for each experiment. On I_1 and I_3, after ADP additions, mitochondria are in the so called state 4 [12]. They are in state 3 on I_2, after ADP from the first addition is depleted. On I_0, mitochondria are in a state which is close to state 3 and which we call "substrate state", as there is no external ADP up to that point.

4.4 SA applied on simulated oxygen consumption rate

The final objective of our sensitivity analysis was to determine which were the influential parameters of the model, in order to calibrated them versus the experimental measurements of mitochondrial oxygen consumption rates (sec. 3.5). Having fixed the nine parameters that were identified in the previous section, we used the cost function D from Equation 4.3.1 as output of the model.

With a reduced total of 23 parameters (32-9), and using $N_s = 2\,000$ samples, the computation of the Sobol indices required 50 000 model evaluations. Even though this computational cost is high, each evaluation is independent of the others, so the task can be embarrassingly parallelized.

The results of the Sobol analysis are presented in Figure 4.5. Six parameters only ($p_2, p_5, p_{11}, p_{12}, p_{14}$, and p_{21}) appeared to have important influence on the output D.

4.5 Calibration of the model

Genetic algorithm and *a posteriori* evaluation

The calibration of the 6 previously identified parameters p_2, p_5, p_{11}, p_{12}, p_{14}, and p_{21} was required to be able to reproduce the experimental measurements as accurately as possible.

In addition to the six above parameters, we calibrated the parameter γ that accounts for the volume ratio between the mitochondria and the cytoplasm, and for the flux unit conversions.

The dimensionality of the problem and the non-smoothness of our model make the use of gradient-based calibration method not trivial. For this reason, we choose a genetic optimization algorithm to calibrate the parameters. We implemented the algorithm ourselves in Python (available in the supplementary materials).

Each generation of the algorithm consisted in a set of 1800 samples of parameters. As previously done for the sensitivity analysis, parameters were picked in a range of ±10 % around their base value, computed initially from surface fitting (see section 3.3). The function to be minimized is the cost function (4.3.1) that was discussed in section 4.3. The selection of sets of parameters that occurs at each iteration of the algorithm was based on truncation, where only the better half of the population (i.e. with lower values of the cost function) will eventually be passed to the reproduction phase. During this phase, crossover and mutation of parent parameters are applied with a probability equal 0.7 and 0.05 respectively. In the crossover operation, the weighting coefficient between the two selected sets of parameters is picked randomly in (0,1). The minimization was performed independently for the 5 experiments described in section 3.5, to account for the variability of the experiments (mitochondria, measurements, etc.).

The algorithm converged in 21 to 25 iterations. Convergence was considered attained

when $\left|\overline{D(P^{j+1})} - \overline{D(P^j)}\right| \leq 10^{-5}$, where P^j is the population of the j-th generation of the parameters $\{p_2, p_5, p_{11}, p_{12}, p_{14}, p_{21}, \gamma\}$. The functional D decreases from 5.33 to 2.52 on average. We run 2-3 repeats of the algorithm for each experiment, to reduce the probability of obtaining a local minimum. After having calibrated the parameters, we computed their average values and standard deviation across experiments. We also ran our model with these individual sets of parameters in order to make a direct comparison with the experimental data.

Table 4.1: Parameters of the model provided by the genetic algorithm, minimizing the cost function (4.3.1) on 5 different sets of experimental data.

Parameter	**Unit**	**Average**	**Standard deviation**
p_2	mV	1.314×10^2	1.15
p_5	mV	1.035×10^3	7.32
p_{11}	mV	1.194×10^{-2}	1.76×10^{-4}
p_{12}	mV	2.823×10^2	1.52
p_{14}	mV	1.7×10^2	2.58
p_{21}	mV^{-1}	5.502×10^{-2}	1.38×10^{-3}
γ	dimensionless	1.057×10^{-2}	1.007×10^{-3}

Results

The values of the calibrated parameters are reported in Table 4.1, averaged over the five available experiments. With the exception of the volume ratio γ, the variability of the parameters across experiments is low ($\sim 2\%$). This suggests that our model is robust for the modeling experiments on populations of isolated mitochondria.

Figure 4.7 shows the comparison between our model run with calibrated parameters and respiration data. Our model reproduces the quick transitions between respiratory states of the mitochondria.

However, when the small quantities of ADP are added (Figure 4.7(d) and 4.7(e)), it is

more difficult to identify the slope corresponding to mitochondrial state 3, and our model hardly reproduces the experimental data. This is confirmed when plotting the simulated respiration rates on top of the values fitted from data, as shown in Figure 4.8. It is also likely that the fitted respiration rate could not be one of a theoretical population of mitochondria which are all in the same state at all times. Nevertheless, the simulations correctly identified the periods of time when mitochondria are in state 3 or 4, even for these difficult conditions.

We recall that the cost function used for calibration is derived to recover the ratios between respiration rates, instead of their absolute values. Thus, the simulated results plotted in Figures 4.7 and 4.8 were scaled by a constant value determined during the initial mitochondrial inactivated state (before any addition).

Additionally, the very sharp transitions of the simulations shown in Figure 4.8, cannot be seen on the experiments. This is expected as well, since the experimental measurement system displays a response-time (of about 1 second) and because a population effect tends to smoother the total respiration of all mitochondria.

In order to assess the predictive properties of our model, we ran a simulation with the averaged parameters given in Table 4.1. In Figure 4.9, we compare the output of the model with a sixth separated experimental data set, which was not used for calibration. There is good agreement between the two time series. It is confirmed by the fact that the value of the cost function is 2.44, which is lower than the average 2.52 obtained at the end of the calibration.

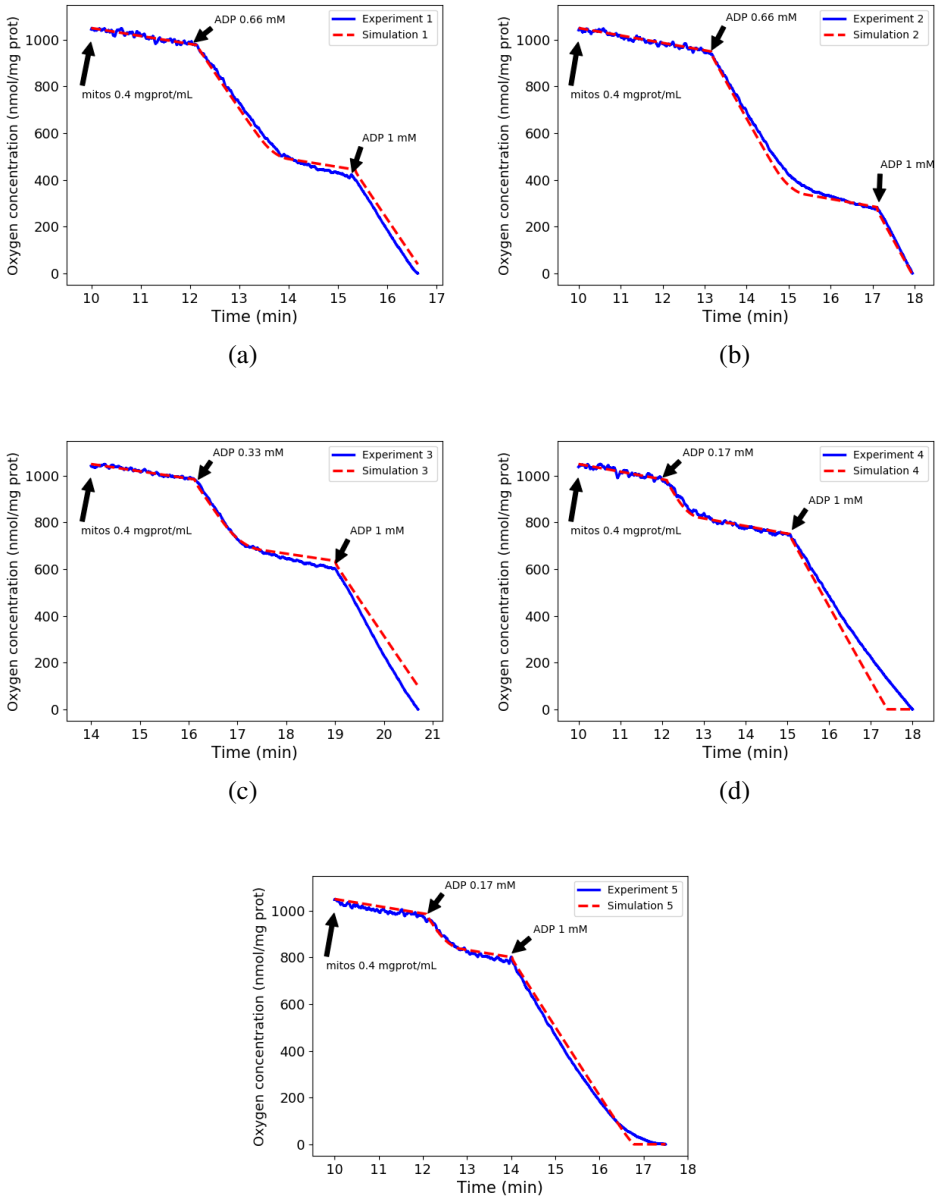

Figure 4.7: Calibrated oxygen consumptions (dashed red lines) compared to data from 5 experiments (blue solid lines). Arrows locate additions of mitochondria then ADP at two time instants.

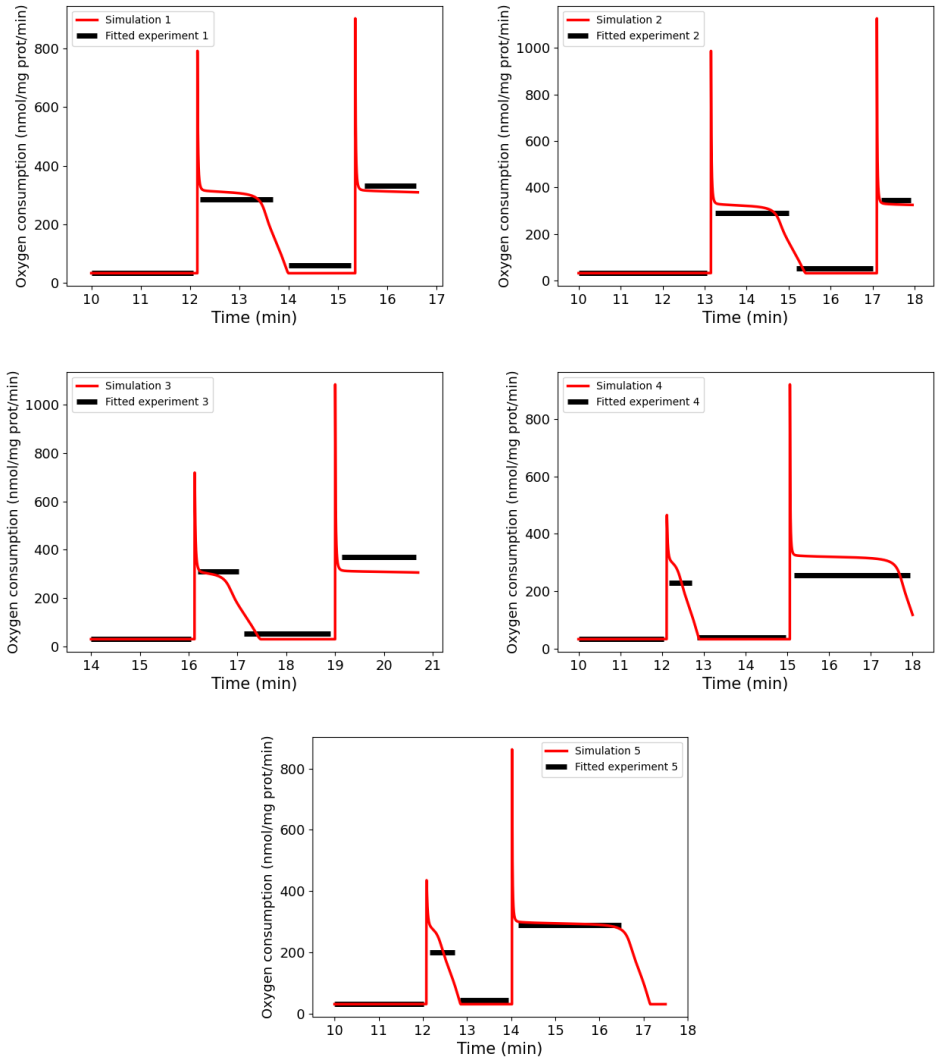

Figure 4.8: Calibrated respiration rates (red) compared to the rates fitted on experimental data (black), as described in section 4.3. The target respiration rates are only plotted on the intervals used to fit experimental data, and also used in the computation of the cost function.

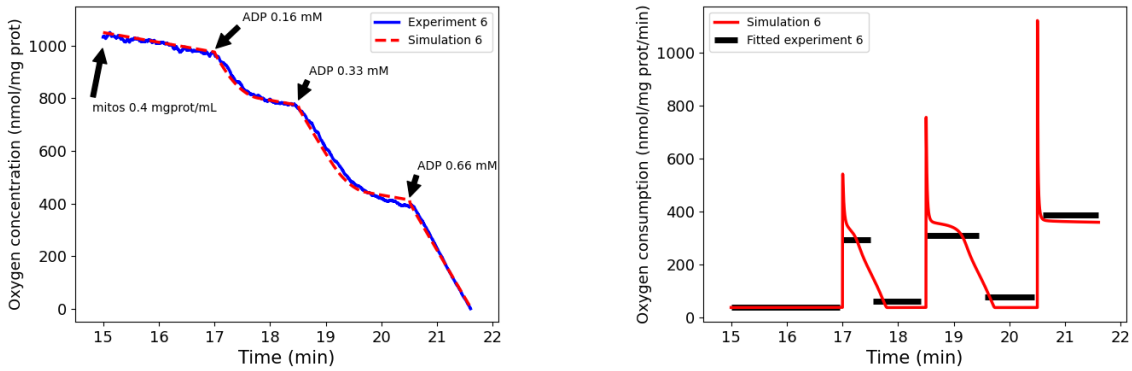

(a) (b)

Figure 4.9: Comparison between experimental data and a simulation using average parameters calibrated from five other experiments. 4.9(a): oxygen concentration, 4.9(b): respiration rates.

4.6 Discussion

We proposed a simple model of cardiac mitochondrial activity, including ATP production through oxidative phosphorylation and calcium handling. The model has simple mathematical expressions that were fitted to revised versions of the more complex MK equations.

The fact that the parameters of the MK model were set for pancreatic β cells can be seen as a limitation of our model. However, all those parameters are now grouped under our new flux functions parameters, which were eventually calibrated to respiration data of cardiac mitochondria from rats. Therefore, the origin of the parameters is not a major concern as we showed that they can be fitted to other types of cells. Nevertheless, parameters associated with the calcium handling were not calibrated in this work, because of lack of associated data. The ability of the model for accurate predictions for calcium associated mechanisms is yet to be confirmed.

Another possible limitation of our simplified model is that its parameters do not have a direct biological meaning, like the parameters in models based on physics or physiology. However, this is offset by the robustness of our model, which cannot be overfitted. This was confirmed by the sensitivity analysis that was performed on the flux expressions, where only 9 parameters appeared to be non-influential (at least for the experimental setups that we considered). This indicates that the simplified expressions balance correctly the complexity of the observations.

We further made use of the available experimental data to perform a global sensitivity analysis, based on Sobol indices, on the respiration rates. In this step, a lot more parameters were excluded, which is explained by the sparsity of the experimental data at hand. In fact, this second sensitivity analysis step was an informal indicator of the non-identifiability of most of the parameters, with respect to respiration rates data. The choice for the Sobol method was motivated by its ability to highlight the interactions between the parameters. We also wanted to use a method that was able to analyze the entirety of our set of parameters in one go, and to account for the fact that they are statistically distributed. Our model with few parameters allowed for the use of such a computationally expensive method. With a very descriptive but highly complex model, we may have been able to conduct an analysis on a subset of parameters only, as done for example by Wu *et al.* [79].

In our work, the seven influential parameters that were identified from the sensitivity analysis were calibrated separately, using an optimization algorithm, to five data sets of respiration rates controlled by different concentrations of ADP addition. Then the prediction capability of our model was assessed on a sixth data set that was not used in the calibration. Results show that our model is capable of reproducing respiratory states of cardiac mitochondria, and the transition between them, as described by biologists.

The methodology that we developed and tested with experimental data on mitochondrial respiration activities can be applied to other types of data sets. For instance, other parameters can be determined with data on external calcium or ATP/ADP concentrations. Ultimately, all the parameters of the model may be determined, with the certainty that the

- model will not be overfitted.

Part II

Permeability transition pore

Chapter 5

State of the art

Contents

The first observations of the mitochondrial permeability transition pore (mPTP) date from the 1960s, where it was shown that matrix calcium could cause an increase in the permeability of the inner mitochondrial membrane of bovine hearts [49, 15, 29, 37]. Indeed, the relationship between calcium and mPTP is extensively studied in the literature, because calcium is known to be a principal activating factor of the mPTP. However, it is not the only regulator as we will see later on. The mPTP is shown to be a non-specific pore that allows the passage of any molecule smaller or equal to 1.5 KDa [37, 24]. Its size is approximately 2 nm. The exact structure of the mPTP is still a subject of debate, even if several hypothesis about its structure were proposed. These hypothesis were reviewed recently in [39]. However, in this manuscript we wont focus on the structure of the mPTP. What will be interesting for us is its operating modes and some of its regulators.

5.1 Two operating modes for the mPTP

Sustained opening

When it was first discovered, the mPTP opening was thought to be irreversible. That means that once the pore is activated, it will stay open. This opening is characterized by a large conductance that will cause a collapse in the mitochondrial membrane potential, uncoupling of the respiratory chain and the entrance of water in the matrix. The whole process ultimately results in the release of mitochondrial contents into the cytosol, a rupture of the mitochondrial outer membrane, a drop in the osmotic pressure of the matrix solutes, and finally the death of the mitochondria.

On the cellular scale, this will lead to the depletion of cellular ATP, and ultimately to necrotic cell death [30, 42]. This irreversible opening of the pore has been linked to several pathologies including ischemia reperfusion injury and cancer [61, 7].

Transient opening

More recently, studies have shown a new transient type of mPTP opening which does not lead to the death of the mitochondria and whose role could be physiological [50, 76, 63]. This opening mode is sometimes called flickering. In fact, the transient mPTP opening could serve as a rapid mitochondrial efflux for excess calcium and reactive oxygen species (ROS) [80, 47]. While the sustained opening mode is associated with a total collapse of the mitochondrial inner membrane potential, it has been shown that while in the flickering mode the membrane potential is only transiently depolarized [41]. Indeed, this opening mode would cause a fall of membrane potential as well as an uncoupling of the respiratory chain, and consequently a shutdown of ATP production. However, these effects would only be transitory since the pore would be able to close, thus allowing the mitochondria to reconstitute its membrane potential and ATP production. This transient operating mode could be involved in the control of calcium fluxes and ROS. Physiologically, while in the cardiac relaxation phase, the transient mPTP could be a key player in the exclusion of the mitochondrial calcium as discussed in the hypothesis in

Fig. 1.4. That means, the mPTP could be a factor that helps in avoiding a calcium overload within the mitochondrial matrix and thus maintaining the calcium homeostasis [25].

5.2 Regulators

The list of activators and inhibitors of the mPTP is large, and their mechanisms, that can often be complex, are still debated for some of them. We will not be able to discuss them all in this manuscript. However, we will list the most studied ones, to our knowledge. For a more complete list of mPTP regulators, the interested reader is referred to [39].

The mitochondrial membrane potential

While some agents are activators and others are inhibitors, the mitochondrial membrane potential is known to be able to both activate or inhibit the mPTP. Indeed, when the mitochondrial membrane potential is elevated, it inhibits the opening of the mPTP, whereas when its magnitude is low it is thought to trigger the mPTP opening [38].

Activators

Calcium

As we previously mentioned, calcium is the key activator of the mPTP. In fact, The mPTP has a cation binding site, which when filled with enough calcium will act as an activator. The matrix calcium concentration needed for the pore oprening is thought to be between 100 – 200 $\mathrm{nmol\,mg^{-1}\,mL^{-1}}$ [29, 37].

Reactive oxygen species (ROS)

The generation of ROS in the mitochondria primarily occurs in the respiratory chain. It is mostly due to a binding of an electron, leaked from the electron transport chain, to dioxygen. This forms the superoxide anion $O_2.^-$.

It has been shown that ROS can increase the mPTP activity [33]. Additionally, ROS can also

modulate the free intracellular calcium levels to be taken by mitochondria by several mechanisms (*e.g.* activating plasma membrane influx, ...), and thus increase the mPTP activity.

Other activators of the mPTP include cyclophilin D (CsD), inorganic phosphate (Pi) and Atractyloside [39].

Inhibitors

The most known and studied inhibitor of the mPTP is Cyclosporine A (CsA) which is an immunosuppressive agent. It works by blocking CsD from binding to the pore [26]. Divalent cations such as Mg^{2+}, Mn^{2+}, and Sr^{2+} are also known for inhibiting the mPTP. They work by competing with calcium for a shared site on the mPTP in the matrix [3]. They can also inhibit calcium entrance into the mitochondria [74]. Other inhibitors of the mPTP include Benzodiazepines, Bongkrekic Acid and acidic matrix pH. In summary, most of the mPTP inhibitors act directly or indirectly through an interference with calcium.

5.3 Mathematical models that include mPTP or ROS

Mathematical models that incorporate the mPTP were developped using mainly two conceptual approaches. The first one is a population dynamics approach were mitochondria are charachterized by some states of interest, mainly related to the mPTP. In these kind of models, state variables are fractions of these mitochondrial states. For example Chapa-Dubocq *et al.* [14], developed a population model of mitochondria where the mPTP is studied through the correspondent state of mitochondria swelling. In their model they partitioned their population into four subpopulation representing : negligible swelling, mitochondria containing calcium, reversible swelling, and irreversible swelling. The transition between these states was principally regulated by calcium. They were able to fit the kinetic parameters in their model, representing thresholds of transitions between the different states, to experimental data of mitochondrial swelling.

The second approach consists in defining a state variable representing the permeability of the

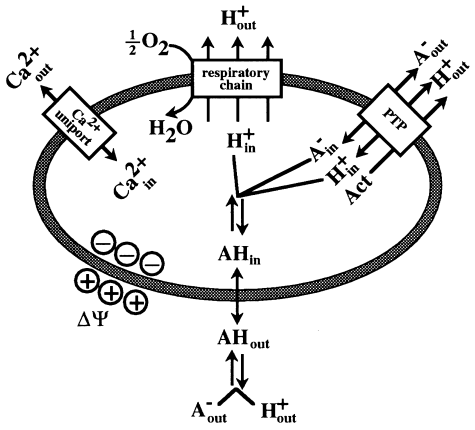

Figure 5.1: Schematic representation of the Selivanov *et al.* model [69] components.

mPTP in one or both of its states, and adding this variable to classical models of mitochondrial energy metabolism and calcium transport. This approach is surely more adapted to our aim, since we already developed a minimal mitochondrial model (see chapter 3) that accounts for classical mechanisms, and our next objective is to incorporate to it the mPTP functioning. Next we review some of the literature models that were developed following this approach.

The Selivanov *et al.* model

In 1998, Selivanov *et al.* [69] proposed a minimal mitochondrial model that incorporates mPTP in its low conductance mode. Their model illustrates the mPTP related Ca^{2+}-induced Ca^{2+}release. In their model they considered the following main components : the respiratory chain, the mPTP, the calcium uniporter, and the movement of weak acids across the mitochondrial membrane (Fig. 5.1). With these components, five state variables were considered : the cytoplasmic calcium concentration, the membrane potential, protons concentration in the matrix, the amount of opened PTP channels, and the matrix concentration of respiratory chain activators. Three main factors contributing to the regulation of the mPTP were considered :

- an increase in the matrix calcium concentration
- a decrease in the mitochondrial membrane potential

- an increase in the matrix pH.

These three factors were considered as both ways regulators. That means that the inverse functioning of these factors promotes the closure of the mPTP. However, not all of the three factors were considered as direct regulators. Indeed, only the pH was considered to influence the mPTP directly whereas the membrane potential and the concentration of calcium in the matrix were considered as indirect regulators. Their model was based on the following formulation. First the cytoplasmic calcium enters the mitochondria through the Ca^{2+}uniporter which causes a transient drop in the mitochondrial membrane potential. This drop activates the respiration and thus increases the number of protons pumped outside the mitochondria resulting in the alcalinization of the matrix. The mPTP is then activated by the fact that the matrix pH has increased. This triggers the ion fluxes according to their potential gradients. The activation of mPTP also causes inhibition of the respiration which contributes to matrix acidification that eventually inactivates the mPTP.

Even though the ATPase activity and the calcium transport through the Na^{+}/Ca^{2+}exchanger were not considered in their model, it was able to reproduce calcium spiking and oscillation observed experimentally when the mPTP is working in its low conductance mode. However the fact that, in their model, calcium was not considerded as a direct activator of the mPTP could be debated especially since several experimental studies suggested the opposite [29, 37].

The Pokhilko *et al.* model

Several years later, in 2006, Pokhilko *et al.* [65] developed a mitochondrial model for ion transport, that includes the mPTP. Their aim was to analyze different modes of calcium uptake. In their model, fluxes of ions and the state of the mPTP were described in five compartments (Fig. 5.2) :

- transport of protons
- calcium transport
- potassium transport

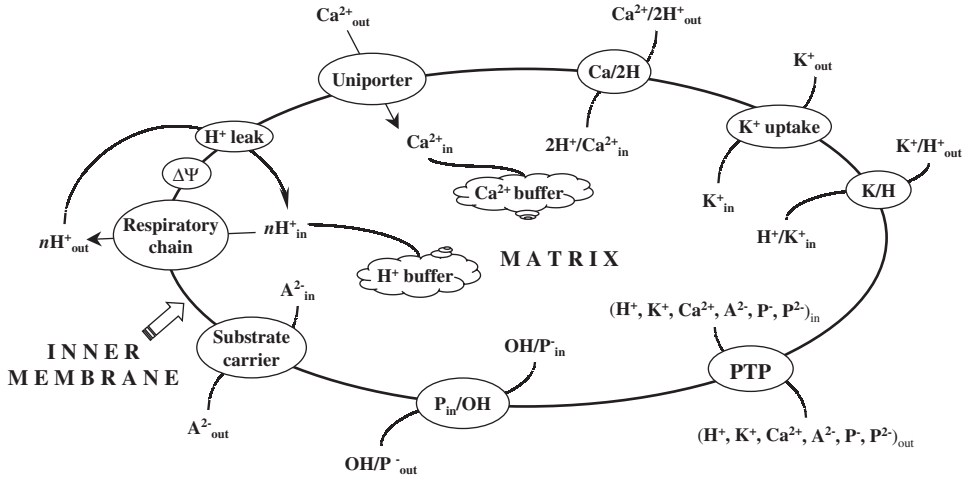

Figure 5.2: The compartments and ion fluxes included in the Pokhilko *et al.* model [65].

- anions transport (*e.g.* phosphate transport, oxidative substrate transport)

- mitochondrial permeability transition pore.

Concerning the mPTP in their model, it was regulated by matrix Ca^{2+}, protons, membrane potential, and fluxes of ions through it. The dynamics of the fraction of opened mPTP was adapted from the work of Selivanov *et al.* [69] using an ordinary differential equation as follows :

$$\frac{\mathrm{d}}{\mathrm{d}t}\mathrm{T_{op}} = k_{\mathrm{op}}[\mathrm{Ca}^{2+}]_{\mathrm{m}} p_1(\Delta\psi)(1-\mathrm{T_{op}}) - k_{\mathrm{cl}}\mathrm{T_{op}} p_2(H^+), \tag{5.3.1}$$

where $\mathrm{T_{op}}$ is the fraction of open mPTP, k_{op} and k_{cl} are the rate constants of the mPTP opening and closure. The functions p_1 and p_2 describe the dependence of the opening and closure rate of the mPTP on the membrane potential and the protons respectively. The dynamics of the mPTP is written in a way that the rate of opening (first term in eq. 5.3.1) is proportional to the fraction of closed mPTP, and the rate of closure of the mPTP (second term in eq. 5.3.1) is proportional to the fraction of open mPTP.

Using the equation 5.3.1 for solving the steady state equation

$$\frac{\mathrm{d}}{\mathrm{d}t}\mathrm{T_{op}} = 0, \tag{5.3.2}$$

with respect to the variable T_{op} leads to the steady state solution

$$T_{op,\infty} = \frac{1}{1 + \frac{k_{cl} p_2(H^+)}{k_{op}[Ca^{2+}]_m p_1(\Delta\psi)}}. \tag{5.3.3}$$

This solution varies between zero (low conductance mPTP) and one (high conductance mPTP) if $k_{op}[Ca^{2+}]_m p_1(\Delta\psi)$ and $k_{cl} p_2(H^+)$ are of the same sign. More generally the terms leading $(1 - T_{op})$ and T_{op} need to be of the same sign. These terms are the rate constants of the opening and closure multiplied by functions representing the dependence of the opening and closure on the considered regulators.

Using this model, they were able to show that the kinetics of the mitochondrial Ca^{2+} uptake is dependent on two factors: the total amount of Ca^{2+} in the system, and the rate of Ca^{2+} infusion. Additionally they were able to provide Ca^{2+} thresholds for transitioning between the different mPTP operating modes.

Even though this model still does not account for the ATPase activity and the calcium transport through the Na^+/Ca^{2+}exchanger, it is more complete than Selivanov *et al.* model in terms of incorporating most of the mitochondrial ions transport. This could be useful when the goal of the model is to improve our understanding of the ions transport, in particular in the presence of the mPTP. However, if the purpose of modeling the mPTP is not primaraly related to the different ions transport in the mitochondria, more simplification could have been done. This is by eliminating the explicit variables representing the ions, and keeping only their influence on the membrane potential. This is what has been done by Wacquier *et al.* [75].

The Wacquier *et al.* model

In their model, Wacquier *et al.* [75] adopted almost the same modeling formulation of the mPTP used in the models of Selivanov *et al.* and Pokhilko *et al.* . However, the regulators influence on the opening and closure of the mPTP were slightly different. The considered regulators of the mPTP were only the concentration of matrix calcium and the membrane potential. The evolution equation of the fraction of open mPTP (denoted PTP) is triggered when the membrane potential falls below a certain threshold, that depends on the matrix calcium concentration, and

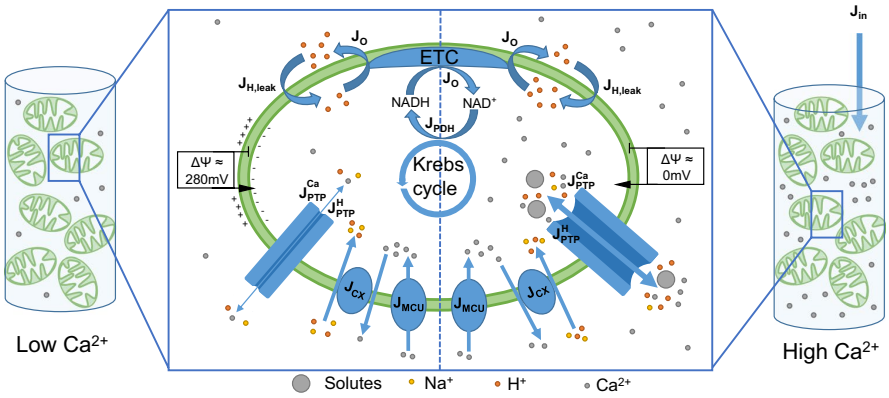

Figure 5.3: Schematical representation of the mechanisms and ion fluxes included in the Wacquier *et al.* model [75].

can be written as follows :

$$\frac{\mathrm{d}}{\mathrm{d}t}\mathrm{PTP} = V_{\mathrm{op}}(1-\mathrm{PTP})\frac{1}{1+\exp\left(\frac{\Delta\psi - q_{op}[\mathrm{Ca}^{2+}]_{\mathrm{m}}}{q_s}\right)} - k_{\mathrm{cl}}\mathrm{PTP}. \tag{5.3.4}$$

In equation 5.3.4, the closure rate is described as a linear function, and the dependence of the rate of opening, on the membrane potential and the calcium, is a highly non-linear function. The parameters q_{op} and q_s influence the threshold and the slope of the dependence of PTP opening on $\Delta\psi$. In contrast to Pokhilko *et al.* model, they did not consider ions as state variables (except for the cytoplasmic and matrix calcium concentrations), but still kept the protons flux influence on $\Delta\psi$ via the mPTP. In their model, the relationship between the mPTP and $\Delta\psi$ is a positive feedback loop, that is controlled by Ca^{2+}. That means that first Ca^{2+} controls the threshold at which $\Delta\psi$ starts inhibiting the mPTP. Then, while high $\Delta\psi$ prevents the pore from opening, this opening dissipates $\Delta\psi$ due to ion leakage across the mitochondrial membrane. The fluxes and mechanisms considered in their model are illustrated in Fig. 5.3.

On the other hand, the fluxes considered in their model via the mPTP were written using a simplified version of the Goldman-Hodgkin-Katz equation. Thus these flux expressions depend on the ions electrochemcial gradients and on the state of the mPTP as follows :

$$J_{PTP}^{Ca} = V_{PTP}^{Ca}.\mathrm{PTP}.\frac{[\mathrm{Ca}^{2+}]_{\mathrm{m}} - [\mathrm{Ca}^{2+}]_{\mathrm{c}}}{1+\exp\left(\frac{s_1-\Delta\psi}{s_2}\right)}, \tag{5.3.5}$$

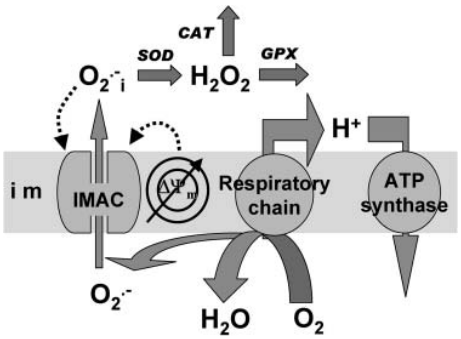

Figure 5.4: The mitochondrial bioenergetics model of Cortassa *et al.* [18] illustrating the considered ROS production, transport and scavenging mechanisms. Abbreviations: im (inner mitochondrial membrane), IMAC (inner membrane anion channel), CAT (catalase), SOD (superoxide dismutase), and GPX (glutathione peroxidase).

$$J^H_{PTP} = V^H_{PTP}.\mathrm{PTP}.\frac{1}{1+\exp\left(\frac{s_1-\Delta\psi}{s_2}\right)}. \tag{5.3.6}$$

Since protons concentration is not a state variable in their model, it does not appear in equation 5.3.6, and it is implicitly included in the parameter V^H_{PTP}. This model was validated against experimental data of rat hepatocytes. It was able to reproduce the long lasting opening of the mPTP after several addition of calcium concentrations in the medium.

Cortassa *et al.* model

Cortassa *et al.* [18], in 2004, incorporated ROS mechanisms (mitochondrial ROS production, cytoplasmic ROS scavenging (reaction of ROS with antioxidants), and ROS activation of inner membrane anion flux) to their previously developed model of cardiac mitochondrial bioenergetics (see chap. 2). The aim of their model was to test, using a computational model, the influence of the balance between superoxide anion efflux and the intracellular ROS scavenging capacity on the mitochondrial oscillatory mechanism. These mitochondrial oscillations (of membrane potential, ROS production and NADH concentrations) are observed in isolated cardiomyocytes, and are known to contribute to energetic and electrical dysfunction in pathological context such as ischemia-reperfusion.

Mitochondrial ROS production was considered as a side path of electrons leaking from the

electron transport chain and binding to an oxygen molecule, leading to superoxide anion $O_2.^-$. These are then transported to the cytoplasm through the inner mitochondrial membrane anion channel, that is postulated to be activated by by cytoplasmic superoxide anions (Fig. 5.4).

In this model, unlike in the previously discussed models in this chapter, the ATPase activity was taken into consideration. However the mPTP activity was not considered, not being one of the study aims. Since the authors were interested in the balance between ROS production and scavenging, they were constrained to add state variables representing both matrix and cytoplasmic ROS concentrations. In addition, they were obliged to model the ROS transport through the IMAC (inner membrane anion channel).

Several simplification hypothesis could be done to this model, depending on the modeler study objectives. This will be discussed in the next chapter where we adapt some of the models, discussed here, to extend our previously introduced model to make it account for both mPTP activity and ROS.

The Kushnareva *et al.* model

Another model for ROS production was proposed by Kushnareva *et al.*in 2002 [46]. In their model, they proposed that the rate of ROS production in the mitochondria is determined by the concentration of the site of superoxide generation (denoted *ROS). The variation of superoxide anion concentration in function of time could be then written as follows:

$$\frac{\mathrm{d}}{\mathrm{d}t}[O_2.^-] = k[O_2][^*ROS^{\cdot -}], \tag{5.3.7}$$

where $^*ROS^{\cdot -}$ is the reduced form of the latter site, and k is the second order rate constant. They further assumed that the redox state of *ROS site is controlled by the thermodynamics of the redox couple NADH/NAD^+. This model was built based on evidence obtained from isolated mitochondria of rat brain and heart. Even though its formulation is simple, it is thought to be not able to reproduce experimental results in intact myocytes [18].

Summary, discussion and conclusion of the literature models

Each one of these previously discussed models has contributed to our understanding of different aspects of the mPTP or ROS. In most of the models that incorporated the mPTP, the evolution of the variable representing this pore was described almost in the same way. This variable represented the fraction of open mPTP and it was modeled using the following type of differential equation:

$$\frac{\mathrm{d}}{\mathrm{d}t}\mathrm{P} = k_{\mathrm{op}}(\text{activators})(1-\mathrm{P}) - k_{\mathrm{cl}}(\text{inhibitors})\mathrm{P}, \tag{5.3.8}$$

where P is the variable that represents the fraction of open mPTP, k_{op} is the rate of opening that can depend on the considered activators, and k_{cl} is the rate of closure that can depend on the considered inhibitors. The only differences were in the types of the considered regulators, and how they were modeled. Almost all of these models considered the mitochondrial membrane potential difference ($\Delta\psi$), the matrix calcium concentration ($[Ca^{2+}]_{\mathrm{m}}$), and sometimes the pH difference as regulators of the mPTP either in a direct or indirect way. The fluxes of ions via this pore were modeled using a simplified version of the Goldman-Hodgkin-Katz equation:

$$\mathrm{J}^{I}_{PTP} = V^{I}_{PTP}.\mathrm{P}.\frac{[I]_m - [I]_c}{1+\exp\left(\frac{s_1-\Delta\psi}{s_2}\right)}, \tag{5.3.9}$$

where I is the considered ion, V^{I}_{PTP} is the rate constant of the flux of I through the mPTP, P the variable representing the permeability of the membrane, and s_1, s_2 are parameters representing the threshold and the slope of the dependence of the flux on the mitochondrial transmembrane potential. Using this equation, it is possible to write down the expressions of the fluxes in function of the internal and external concentration of the considered ion and the variable representing the permeability of the membrane (the variable representing the fraction of open mPTP in our case).

Even though the classical regulators of the mPTP (*e.g.* calcium, membrane potential) were taken in consideration in these literature models, the ROS component was neglected. This could be limiting especially in the pathological context in which we are interested. This is because, as discussed in the introduction (sec 1.3), the pathological opening of the mPTP is known to be related to increased ROS production by the mitochondria. Also, in the cardiac cell, ROS have a

strong impact on the excitation-contraction coupling system [43]. Thus incorporating the ROS production by mitochondria and relating it to the mPTP is crucial for a more complete model of the cardiac mitochondria that could account for both physiological and pathological contexts.

In the next chapter we will incoporate the mPTP activity and ROS generation to our previously introduced cardiac mitochondrial model (3.1.9). Following the modeling approach in the literature, we will model the mPTP activity using the evolution equation (5.3.8). Similarly, the fluxes of ions associated with the mPTP opening will be modeled using the equation (5.3.9). In what concerns the ROS, we will be only interested in modeling its production. This production will be considred as a shunt from the electron transport chain as described in [18]. Additionally, the influence of the ROS concentration on the opening of the mPTP will be considered. The details about the modeling and the considered regulators will be discussed in the next chapter.

Chapter 6

A new cardiac mitochondrial model including respiration, Ca^{2+}, mPTP and ROS

Contents

In this chapter, we extend our previously introduced cardiac mitochondrial model (3.1.9) so it can account for the mPTP activity and ROS production. Here we adopt the same mPTP modeling approach as in [69, 65, 75], which was discussed in section 5.3. However, unlike the latter models, we incorporate ROS production by the mitochondria, and add ROS as one of the mPTP activators. Overall, two new state variables (denoted P and $[O_2.^-]$) representing the mPTP porosity and the concentration of matrix ROS respectively, were added to our previous model (3.1.9).

6.1 Modeling ROS production

The ROS production was modeled as in Cortassa *et al.* [18] but with several simplifications hypothesis thar are convenient to our purpose. Unlike in [18], the model is not designed to study the influence of ROS on the oscillatory mechanism of the mitochondria. Indeed we are interested in adding the mitochondrial ROS production to eventually link it to the mPTP component of the model as one of the known regulators.

For this reason, it is not crucial for us to add explicitly a state variable representing the cytoplasmic ROS concentration, as done in Cortassa *et al.*. Besides that, ROS related mechanisms such as cytoplasmic ROS scavenging, and ROS activation of inner mitochondrial membrane were also not considered in our model for the sake of simplicity. Additionally, the efflux rate of mitochondrial ROS, via the membrane anion channels, is considered as a linear function of the ROS concentration, without explicitly modeling the functioning of these channels. However, the efflux of ROS via the mPTP when it is open is considered. This efflux rate, as well as all the rates associated with other ions transport through the mPTP, are modeled using a simplified version of the Goldman-Hodgkin-Katz equation:

$$J_{PTP}^{O_2^-} = V_{PTP}^{O_{2\cdot}^-}.P.\frac{[O_{2\cdot}^-]}{1+\exp\left(\frac{p_{30}-\Delta\psi}{p_{29}}\right)}, \tag{6.1.1}$$

where $V_{PTP}^{O_{2\cdot}^-}$, p_{29}, and p_{30} are parameters given in Table 6.1. Using the fact that the ROS in the mitochondria are created when an electron leaks from the ETC and binds to a molecule of dioxygen, the ROS production can then be modeled as a shunt (denoted s) from respiration. The evolution equation of $[O_{2\cdot}^-]$ can thus be written as follows:

$$\frac{\mathrm{d}}{\mathrm{d}t}[O_{2\cdot}^-] = \ \mathrm{s}.J_O - \alpha_{O_{2\cdot}^-}.[O_{2\cdot}^-] - J_{PTP}^{O_2^-} \tag{6.1.2}$$

where the parameters s and $\alpha_{O_{2\cdot}^-}$ are given in Table 6.1.

6.2 Modeling the mPTP activity

The considered activators of the mPTP will be the mitochondrial matrix calcium concentration $[Ca^{2+}]_m$, the mitochondrial transmembrane potential $\Delta\psi$, and the mitochondrial matrix ROS

concentration $[O_2.^-]$. As the exact mechanisms behind the ROS activation of the mPTP is not well established to our day, we choose a similar approach as in the first model. Indeed, since in biology most of the activators tend to have a threshold characteristic dependency, we choose a sigmoidal function to illustrate the dependency of the mPTP opening on the ROS through the function:

$$f([O_2.^-]) = \frac{1}{1+\exp\left(\frac{p_{31}-[O_2.^-]}{p_{32}}\right)}. \tag{6.2.1}$$

Following the formulation described in [69, 65, 75] the evolution equation of the fraction of open mPTP (denoted P) can be written as follows:

$$\frac{\mathrm{d}}{\mathrm{d}t}P = V_{op}(1-P)\frac{1}{1+\exp\left(\frac{\Delta\psi - p_{27}.[Ca^{2+}]_m}{p_{28}}\right)}.f([O_2.^-]) - k_{cl}.P, \tag{6.2.2}$$

where V_{op}, k_{cl}, p_{27}, and p_{28} are parameters given in Table 6.1. The only difference here is the addition of an explicit dependence of the ROS on the activity of the mPTP through the function $f([O_2.^-])$. Using the same previously used formulation of the Goldman-Hodgkin-Katz equation, for the ROS efflux via the mPTP, the ions transport rates via the mPTP of the different components of our model can be written as follows:

$$J^{Ca}_{PTP} = V^{Ca}_{PTP}.P.\frac{[Ca^{2+}]_m - [Ca^{2+}]_c}{1+\exp\left(\frac{p_{30}-\Delta\psi}{p_{29}}\right)}, \tag{6.2.3}$$

$$J^{H}_{PTP} = V^{H}_{PTP}.P.\frac{1}{1+\exp\left(\frac{p_{30}-\Delta\psi}{p_{29}}\right)}, \tag{6.2.4}$$

and

$$\begin{aligned} J^{ADP}_{PTP} &= V^{ADP}_{PTP}.P.\frac{[ADP]_m - [ADP]_c}{1+\exp\left(\frac{p_{30}-\Delta\psi}{p_{29}}\right)} \\ &= V^{ADP}_{PTP}.P.\frac{\frac{K_{F1}A_{tot,m}}{[Pi]_m\exp\left(\frac{F}{RT}\Delta G_{p,m}\right)+K_{F1}} - \frac{K_{F1,c}A_{tot,c}}{[Pi]_c\exp\left(\frac{F}{RT}\Delta G_{p,c}\right)+K_{F1,c}}}{1+\exp\left(\frac{p_{30}-\Delta\psi}{p_{29}}\right)}, \end{aligned} \tag{6.2.5}$$

where the parameters $V^{Ca}_{PTP}, V^{H}_{PTP}$, and V^{ADP}_{PTP} are given in Table 6.1. In equation (6.2.4), the concentration of H^+ does not appear because it is not a variable of the model. It is implicitly included in the parameter V^{H}_{PTP}, and the correspondent flux J^{H}_{PTP} will only participates in the evolution equation of the transmembrane potential. In equation (6.2.5), the transition, from the adenine nucleotide concentrations to the Gibbs free energy variables, is done using the change

of variable equations (3.1.6), and (3.1.8). In the equations (6.2.3) and (6.2.5), it is the gradient of the correspondent molecules that imposes inward or outward directions of the flux.

6.3 The new model differential equations after incorporating the mPTP and the ROS

Incorporating the mPTP and ROS mechanisms to the differential equations system (3.1.9), we get a new system of differential equations that is written as follows:

$$
\begin{cases}
\dfrac{\mathrm{d}}{\mathrm{d}t}\Delta E_{\mathrm{resp}} &= \varphi_1(\Delta E_{\mathrm{resp}})\,(J_{\mathrm{sub}} - J_{\mathrm{O}})\,, \\[2ex]
\dfrac{\mathrm{d}}{\mathrm{d}t}\Delta G_{\mathrm{p,m}} &= \varphi_2(\Delta G_{\mathrm{p,m}})\left(J_{\mathrm{F1F0}} - J_{\mathrm{ANT}} + J_{PTP}^{ADP}\right), \\[2ex]
\dfrac{\mathrm{d}}{\mathrm{d}t}\Delta G_{\mathrm{p,c}} &= \varphi_3(\Delta G_{\mathrm{p,c}})\left(\gamma(J_{\mathrm{ANT}} - J_{PTP}^{ADP}) - \dfrac{\mathrm{d}}{\mathrm{d}t}J_{\mathrm{ADP,ext}}(t)\right), \\[2ex]
C_{\mathrm{m}}\dfrac{\mathrm{d}}{\mathrm{d}t}\Delta\psi &= 12J_{\mathrm{O}} - 3J_{\mathrm{F1F0}} - J_{\mathrm{ANT}} - J_{\mathrm{leak}} - 2J_{\mathrm{uni}} + 2J_{PTP}^{Ca} - J_{PTP}^{H} - J_{PTP}^{O_2^{\cdot-}}, \\[2ex]
\dfrac{\mathrm{d}}{\mathrm{d}t}[\mathrm{Ca}^{2+}]_{\mathrm{m}} &= f_m(J_{\mathrm{uni}} - J_{\mathrm{NaCa}} - J_{PTP}^{Ca}), \\[2ex]
\dfrac{\mathrm{d}}{\mathrm{d}t}[\mathrm{Ca}^{2+}]_{\mathrm{c}} &= f_c\tilde{\gamma}(J_{\mathrm{NaCa}} - J_{\mathrm{uni}} + J_{PTP}^{Ca}) + \dfrac{\mathrm{d}}{\mathrm{d}t}[\mathrm{Ca}^{2+}]_{\mathrm{ext}}(t), \\[2ex]
\dfrac{\mathrm{d}}{\mathrm{d}t}P &= V_{op}(1-P)\dfrac{1}{1+\exp\left(\frac{\Delta\psi - p_{27}.[\mathrm{Ca}^{2+}]_{\mathrm{m}}}{p_{28}}\right)}.f([\mathrm{O}_2.^-]) - k_{cl}.P, \\[2ex]
\dfrac{\mathrm{d}}{\mathrm{d}t}[\mathrm{O}_2.^-] &= \mathrm{s}.J_{\mathrm{O}} - \alpha_{\mathrm{O}_2.^-}.[\mathrm{O}_2.^-] - J_{PTP}^{O_2^{\cdot-}}
\end{cases}
\tag{6.3.1}
$$

In equation (6.3.1), the fluxes of ions via the mPTP are denoted J_{PTP}^{I}, where I is the considred ion. The expressions that are highlighted in blue are the ones that were not present in the old system of equation (3.1.9). They correspond to the newly added components (mPTP and ROS) and their associated fluxes. The fluxes expressions J_{PTP}^{Ca} and J_{PTP}^{H} were adopted from Wac-

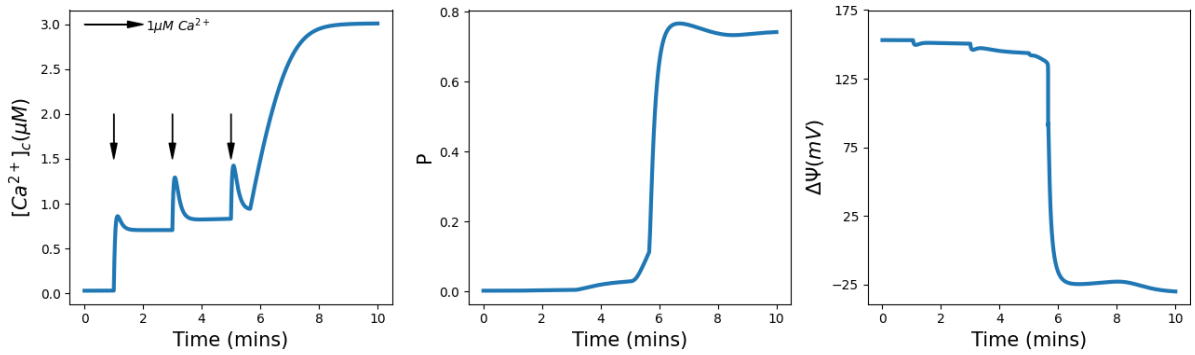

Figure 6.1: Model simulation of successive calcium additions leading to definitive mPTP opening. More details are explained in the text.

quier *et al.* model [75]. The other mPTP related fluxes expressions J_{PTP}^{ADP} and $J_{PTP}^{O_2^-}$ were newly added and they were modeled using the same approach (see equation (5.3.9)). The equation of the evolution of P was also inspired from [69, 65, 75] , with the addition of the dependance of the mPTP opening on ROS. The equation of the evolution of ROS concentration $[O_2.^-]$ is a new addition, in which the ROS production part (s.J_O) was adopted from Cortassa *et al.* model [18].

6.4 Behavior of the model in the presence of successive Ca^{2+}additions

In Fig. 6.1, we run a simulation of our model that shows the influence of cytoplasmic calcium additons (1 μM of cytoplasmic calcium for each arrow) on the output of our model. When small quantities of cytoplasmic calcium quantities are added (first two arrows), they enter the mitochondria via the Ca^{2+}-uniporter leading to a small depolarization in the mitochondrial membrane potential, and almost no effect on the porosity of the mPTP. However at a certain threshold of added calcium (third arrow), the mitochondria are unable to sequester it all, and we observe a brutal collapse of the mitochondrial transmembrane potential accompanied with a high porosity of the mPTP and a relargation of the matrix calcium. Some of these observations can be seen qualitatevly in experiments (Fig. 6.2, [78]). More practically, in the model, calcium influences the threshold at which the membrane potential inhibits the high conductance opening of the

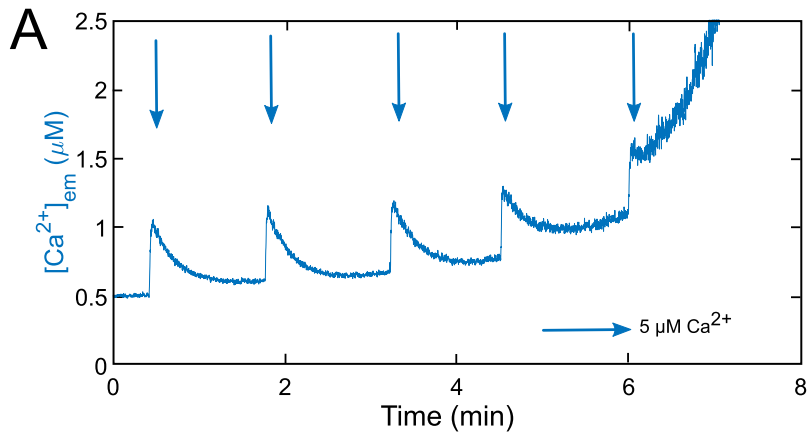

Figure 6.2: Successive calcium additions leading to mPTP definitive opening and subsequently to the sudden rise in the cytoplasmic calcium concentration. Data correspond to experiments on rat hepatocytes from [75].

mPTP. This is modeled through the function $1 + \exp\left(\frac{\Delta\psi - p_{27}.[Ca^{2+}]_m}{p_{28}}\right)$ that multiplies the rate constant of the mPTP opening V_{op} in the evolution equation of P in the system (6.3.1). When this threshold is attained, the protons efflux via the mPTP (flux eq. 6.2.4), even with small opening magnitude, leads to more depolarization of the mitochondrial membrane potential, which leads in its turn to more mPTP opening and more protons ejection. This cycle is what makes the high conductance opening mode of the mPTP irreversible. On the other hand, when the mitochondrial membrane potential decreases, the magnitude of the respiration rate increases, hence we have an increase in ROS production which leads also to faster rate of mPTP opening.

In low conductance mode, the value of cytoplasmic calcium, over which the mitochondria starts sequestering calcium (first arrow of the left subfigure of Fig. 6.1), is controlled by the balance between the Ca^{2+}-uniporter and the Ca^{2+}/Na^{+}exchanger.

6.5 Experimental observed mPTP opening types

In an experimental study [16], our collaborators characterized the different opening types of the mPTP, using calcium additions as a triggering factor for both transient and definitive openings. The study is based on monitoring individual mitochondria using fluorescent dye tetramethyl-

rhodamine methyl ester (TMRM) microscopy in the presence of calcium. Indeed the variation of the intensity of fluorescence can be seen as an analogy of the variation of the mitochondrial transmembrane potential $\Delta\psi$, and hence is a good indication of the mPTP openings.

More practically, their experiment starts by sacrificing a rat, then isolating its cardiac mitochondria (in the order of several hundreds or few thousands). The mitochondria are diluted to a concentration of 0.1 mgprot mL^{-1} in a buffer containing the substrates glutamate-malate and succinate. Calcium in the form of $CaCl_2$ at a concentration of 1 mM is added to the mitochondrial solution. It is important to note that the medium already contains 1 mM EGTA (chelating agent known for its ability to bind to calcium), so the final calcium concentration (free calcium) is therefore much lower, of the order of a few μM.

The mitochondria are then put on a coverslip, and are observed using a inverted microscope in transmitted light and fluorescence (Fig. 6.3 A). Microscopy images are taken all along the experimental time span. These images are then analyzed using an adequate computer software 'ImageJ-Trackmate' that permits to follow the intensity of fluorescence of the mitochondria simultaneously in function of time. Indeed, this software works in two main steps, a first step consisting of detecting the objects (mitochondria) on each of the images and a second step allowing the identification of the same object over time. The output results of the software are time series of fluorescence intensities for each of the individual mitochondria.

Overall, their method allows to visualize the different possible depolarizations, of the mitochondrion membrane potential, observed when the mPTP exhibits a transient or definitive opening. Indeed, to characterize the different depolarizations observed, they analyzed the TMRM monitoring curves of several thousand mitochondrion in the presence of calcium, in an attempt to create a statistical classification.

In these experiments, they found four main types of events classified from 0 to 3 and illustrated in the examples in Fig. 6.4. The goal of this figure is not to compare amplitudes or time intervals but only to show curves representative of the different types observed and their shapes. The first type of event is named type-1, which is shown schematically in the left plot of Fig. 6.4. It corresponds to a transient depolarization, visible by a decrease in the fluorescence of the TMRM, and a peak shape. An important point is that the intensity of fluorescence, after

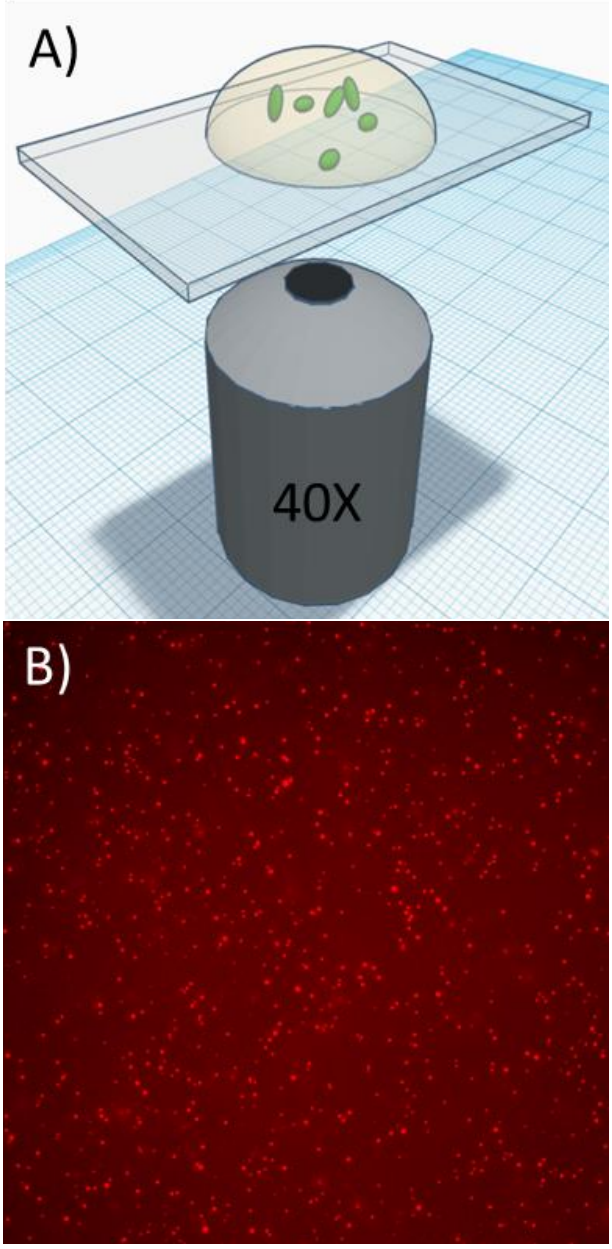

Figure 6.3: A) Schematic of the microscopy experiment for monitoring individual mitochondria. B) Example of an image obtained by microscopy: each point on the image corresponds to an isolated mitochondria. Figure taken from [16].

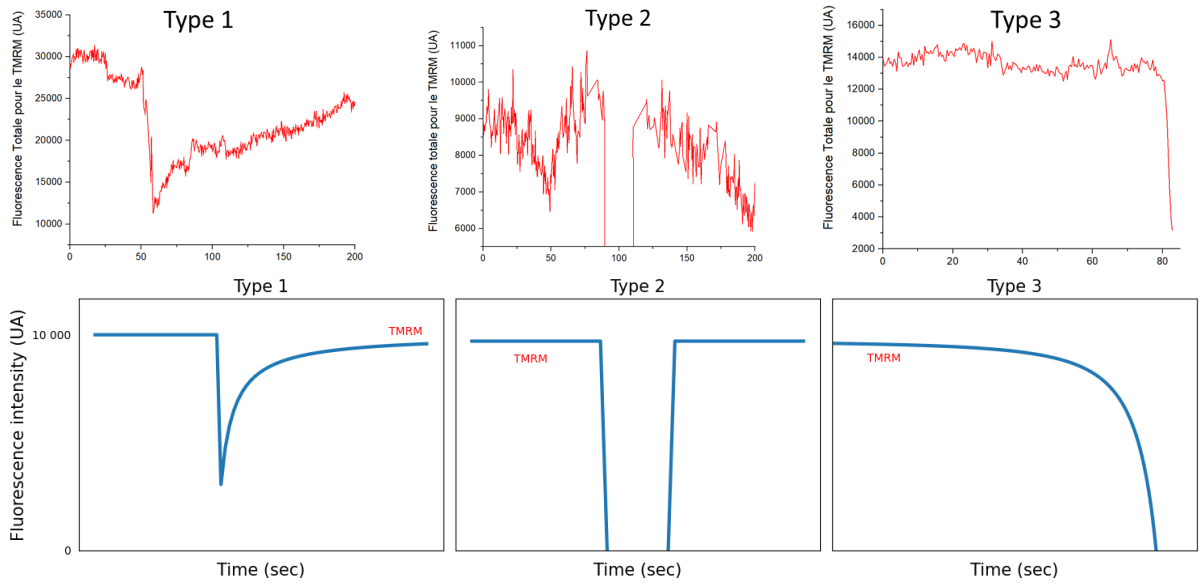

Figure 6.4: Illustration of the shapes of the different classes of TMRM curves obtained experimentally. Type-0 is not illustrated as it does not show any variation in its TMRM curve. More details in the text.

the peak, does not necessarily go back to the exact same magnitude as before the peak, yet it tends to be not far away from it. Type-2 also corresponds to a transient depolarization (middle plot of Fig. 6.4), but in this case at the time of depolarization the mitochondrion will not be detectable anymore. Another difference with type-1 is the time necessary for repolarization. For type-1, this step will be fast but it is possible to follow the gradual rise in fluorescence while for type-2, this rise is very often almost instantaneous. The third type of event, type-3, is the one that corresponds to a definitive depolarization (right plot of Fig. 6.4), where the fluorescence in TMRM will decrease drastically and then never go up again. It is a total loss of activity or the equivalent of the mitochondrial death. The last type of event, named type-0, which is not shown in Fig. 6.4, is the simplest. It corresponds to a mitochondrion which does not present any transient depolarization when monitoring its TMRM. We think that this type is actually a type-1, but with a very weak depolarization that could not be detected either when monitoring the TMRM or while numerically classifying the different types.

In conclusion to their experiments, our collaborators performed statistical counting of the four different events occurring on several thousands of mitochondria ($N = 2737$). The results

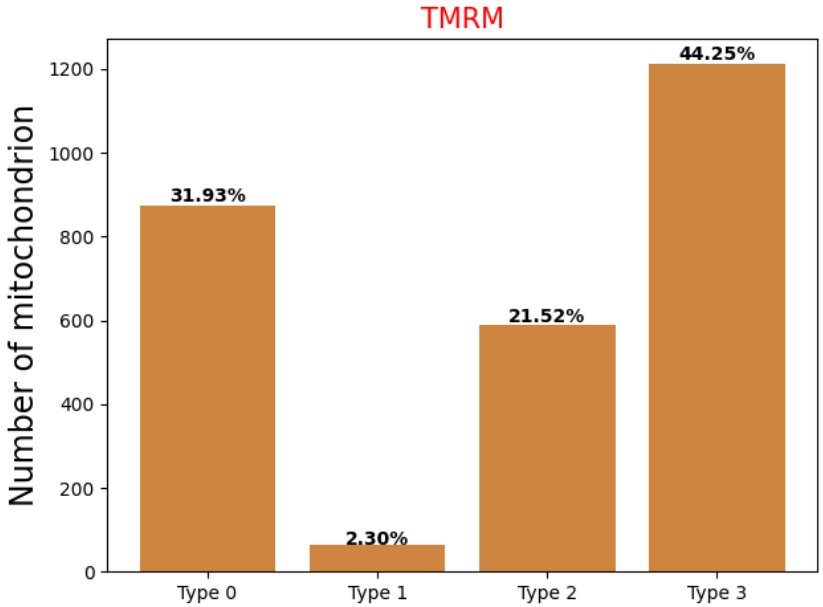

Figure 6.5: Cumulative histogram of the number of mitochondrion that underwent one of the different types of depolarizations detected with the TMRM, with the substrate condition and immediately after injection of 1 mM calcium.

is presented in the Fig. 6.5. In the next chapter we will see how to make the link between these data and our model. In particular, we will use these experimental statistical counting to perform inference on some of our model parameters.

Table 6.1: Parameters associated with the mPTP and ROS mechanisms. (*): These parameters can not be found directly in the literature and their values are proposed either by analogy to other parameters associated to similar fluxes or after observing a set of model simulations.

Parameter	Description	Value	Unit	Reference
V_{op}	mPTP opening rate constant	4.2	min^{-1}	[75]
k_{cl}	mPTP closure rate constant	1.2	min^{-1}	[75]
p_{27}	Voltage and calcium dependence of mPTP opening	15 000	$\text{mV nmol}^{-1}\text{ mgprot}^{-1}$	[75]
p_{28}	Voltage dependence of mPTP opening	20	mV	[75]
p_{29}	Voltage dependence of ion fluxes via mPTP	50	mV	[75]
p_{30}	Voltage dependence of ion fluxes via mPTP	100	mV	[75]
p_{31}	Parameter for the dependence of mPTP opening on $O_2.^-$	0.08	nmol mgprot^{-1}	(*)
p_{32}	Parameter for the dependence of mPTP opening on $O_2.^-$	0.008	nmol mgprot^{-1}	(*)
V_{PTP}^{Ca}	Rate constant of the Ca^{2+} flux via the mPTP	2.4	$\text{nmol mgprot}^{-1}\text{ min}^{-1}$	[75]
V_{PTP}^{H}	Rate constant of the H^+ flux via the mPTP	2160	$\text{nmol mgprot}^{-1}\text{ min}^{-1}$	[75]
V_{PTP}^{ADP}	Rate constant of the ADP flux via the mPTP	2.4	$\text{nmol mgprot}^{-1}\text{ min}^{-1}$	(*)
$V_{PTP}^{O_2.^-}$	Rate constant of the $O_2.^-$ flux via the mPTP	2.4	$\text{nmol mgprot}^{-1}\text{ min}^{-1}$	(*)
s	Electron shunt from the ETC	0.05	dimensionless	[18]
$\alpha_{O_2.^-}$	Parameter for the $O_2.^-$ efflux via the membrane anion channels	0.5	min^{-1}	(*)

Chapter 7

Classification and parameters inference

Contents

7.1 How to define mPTP opening classes of the model

The link between the experimental data, introduced in sec. 6.5, and our model is not trivial. Indeed, the experimental data focus on the mPTP opening type as a result of Ca^{2+}addition, through monitoring the intensity of TMRM, which can be seen as monitoring the mitochondrial membrane potential. To make a link between these data and our model, the state variables that should mostly interest us are the fraction of open mPTP (P), and the transmembrane potential difference ($\Delta\psi$). Together, these two variables could give an indication on the state of the mPTP, since the mPTP openings are associated with a depolarization of the mitochondrial membrane

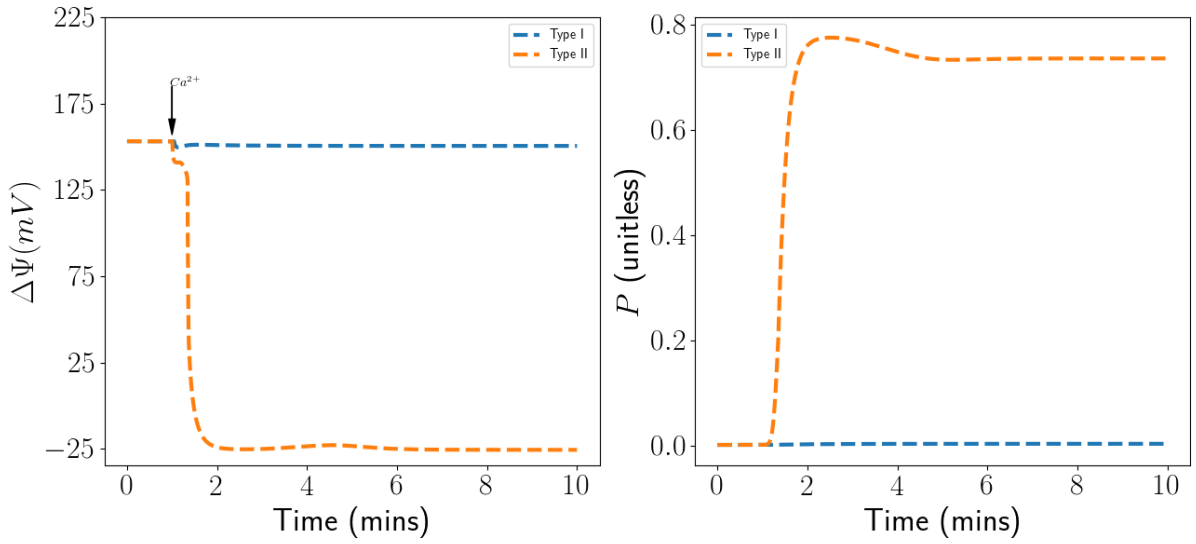

Figure 7.1: Example of two model simulations illustrating the two possible classes, of simulated mPTP opening states, after Ca^{2+}addition.

potential. After performing a first set of model simulations, with different conditions (varying the model parameters, as well as the quantity of Ca^{2+}added), we remarked that the output ($\Delta\psi$ and P) could be grouped in two classes that will be denoted with the roman numeral type-I and type-II (illustrated by an example in Fig. 7.1). They should not be confused with the previously discussed experimental mPTP opening types that were denoted using the classical numerals (type-0,type-1,type-2 and type-3). The link between the experimental mPTP opening types (denoted using roman numerals) and the model mPTP opening types (denoted with the classical numbers) will be explained in this section in the text, as well as in the next section 7.2.

The first class (type-I) is when the membrane potential undergoes a small transient depolarization, following the Ca^{2+} addition, then repolarize and attain a value not far from its original magnitude. In this class of events, the magnitude of the porosity of the mPTP tends to be very minimal and barely changes following the Ca^{2+} addition. In Fig. 7.1, this class of events corresponds to the plots in blue. It is clear that this class of simulations could be attributed to the type-1 transient mPTP opening of the experimental data previously discussed (sec. 6.5). On the other hand, the second class (type-II) is when the mitochondrial membrane potential collapses, and the mPTP porosity magnitude increases to high levels. This class of events is illustrated in,

Fig. 7.1, by the plots in orange. This class of simulations could be associated with the type-3 definitive mPTP opening of the experimental data.

The model we developed is not designed initially to help classification of mPTP opening types. Hence, to make a link between the experimental data, introduced in sec. 6.5, and our model simulations, we build a classifier that takes as input the initial conditions and a set of the model parameters, and as an output returns an mPTP opening type. That means, when we run a simulation, the solution of the dynamical system (6.3.1) has to be classified as one of the two possible simulated types (type-I or type-II). Indeed, the resulting type could be identified using the solution curves of the state variables $\Delta\psi$ and P. The classification is done in two steps. First we solve the differential equation system (6.3.1) for a set of model parameters and initial conditions. Second, using the solution curves of $\Delta\psi$ and P, the classifier choose the output class in the following way:

Algorithm 1 Automated classifier, of the solution of eq. (6.3.1), into mPTP opening types (type-I and type-II).

$t_0 \leftarrow$ first time instant
$t_f \leftarrow$ final time instant
$t_{Ca} \leftarrow$ time instant at which $Ca^{2+}$is added
if |mean($\Delta\psi[t_0 : t_{Ca}]$) - $\Delta\psi[t_f]$| $\geq$ (r $\times$ $\Delta\psi[t_0]$) & |mean($P[t_0 : t_{Ca}]$)-$P[t_f]$| $\geq$ 0.5 **then**
    Class $\leftarrow$ II
else
    Class $\leftarrow$ I
end if

The coefficient r is the approximation of the experimental relative rate of depolarization of the transmembrane potential for type-1 openings ($r \sim 0.3$). Whereas, the absolute value 0.5 guarantees that the porosity of the mPTP has increased significantly. Together these two conditions suggest that the mPTP is undergoing a definitive opening (type-II). However, if after the Ca^{2+}addition, these conditions are not fulfilled, then the membrane potential must have underwent a weak transient depolarization leading to the so called type-I mPTP transient opening state.

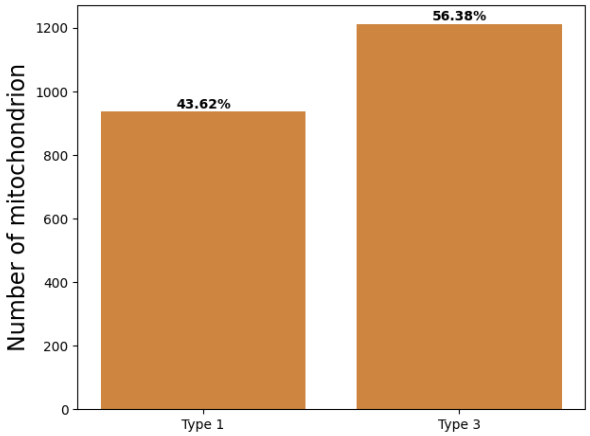

Figure 7.2: Cumulative histogram of the number of mitochondrion that underwent type-1 and type-3 depolarizations, after adopting the two data wrangling considerations evoked in section 7.2.

7.2 Data wrangling

Until this point, we have seen the experimental data on the possible mPTP opening types (ranging from type-0 to type-3), and we have explained how we built a classifier that returns two possible simulated mPTP opening type (type-I and type-II). However to make use of the experimental data in hand, they must be comparable to model simulations (classifier simulations), which is not initially fulfilled since we have different number of possible outcomes. To overcome this problem, we make two considerations for the experimental data. First we adopt the hypothesis evoked in section 6.5, which supposes that the type-0 is a sub-type-1 with a very weak depolarization of the membrane potential that made it undetectable. On the other hand, since type-2 transient depolarization behavior can not be seen in the model simulations, and in addition it is not fully understood by the experimenters, we decided to eliminate this class from the experimental data. These two considerations leave us with a new binomial distribution (Fig. 7.2) for the experimental data that is now comparable to the classifier simulations.

7.3 Parameter inference

Using the experimental data introduced in the previous section, we want to perform parameter inference so that our model is calibrated to the experimental data. However, it is clear that there is an important variability between individual mitochondria (Fig. 7.2). That means that the same experimental conditions can lead to different mPTP opening type between different individuals. This variability is an indication that point estimates of the model parameters is not appropriate. A better approach would be to consider the parameters in question as random variables, and to compute their actual distributions.

7.3.1 Preliminary sensitivity analysis

Overall, with the new parameters added for the mPTP and ROS mechanisms, the complete model has forty-five parameters. Of course, not all of them are identifiable with respect to the data in hand. Then again, we perform a global sensitivity analysis, using Sobol indices, to quantify the influence of the model parameters on the type of simulated mPTP opening as done previously (sec. 4.4). The parameters of the model were picked from a uniform distribution varying 100% around their values listed in Tables 3.5, 4.1, and 6.1.

The concentration of Ca^{2+}addition is of course the main influencer on the resulting simulated mPTP opening type. However, this concentration is not a model parameter, and it was set to 20 μM, when performing the sensitivity analysis. This value was chosen taking into account two considerations. The first is the setup in which the experimental data were measured. That means to consider the amount of experimental Ca^{2+}concentration added. The second consideration is related to having variability in term of the two resulting simulated mPTP opening types (type-I and type-II). With this setup, and after evaluating the model using a parameters sample of 47000, we get 65.26% of type-I and 34.74% of type-II.

The results of the sensitivity analysis are presented in Fig. 7.3. Only parameters with dominant influence will be considered for inference in the next sections. We set a minimum total Sobol index of 0.15 over which parameters are considered to have enough influence on the simulated mPTP opening type. Using this criteria, it is the set of eleven parameters

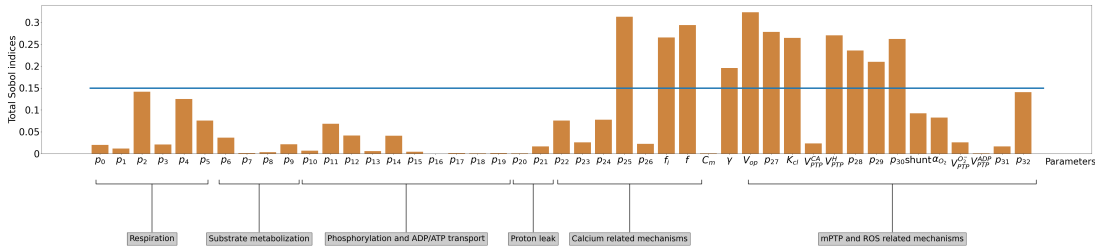

Figure 7.3: Total Sobol index representing the sensitivity of the simulated mPTP opening type (type-I or type-II) with respect to the model parameters. The blue line represents the threshold afterwhich we consider the total Sobol index to be important. The conditions used to compute these indices are of one addition of Ca^{2+}at a concentration of 20 μM.

$\{p_{25}, f, f_i, \gamma, V_{op}, p_{27}, k_{cl}, V^H_{PTP}, p_{28}, p_{29}, p_{30}\}$ that will be concerned. The rest of parameters will be fixed either to their previously calibrated values from Table. 4.1, or to their values from Tables. 3.5 and 6.1.

7.3.2 Meta models using machine learning

The algorithms used for parameters inference usually requires a huge number of model evaluations before reaching convergence. Sometimes this number is of the order of several dozens of millions. Note that in our case a model evaluation is equivalent to solving the equation (6.3.1) and then classifying the solution using the previously introduced classifier (sec. 7.1). Since a model evaluation takes approximately 120 seconds, it becomes important to find an alternative to classical model evaluations.

In this section, we test supervised classification algorithms to construct meta models that are able to mimic a model evaluation without going through the burden of solving the differential equations system on the experimental time interval. Indeed, in our case, these classification methods take as input a set of model parameters (in our case the eleven influential parameters that were chosen following the sensitivity analysis discussed in section 7.3.1) and return as output the correspondent simulated mPTP opening class (type-I or type-II).

Using the Python package scikit-learn [62], we compare the performance of four supervised classification methods (decision tree, gaussien naive Bayes, support vector machine, and

k-nearest neighbor). The features of the constructed classification models are the eleven parameters previously selected following the sensitivity analysis (sec. 7.3.1). To learn and test our models, we use for these parameters a sample of size 26000, and we compute its associated model evaluations (correspondent simulated mPTP opening classes). Even though the sample size is considered sufficient relatively to the eleven features, it is not perfectly balanced since 61.95% of it results in type-I class and the other 38.04% results in type-II class. This can lead to biased training of the classification model or to misleading performance accuracy. To overcome this problem, we use stratified train-test split. That means we split the data set into train and test sets in a way that preserves the same proportions of examples in each class as observed in the original data set. The data set proportions used in our models are 70% for training and 30% for testing.

Gaussian Naive Bayes

The Gaussian naive Bayes algorithm uses the Bayes theorem to classify the data with respect to the output classes. Indeed, this algorithm supposes that the features are distributed according to a normal distribution. Using the training data, the parameters of the gaussian likelihood function (the mean and the standard deviation) are estimated for each output class. Then, for each new input feature, the probability of the feature being associated to each class is calculated using the Bayes theorem. The classification is then done by choosing the class that had the higher probability (Fig. 7.4). In addition, this algorithm makes the assumption that the features are strongly independent.

Support vector machines (SVM)

The support vector machines algorithms are based on maximizing the margin between the different classes of data. The margin is the distance between the separation boundary and the closest samples. These are called support vectors. In SVM, the separation boundary is chosen as the one that maximizes the margin. The challenge is to find this optimal dividing border, from a training set. This is done by formulating the problem as an optimization problem. In the case

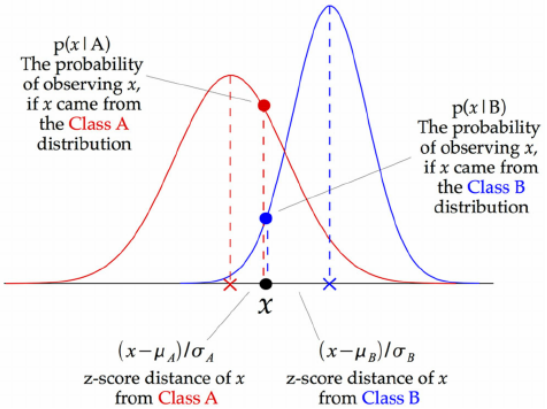

Figure 7.4: Illustration of how the Guassian naive Bayes algorithm works. More details in the text. Taken from https://iq.opengenus.org/gaussian-naive-bayes/ .

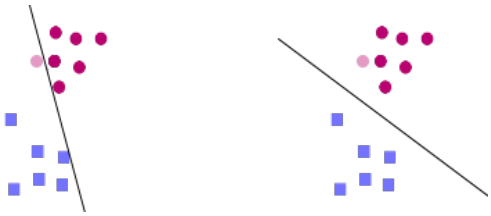

Figure 7.5: Illustration of linearly separable data. The separation boundary in the left figure is not the optimal one, as the one on right figure maximizes more the margin.

where the data are linearly separable, the task is simple (Fig. 7.5). On the other hand, when data are not linearly separable, the trick is to transform the representation space of the input data into a space of greater dimension (possibly of infinite dimension), in which it is probable to have a linear separation (Fig. 7.6). This could be done using a kernel function, which must respect the conditions of Mercer's theorem, and which has the advantage of not requiring the explicit knowledge of the transformation to be applied for the change of space.

Decision tree

A decision tree is a decision support tool representing a set of choices in the graphic form of a tree. The various possible decisions are located at the ends of the branches (the "leaves" of the tree), and are reached according to decisions taken at each stage. Decision trees can be calculated automatically from databases by supervised learning algorithms. These algorithms automatically select discriminant variables from unstructured and potentially large data. They

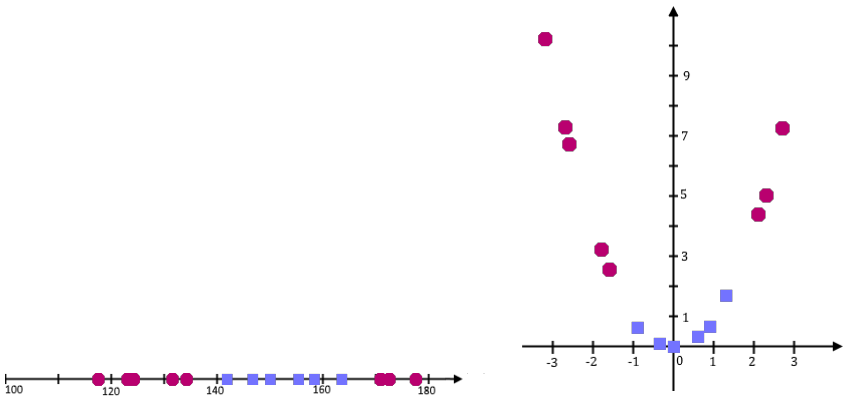

Figure 7.6: To the left: 1D data that are not linearly separable in $\mathbb{R}$. To the right: the same data becomes linearly separable in $\mathbb{R}^2$ after performing the transformation $\phi : x \longmapsto \left(\frac{x-150}{10}, \left(\frac{x-150}{10}\right)^2\right)$.

can thus make it possible to extract logical cause-and-effect rules that did not initially appear in the raw data. The rules of transition are generally based on information theory. This means that the splitting rules at each node are created based on either maximizing the information gain, or reducing the entropy. The algorithm used for the generation of our results (in particular for Fig. 7.7) uses entropy as splitting rule.

K-nearest neighboor (KNN)

The k-nearest neighbors is a non parametric method in which the model stores the observations of the training set for the classification of the data of the test set. Indeed, this algorithm is qualified as lazy (Lazy Learning) because it does not learn anything during the training phase. To predict the class of a new input data, it will look for its k nearest neighbors (using Euclidean distance, or others) and choose the class of majority neighbors. Practically, the different steps needed to apply this algorithm are the following:

- we fix the number of neighbors k,
- we detect the k-neighbors closest to the new input data we want to classify,
- the corresponding classes are assigned by the majority of votes.

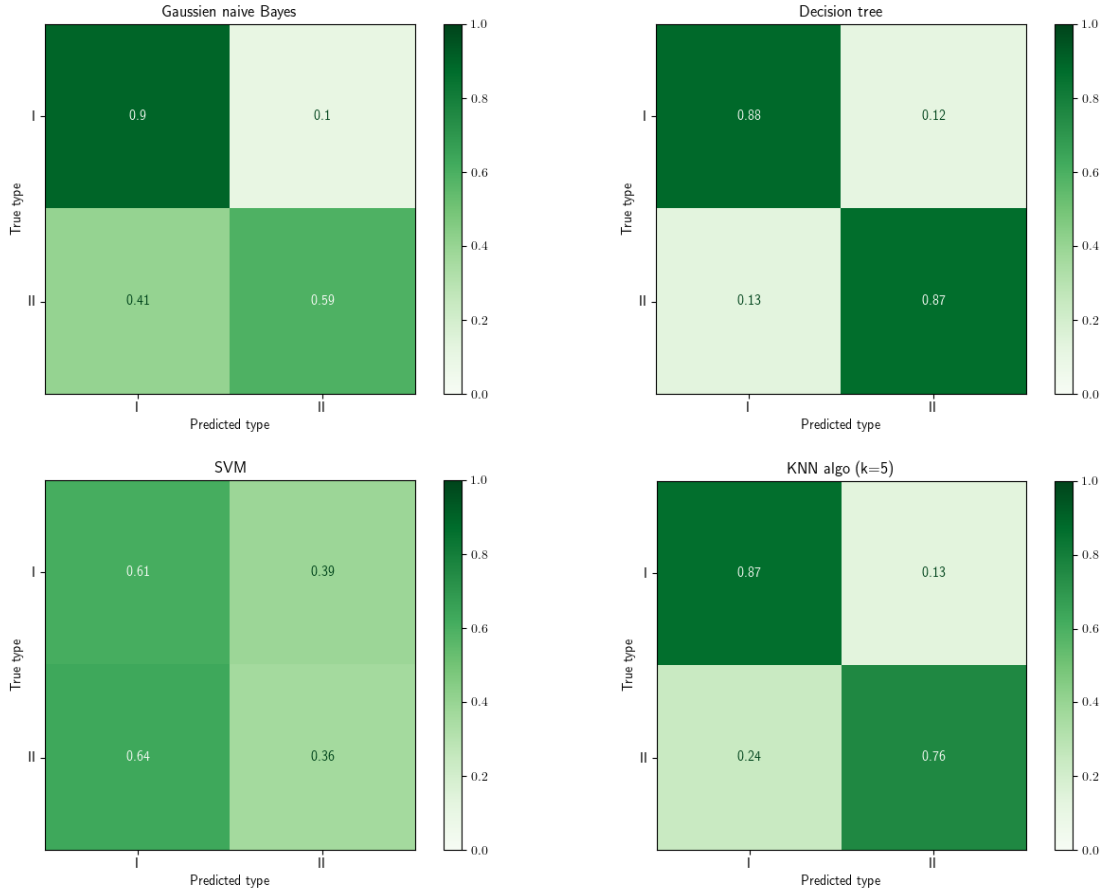

Figure 7.7: Confusion matrices that show the performance of the four supervised classification algorithms tested. The matrices are normalized with respect to the true values (rows). More details in the text.

The optimal k is chosen in a way to minimize the error rate. In our case, we tried to run the algorithm for different values of k (from one to fifteen), and the k value that gave the better performance was selected ($k = 5$ in our case).

Classification results

Fig. 7.7 shows the performance of the four tested methods. These confusion matrices are constructed by comparing the true class (type-1 and type-3) and the predicted class (type-I and type-II) of the test data set. The diagonals of the matrices show the capability of the algorithm to predict true classifications (true positives and true negatives). In the context of our model,

this means the ability of the algorithm to predict type-I when the true experimental class is type-1 and type-II when the true experimental class is type-3. On the other hand, the off-diagonals show the false predictions of the algorithms. That means the events where the algorithm predicts a type-I when the true experimental class is type-3, or a type-II when the true experimental class is type-1. We choose to normalize these matrices with respect to the true classes (with respect to rows), for easier reading. The tuning parameters for each algorithm, if they exist, were chosen in a way as to return the best performance possible for the correspondent method.

Many performance indices could be calculated using the data from these matrices. However in our case, it is clear which algorithm performs the best. This could be figured out from the confusion matrix that has the highest values on the diagonal and the lowest values on the off-diagonal, which corresponds to the decision tree algorithm in our case. Using this method, we are able, in approximately 0.3 ms and with an accuracy of 84.2%, to mimic a model evaluation. We should note that the accuracy is calculated as the true predictions over the total number of predictions.

7.3.3 Inference for parameter estimation

Now that all is setup, we explain how we performed parameters inference using the experimental data (sec. 7.2). The aim is to compute the distribution of the eleven influential parameters $\theta := \{p_{25}, f, f_i, \gamma, V_{op}, p_{27}, k_{cl}, V^H_{PTP}, p_{28}, p_{29}, p_{30}\}$, that best reproduces the experimental data.

Indeed, since the parameters in question are treated as random variables, we first tried to apply Bayesian inference algorithm. However, this did not work out because of several problems that we will discuss in the next paragraph.

Bayesian inference is based on Bayes theorem:

$$\overbrace{f(\theta/\text{Data})}^{\text{Posterior}} = \frac{\overbrace{p(\text{Data}/\theta)}^{\text{likelihood}} \times \overbrace{f(\theta)}^{Prior}}{p(\text{Data})}, \tag{7.3.1}$$

where θ is the continuous set of eleven parameters in question, $f(\theta)$ is the probability density function, $p(\text{Data}/\theta)$ is the likelihood of the data given hypothesis θ, and $p(\text{Data})$ is the total probability of data. Indeed, the idea is to compute the posterior or the updated distribution of

the parameters in question using some prior knowledge on these parameters (via $f(\theta)$), and a likelihood with respect to experimental data (via $p(\text{Data}/\theta)$).

The posterior distribution is then computed numerically using, for example, the following Metropolis Hasting algorithm:

Algorithm 2 Metropolis Hasting algorithm to sample from the posterior distribution of the parameters θ.

At $i = 0$ draw θ_0 from the prior
θ_{i+1} is generated as follows:

1. Sample a candidate θ_{cand} from a jump distribution (e.g $\mathcal{N}(\theta_i, COV)$)
2. Compute $r(\theta_i, \theta_{\text{cand}}) = \frac{p(\text{Data}/\theta_{\text{cand}})f(\theta_{\text{cand}})}{p(\text{Data}/\theta_i)f(\theta_i)}$
3. Sample a value of θ_{i+1} according to:

$$\theta_{i+1} = \begin{cases} \theta_{\text{cand}} & \text{with probability } \min(R, 1) \\ \theta_i & \text{Otherwise} \end{cases}$$

4. Increment i and return to step 1

To use the above algorithm we first need to define our likelihood function. Since the model can only return two possible outcomes (type-I or type-II), the likelihood function should correspond to a binomial distribution. Hence the likelihood function is written as follows :

$$\mathcal{L} = \binom{N}{k} p^k (1-p)^{N-k}, \tag{7.3.2}$$

where p is the probability of having a type-I mPTP opening, $N = 2148$ is the total number individual mitochondrion from the experimental data, $k = 937$ is the number of events with a type-1 output among the N trials. However, working with this likelihood function can give rise to numerical problems such as underflows. The classical approach to overcome this is the use of the log likelihood function instead :

$$\ell = \log \binom{N}{k} + k \log p + (N-k) \log (1-p). \tag{7.3.3}$$

The first problem is that our model is deterministic, meaning that, for every set of parameters θ, the output is either a type-I or type-II. This leads to a likelihood equal to zero (since either p or $(1-p)$ is necessarily equal to 0). Thus the previous algorithm could not work properly.

To overcome this we first tried to add a measurement error ϵ to our model so it becomes a probabilistic model. However, this did not work as well because the algorithm was trying to calibrate the error component ϵ of the model, leaving the parameters θ unadjusted.

For those reasons, we had to use an algorithm that takes into account the fact that the model is deterministic. Indeed, we used a revisited version of the algorithm 2. The idea was to draw, at each iteration, a collection of θ samples instead of just a single draw. The parameter p could be then estimated using the latter samples of θ of the eleven parameters in question, and their associated model evaluations. Since, in this version of the algorithm, we are drawing at each iteration a collection of θ samples, we eliminate from the ratio $r(\theta_t, \theta_{\text{cad}})$ the density functions because they become irrelevant.

Indeed the new version becomes an iterative maximum likelihood algorithms as follows:

Algorithm 3 Iterative maximum likelihood algorithm for computing the distribution of θ.

$M \leftarrow 300$ ▷ Sample size of the distribution of θ.
it_max $\leftarrow 500,000$ ▷ Maximum number of iterations
$\theta_0 \sim \mathcal{U}(0, 2\hat{\theta})$ ▷ Initial guess of the distribution of θ.
▷ $\hat{\theta}$ is the prior value (100% variation).

$i \leftarrow 1$
while i < it_max & $|\ell(\theta_{i-1}) - \ell_{\text{opt}}| > \epsilon$ **do**
    $\theta_{\text{cand}} \sim \mathcal{N}(\theta_i, s\mathbb{I}_{11})$ ▷ Random walk around θ_i using a multivariate normal distribution.
    ▷ s is the jump strength.
    if $\ell(\theta_i) \geq \ell(\theta_{i-1})$ **then**
        Accept θ_i
    else
        Keep θ_{i-1}
    end if
end while

First, an initial guess θ_0 of the distribution of θ is proposed. This guess is sampled from a uniform distribution varying 100% around the parameters prior values (Tables. 6.1 and 3.5). Each θ_i can be seen as a matrix with M rows and 11 columns, where the columns represent the parameters in question and the rows represent the sample size. Next, at each iteration i of the algorithm, a new candidate distribution is proposed using a random walk around the previous distribution guess. We use a multivariate normal distrubution for this random walk.

The strength of the jump s is tuned so that the acceptance rate of the algorithm stays near 0.23 as recommended in [27]. The stop criteria depends on how far the current log-likelihood value is from the optimal one, ℓ_{opt}, which is calculated using the experimental data from section 7.2. At the end, after $\sim 200,000$ iterations, we obtain the desired distribution θ (Fig. 7.8).

7.4 Discussion

In this second part of the manuscript, we incorporated the mPTP to the previously discussed cardiac mitochondrial model. Even though not all of its known regulators are considered in our model, the most known ones (membrane potential, calcium and ROS) are taken into account. One of the advantages of this model, over other literature models, is that the rate of opening of the mPTP includes a direct explicit dependance on ROS concentration. This is important since ROS is known to sensitize the mPTP to calcium [11].

The objective on the short term was to construct a mathematical model that can represent experimental observations of individual and/or population of cardiac mitochondria. This could be done by calibrating the model parameters to experimental data acquired from the latter observations. However, in contrast with the first part of the manuscript where the data used for calibration were from a population of cardiac mitochondria, here the experimental data related to the mPTP opening were acquired from individual mitochondria. This can also be seen from the high variability, between each mitochondrion, present in the data (Fig. 7.2). This variability led us to treat the model parameters in question as random variables and thus to try to compute distributions of these parameters instead of point estimates.

First, to make a link between the experimental observations (mPTP opening types) and the model simulations, we constructed a classifier that takes as input the solution of the ODE system (6.3.1) and returns as output the associated mPTP opening type. Following the same methodology as in the first part of the manuscript, and using the latter classifier, we performed sensitivity analysis for the parameters of the model. This analysis shows that only eleven parameters have strong influence on the considered output of the model which is the mPTP opening type. Unsurprisingly, all of these eleven parameters could be associated to mechanisms related

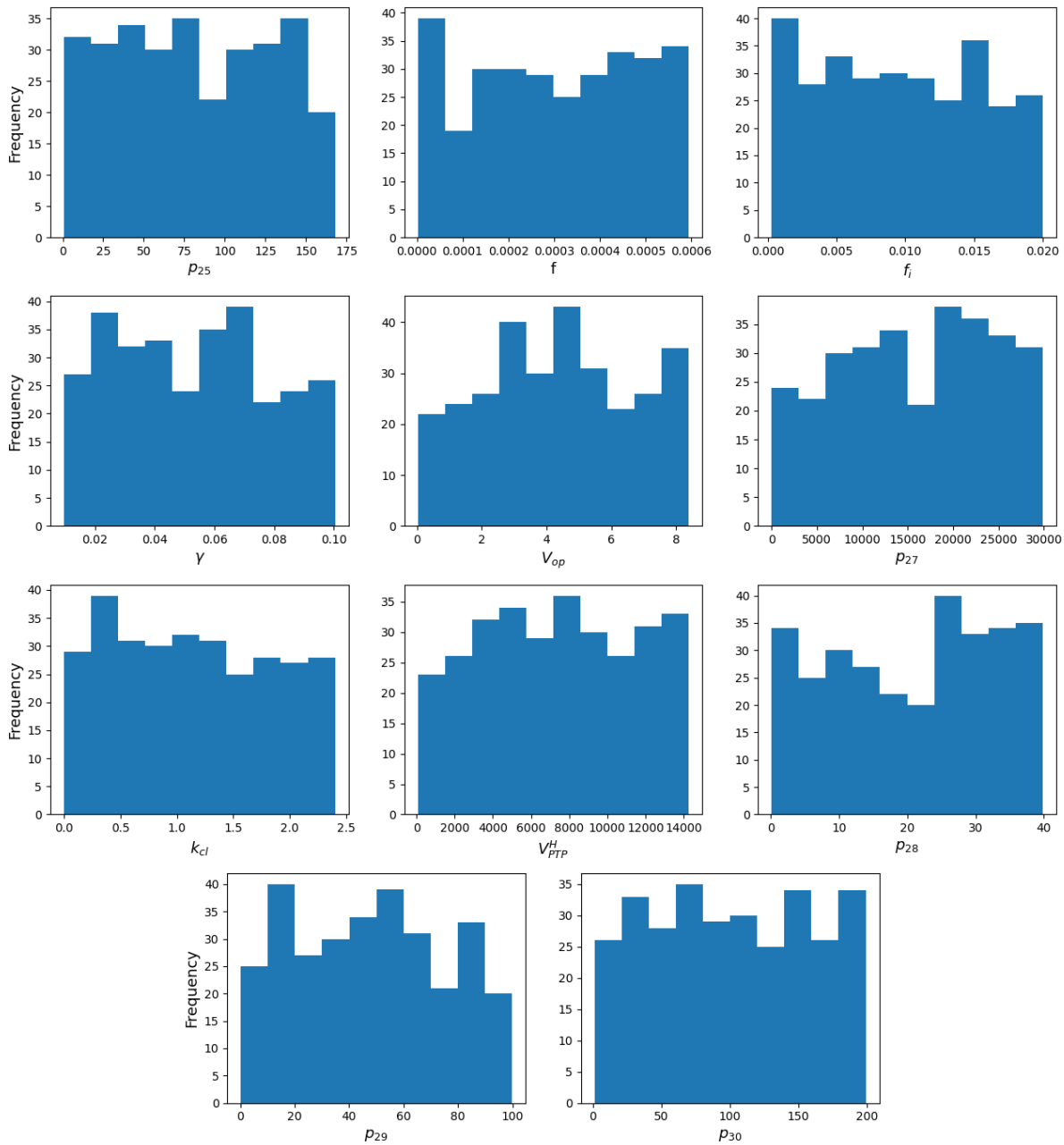

Figure 7.8: The computed distributions of eleven parameters using the maximum likelihood algorithm show quasi-uniform distributions. More details in the discussion section 7.4.

either to calcium exchange, mPTP or ROS. That is because the mPTP is mainly regulated via related mechanisms.

Next, we used machine learning supervised classification algorithms to constructed meta-models that are able to mimic the original model and its associated classification (using the previously discussed classifier). These meta-models will behave as a black box that is able to classify the mPTP opening type with respect to the given parameters (features), without going through the burden of solving the differential equation system. This is crucial since algorithms that perform parameter inference require normally a huge number of model evaluations, which would not be feasible via the classical model that takes $\sim$ 100 sec for a single model simulation. The chosen meta-model (decision tree) is able to reproduce the classification of the original model with 84.2% accuracy.

Here also we should note that the sensitivity analysis we performed before the use of machine learning classification algorithms was useful because it permitted us to optimize the performance of the tested meta-models. This is because supervised classification algorithms tend to perform better when the features of the model are reduced to an optimal number. Including only the influential parameters as features for the classification algorithms guarantees that the output classes are well described by the features and thus the algorithm performance increases. However, we are aware that there is probably room for more improvements in the use of the classification algorithms. This could either be by trying different algorithms from the ones we tested, or by optimizing the performance of the used algorithms.

Finally, using the chosen meta-model, we performed parameter inference using an iterative maximum likelihood algorithm. The algorithm returns the posterior distributions of the eleven parameters in question. Model classifications computed from random draws of these distributions reproduce almost the same variability found in the experimental data. However, the quasi-uniform shapes of the returned distributions (Fig. 7.8) are not very reassuring. This is because normally parameters corresponding to biological phenomenon tend to present modality or normality in their distributions.

The quasi-uniform shapes of the computed distributions could be principally due to three reasons. Two of these reasons could be related to the experimental data. The first reason could

be that the mPTP opening type characterization done by our collaborators was not revised, and a possible classification errors or biases could be the cause of a misleading data.

The second reason could be our use of a very reduced form of the data to infer a big number of the model parameters. Indeed, in the parameter inference we performed, the data on the mPTP opening type used is represented by one scalar. This scalar is the ratio between the number of events resulting in a type-1 and type-3 mPTP opening 7.2. Thus inferring using this reduced form of data could so probably be the reason behind the uninformative computed distributions.

The third possible cause could be the data wrangling assumptions we took in section 7.2. That is because, as explained in section 7.2, the poor understanding of type-2 experimental mPTP opening, and the non existence of a correspondent simulated type led us to eliminate data coming from mitochondria that exhibited this particular type. However, this experimental type-2 opening may eventually be a sub type of the other possible mPTP opening types, and thus eliminating it from the data could be misleading.

On the other hand, we should not eliminate the possibility that the true distributions of the parameters in question be the ones plotted in Fig. 7.8. This could be caused by the important heterogeneity in individual mitochondria.

Conclusion and perspectives

The constructed mitochondrial model proposed in this work, is calibrated for respiration experimental data of a population of cardiac mitochondria. Indeed, it was able to reproduce, up to a certain degree, the experimental data on oxygen consumption by population of mitochondria in their different energetic states.

However, the parameters calibration using data for calcium induced mPTP opening, for individual mitochondrion, was probably not successful due to several possible causes discussed in section 7.4. Indeed, as discussed previously, a very possible cause may be that the data we used for inferring parameters related to the mPTP opening, is hugely reduced to one scalar. This is why we are currently working on a more in depth exploration of this data. More practically, we want to use more from this data by trying to extract more features (*e.g.* $\Delta\psi$ depolarization amplitudes, recovery time to reach baseline, ..) from the fluorescence times series of the individual mitochondria (see section 6.5). Incorporating these features in the parameters inferring algorithm could be helpful to compute the adequate desired parameters distributions.

Moreover, the fact that not all of the model parameters are being calibrated in a one go, is not a problem. That is because the sensitivity analysis we performed, on the different components of the model (Fig. 7.3), shows that the parameters of the model tend to be grouped by blocks. Indeed, each block has influence on a component of the model. This is promising since eventual calibration of the remaining parameter could be possible if adequate data becomes available.

Overall, the utility of such model in itself is that it can be used to make predictions of mechanisms of interest related to mitochondrial respiration, or even to perform simulations of some unfeasible experiments of interest. The model guarantees, at least qualitatively, the ability

to represent population of cardiac mitochondria.

However, a relevant questioning might be on its ability to reproduce mechanisms unrelated or even weakly related to respiration. Indeed, even though the model parameters values are mostly taken from trusted literature, the sparsity of the experimental data used for parameters calibration leaves us with a model that is calibrated only for some of its components. Thus the quality of predictions, that are unrelated to these components, is yet to be confirmed.

On the other hand, another utility of this model, on the cellular level, might be in an eventual incorporation into ionic model of the cardiac cell. Indeed, besides the fact that ionic cardiac models do not account for the activity of the mitochondria, the ability of this model to reproduce qualitatively the activity of the mPTP could be a key player in the comprehension of several cardiac dysfunctions. This could be crucial, especially in the context of cardiac diseases related to energy deficit and/or pathological mPTP opening such as ischemia-reperfusion. Even if this work was not accomplished during this thesis for lack of time, the base ground for it was well established, and the derived model could be included in eventual more studies interested in this subject.

Finally, it could also be interesting to incorporate this model to cardiac excitation-contraction coupling models. Indeed, the fact that the proposed model includes ROS production and activation of the mPTP opening could be a key player in these excitation-contraction models. That is because the potential model could make it possible to explore the involvement of mitochondrial ROS and mPTP in the regulation of the excitation-contraction coupling in cardiomyocytes, under physiological and pathological conditions.

Bibliography

[1] M. J. Achs and D. Garfinkel. Metabolism of totally ischemic excised dog heart i. construction of a computer model. *American Journal of Physiology-Regulatory, Integrative and Comparative Physiology*, 237(5):R318–R326, 1979.

[2] J. N. Bazil, G. T. Buzzard, and A. E. Rundell. Modeling mitochondrial bioenergetics with integrated volume dynamics. *PLOS Computational Biology*, 6(1):e1000632, 2010.

[3] P. Bernardi, P. Veronese, and V. Petronilli. Modulation of the mitochondrial cyclosporin a-sensitive permeability transition pore. i. evidence for two separate me2+ binding sites with opposing effects on the pore open probability. *Journal of Biological Chemistry*, 268(2):1005–1010, 1993.

[4] D. M. Bers. Cardiac excitation–contraction coupling. *Nature*, 415(6868):198–205, 2002.

[5] R. Bertram, M. G. Pedersen, and A. Luciani, Dan S an d Sherman. A simplified model for mitochondrial ATP production. *Journal of Theoretical Biology*, 243(4):575–586, 2006.

[6] R. Bohnensack. Control of energy transformation in mitochondria. analysis by a quantitative model. *Biochimica et Biophysica Acta (BBA)-Bioenergetics*, 634:203–218, 1981.

[7] M. Bonora and P. Pinton. The mitochondrial permeability transition pore and cancer: molecular mechanisms involved in cell death. *Frontiers in oncology*, 4:302, 2014.

[8] M. D. Brand. The stoichiometry of the exchange catalysed by the mitochondrial calcium/sodium antiporter. *Biochemical Journal*, 229(1):161–166, 1985.

[9] M. D. Brand, L.-F. Chien, and P. Diolez. Experimental discrimination between proton leak and redox slip during mitochondrial electron transport. *Biochemical Journal*, 297 (Pt 1):27–29, 1994.

[10] G. C. Brown. The leaks and slips of bioenergetic membranes. *FASEB Journal*, 6(11):2961–2965, 1992.

[11] M. Carraro and P. Bernardi. Calcium and reactive oxygen species in regulation of the mitochondrial permeability transition and of programmed cell death in yeast. *Cell calcium*, 60(2):102–107, 2016.

[12] B. Chance and G. Williams. Respiratory enzymes in oxidative phosphorylation: III. The steady state. *Journal of Biological Chemistry*, 217(1):409–427, 1955.

[13] E. M. Chance. A computer simulation of oxidative phosphorylation. *Computers and Biomedical Research*, 1(3):251–264, 1967.

[14] X. Chapa-Dubocq, V. Makarov, and S. Javadov. Simple kinetic model of mitochondrial swelling in cardiac cells. *Journal of cellular physiology*, 233(7):5310–5321, 2018.

[15] J. Chappell and A. Crofts. Calcium ion accumulation and volume changes of isolated liver mitochondria. calcium ion-induced swelling. *Biochemical Journal*, 95(2):378–386, 1965.

[16] C. Colin. *Développement de nouvelles méthodes de microscopie et d'électrochimie pour des analyses multi-paramétriques de mitochondries individuelles cardiaques (in French)*. Theses, Université de Bordeaux, Oct. 2020.

[17] S. Cortassa, M. A. Aon, E. Marbân, R. L. Winslow, and B. O'Rourke. An integrated model of cardiac mitochondrial energy metabolism and calcium dynamics. *Biophysical Journal*, 84(4):2734–2755, 2003.

[18] S. Cortassa, M. A. Aon, R. L. Winslow, and B. O'Rourke. A mitochondrial oscillator dependent on reactive oxygen species. *Biophysical journal*, 87(3):2060–2073, 2004.

[19] F. M.-P. de Gannes, N. Leducq, P. Diolez, F. Belloc, M. Merle, P. Canioni, and P.-J. Voisin. Mitochondrial impairment and recovery after heat shock treatment in a human microglial cell line. *Neurochemistry international*, 36(3):233–241, 2000.

[20] R. M. Denton, D. A. Richards, and J. G. Chin. Calcium ions and the regulation of nad+-linked isocitrate dehydrogenase from the mitochondria of rat heart and other tissues. *Biochemical Journal*, 176(3):899–906, 1978.

[21] C. O. Diekman, C. P. Fall, J. D. Lechleiter, and D. Terman. Modeling the neuroprotective role of enhanced astrocyte mitochondrial metabolism during stroke. *Biophysical journal*, 104(8):1752–1763, 2013.

[22] P. Diolez, V. Deschodt-Arsac, G. Calmettes, G. Gouspillou, L. Arsac, P. Dos Santos, P. Jais, and M. Haissaguerre. Integrative methods for studying cardiac energetics. *Mitochondrial Medicine*, pages 289–303, 2015.

[23] P. Diolez, V. Deschodt-Arsac, G. Raffard, C. Simon, P. D. Santos, E. Thiaudiere, L. Arsac, and J.-M. Franconi. Modular regulation analysis of heart contraction: application to in situ demonstration of a direct mitochondrial activation by calcium in beating heart. *American Journal of Physiology-Regulatory, Integrative and Comparative Physiology*, 293(1):R13–R19, 2007.

[24] J. W. Elrod and J. D. Molkentin. Physiologic functions of cyclophilin d and the mitochondrial permeability transition pore. *Circulation Journal*, pages CJ–13, 2013.

[25] J. W. Elrod, R. Wong, S. Mishra, R. J. Vagnozzi, B. Sakthievel, S. A. Goonasekera, J. Karch, S. Gabel, J. Farber, T. Force, et al. Cyclophilin d controls mitochondrial pore–dependent ca 2+ exchange, metabolic flexibility, and propensity for heart failure in mice. *The Journal of clinical investigation*, 120(10):3680–3687, 2010.

[26] N. Fournier, G. Ducet, and A. Crevat. Action of cyclosporine on mitochondrial calcium fluxes. *Journal of bioenergetics and biomembranes*, 19(3):297–303, 1987.

[27] A. Gelman, J. B. Carlin, H. S. Stern, and D. B. Rubin. *Bayesian data analysis*. Chapman and Hall/CRC, 1995.

[28] T. E. Gunter and D. R. Pfeiffer. Mechanisms by which mitochondria transport calcium. *American Journal of Physiology-Cell Physiology*, 258(5):C755–C786, 1990.

[29] C. R. Hackenbrock and A. I. Caplan. Ion-induced ultrastructural transformations in isolated mitochondria: The energized uptake of calcium. *The Journal of cell biology*, 42(1):221–234, 1969.

[30] A. P. Halestrap. A pore way to die: the role of mitochondria in reperfusion injury and cardioprotection. *Biochemical Society Transactions*, 38(4):841–860, 2010.

[31] A. P. Halestrap, S. J. Clarke, and S. A. Javadov. Mitochondrial permeability transition pore opening during myocardial reperfusion—a target for cardioprotection. *Cardiovascular research*, 61(3):372–385, 2004.

[32] A. P. Halestrap and P. Pasdois. The role of the mitochondrial permeability transition pore in heart disease. *Biochimica et Biophysica Acta (BBA)-Bioenergetics*, 1787(11):1402–1415, 2009.

[33] A. P. Halestrap, K.-Y. Woodfield, and C. P. Connern. Oxidative stress, thiol reagents, and membrane potential modulate the mitochondrial permeability transition by affecting nucleotide binding to the adenine nucleotide translocase. *Journal of Biological Chemistry*, 272(6):3346–3354, 1997.

[34] J. Herman and W. Usher. SALib: An open-source Python library for Sensitivity Analysis. *Journal of Open Source Software*, 2(9), jan 2017.

[35] T. L. Hill. *Free energy transduction in biology: the steady-state kinetic and thermodynamic formalism*. Academic Press, 1977.

[36] C. J. Holloway, S. Dass, J. J. Suttie, O. J. Rider, P. Cox, L. E. Cochlin, H. Jackson, A. M. Fast, A. W. Johnson, T. D. Karamitsos, et al. Exercise training in dilated cardiomyopathy

improves rest and stress cardiac function without changes in cardiac high energy phosphate metabolism. *Heart*, 98(14):1083–1090, 2012.

[37] D. R. Hunter, R. Haworth, and J. Southard. Relationship between configuration, function, and permeability in calcium-treated mitochondria. *Journal of Biological Chemistry*, 251(16):5069–5077, 1976.

[38] D. R. Hunter and R. A. Haworth. The ca2+-induced membrane transition in mitochondria: I. the protective mechanisms. *Archives of biochemistry and biophysics*, 195(2):453–459, 1979.

[39] S. Hurst, J. Hoek, and S.-S. Sheu. Mitochondrial ca 2+ and regulation of the permeability transition pore. *Journal of bioenergetics and biomembranes*, 49(1):27–47, 2017.

[40] M. S. Jafri and R. Kumar. Modeling mitochondrial function and its role in disease. *Progress in molecular biology and translational science*, 123:103–125, 2014.

[41] M.-J. Jou. Melatonin preserves the transient mitochondrial permeability transition for protection during mitochondrial ca2+ stress in astrocyte. *Journal of pineal research*, 50(4):427–435, 2011.

[42] K. W. Kinnally, M. L. Campo, and H. Tedeschi. Mitochondrial channel activity studied by patch-clamping mitoplasts. *Journal of bioenergetics and biomembranes*, 21(4):497–506, 1989.

[43] A. C. Köhler, C. M. Sag, and L. S. Maier. Reactive oxygen species and excitation–contraction coupling in the context of cardiac pathology. *Journal of molecular and cellular cardiology*, 73:92–102, 2014.

[44] B. Korzeniewski and W. Froncisz. An extended dynamic model of oxidative phosphorylation. *Biochimica et Biophysica Acta (BBA)-Bioenergetics*, 1060(2):210–223, 1991.

[45] G. Krishnamoorthy and P. C. Hinkle. Non-ohmic proton conductance of mitochondria and liposomes. *Biochemistry*, 23(8):1640–1645, 1984.

[46] Y. Kushnareva, A. N. Murphy, and A. Andreyev. Complex i-mediated reactive oxygen species generation: modulation by cytochrome c and nad (p)+ oxidation–reduction state. *Biochemical Journal*, 368(2):545–553, 2002.

[47] J. Q. Kwong and J. D. Molkentin. Physiological and pathological roles of the mitochondrial permeability transition pore in the heart. *Cell metabolism*, 21(2):206–214, 2015.

[48] N. Leducq, M.-C. Delmas-Beauvieux, I. Bourdel-Marchasson, S. Dufour, J.-L. Gallis, P. Canioni, and P. Diolez. Mitochondrial permeability transition during hypothermic to normothermic reperfusion in rat liver demonstrated by the protective effect of cyclosporin a. *Biochemical Journal*, 336(2):501–506, 1998.

[49] A. L. Lehninger. Reversal of various types of mitochondrial swelling by adenosine triphosphate. *Journal of Biological Chemistry*, 234(9):2465–2471, 1959.

[50] X. Lu, J. Q. Kwong, J. D. Molkentin, and D. M. Bers. Individual cardiac mitochondria undergo rare transient permeability transition pore openings. *Circulation research*, 118(5):834–841, 2016.

[51] G. Magnus and J. Keizer. Minimal model of β-cell mitochondrial Ca^{2+} handling. *American Journal of Physiology-Cell Physiology*, 273(2):C717–C733, 1997.

[52] G. Magnus and J. Keizer. Model of β-cell mitochondrial calcium handling and electrical activity. I. Cytoplasmic variables. *American Journal of Physiology-Cell Physiology*, 274(4):C1158–C1173, 1998.

[53] T. Matsuda, K. Takuma, and A. Baba. Na^{+}-Ca^{2+} exchanger: physiology and pharmacology. *Japanese Journal of Pharmacology*, 74(1):1–20, 1997.

[54] J. G. McCORMACK and R. M. Denton. The effects of calcium ions and adenine nucleotides on the activity of pig heart 2-oxoglutarate dehydrogenase complex. *Biochemical Journal*, 180(3):533–544, 1979.

[55] C. C. Mitchell and D. G. Schaeffer. A two-current model for the dynamics of cardiac membrane. *Bulletin of Mathematical Biology*, 65(5):767–793, 2003.

[56] S. Neubauer, H. Remkes, M. Spindler, M. Horn, F. Wiesmann, J. Prestle, B. Walzel, G. Ertl, G. Hasenfuss, and T. Wallimann. Downregulation of the na+-creatine cotransporter in failing human myocardium and in experimental heart failure. *Circulation*, 100(18):1847–1850, 1999.

[57] I. I. Nita, M. Hershfinkel, D. Fishman, E. Ozeri, G. A. Rutter, S. L. Sensi, D. Khananshvili, E. C. Lewis, and I. Sekler. The mitochondrial na+/ca 2+ exchanger upregulates glucose dependent ca 2+ signalling linked to insulin secretion. *PLOS One*, 7(10):e46649, 2012.

[58] G. Olivetti, E. Cigola, R. Maestri, D. Corradi, C. Lagrasta, S. R. Gambert, and P. Anversa. Aging, cardiac hypertrophy and ischemic cardiomyopathy do not affect the proportion of mononucleated and multinucleated myocytes in the human heart. *Journal of molecular and cellular cardiology*, 28(7):1463–1477, 1996.

[59] C. M. Palmeira and A. J. Moreno, editors. *Mitochondrial Bioenergetics*, volume 1782 of *Methods in Molecular Biology*. Humana Press, 2008.

[60] R. Palty, W. F. Silverman, M. Hershfinkel, T. Caporale, S. L. Sensi, J. Parnis, C. Nolte, D. Fishman, V. Shoshan-Barmatz, S. Herrmann, et al. Nclx is an essential component of mitochondrial na+/ca2+ exchange. *Proceedings of the National Academy of Sciences*, 107(1):436–441, 2010.

[61] G. Paradies, V. Paradies, F. M. Ruggiero, and G. Petrosillo. Mitochondrial bioenergetics and cardiolipin alterations in myocardial ischemia-reperfusion injury: implications for pharmacological cardioprotection. *American Journal of Physiology-Heart and Circulatory Physiology*, 315(5):H1341–H1352, 2018.

[62] F. Pedregosa, G. Varoquaux, A. Gramfort, V. Michel, B. Thirion, O. Grisel, M. Blondel, P. Prettenhofer, R. Weiss, V. Dubourg, J. Vanderplas, A. Passos, D. Cournapeau,

M. Brucher, M. Perrot, and E. Duchesnay. Scikit-learn: Machine learning in Python. *Journal of Machine Learning Research*, 12:2825–2830, 2011.

[63] V. Petronilli, G. Miotto, M. Canton, M. Brini, R. Colonna, P. Bernardi, and F. Di Lisa. Transient and long-lasting openings of the mitochondrial permeability transition pore can be monitored directly in intact cells by changes in mitochondrial calcein fluorescence. *Biophysical journal*, 76(2):725–734, 1999.

[64] D. Pietrobon and S. R. Caplan. Flow-force relationships for a six-state proton pump model: int rinsic uncoupling, kinetic equivalence of input and output forces, and domain o f approximate linearity. *Biochemistry*, 24(21):5764–5776, 1985.

[65] A. V. Pokhilko, F. I. Ataullakhanov, and E. L. Holmuhamedov. Mathematical model of mitochondrial ionic homeostasis: three modes of ca2+ transport. *Journal of theoretical biology*, 243(1):152–169, 2006.

[66] A. Saa and K. M. Siqueira. Modeling the atp production in mitochondria. *Bulletin of Mathematical Biology*, 75(9):1636–1651, 2013.

[67] A. Saltelli, M. Ratto, T. Andres, F. Campolongo, J. Cariboni, D. Gatelli, M. Saisana, and S. Tarantola. *Global sensitivity analysis: the primer*. John Wiley & Sons, 2008.

[68] J. Schmitz, J. Vanlier, N. van Riel, and J. A. Jeneson. Computational modeling of mitochondrial energy transduction. *Critical Reviews™ in Biomedical Engineering*, 39(5), 2011.

[69] V. A. Selivanov, F. Ichas, E. L. Holmuhamedov, L. S. Jouaville, Y. V. Evtodienko, and J.-P. Mazat. A model of mitochondrial ca2+-induced ca2+ release simulating the ca2+ oscillations and spikes generated by mitochondria. *Biophysical chemistry*, 72(1-2):111–121, 1998.

[70] A. I. Tarasov, F. Semplici, M. A. Ravier, E. A. Bellomo, T. J. Pullen, P. Gilon, I. Sekler, R. Rizzuto, and G. A. Rutter. The mitochondrial ca 2+ uniporter mcu is essential for glucose-induced atp increases in pancreatic β-cells. *PLOS one*, 7(7):e39722, 2012.

[71] B. Tarraf, E. Suraniti, C. Colin, S. Arbault, P. Diolez, M. Leguèbe, and Y. Coudière. A simple model of cardiac mitochondrial respiration with experimental validation. *Mathematical Biosciences and Engineering*, 18(5):5758–5789, 2021.

[72] K. H. ten Tusscher and A. V. Panfilov. Alternans and spiral breakup in a human ventricular tissue model. *American Journal of Physiology-Heart and Circulatory Physiology*, 291(3):H1088–1100, 2006.

[73] E. Theakston, C. Walker, M. O'Sullivan, and V. Rajagopal. Stochastic modelling of cardiac cell structure. In *2010 Annual International Conference of the IEEE Engineering in Medicine and Biology*, pages 3257–3260. IEEE, 2010.

[74] H. Vainio, L. Mela, and B. Chance. Energy dependent bivalent cation translocation in rat liver mitochondria. *European journal of biochemistry*, 12(2):387–391, 1970.

[75] B. Wacquier, L. Combettes, and G. Dupont. Dual dynamics of mitochondrial permeability transition pore opening. *Scientific reports*, 10(1):1–10, 2020.

[76] L. Wei-LaPierre and R. T. Dirksen. Isolating a reverse-mode atp synthase–dependent mechanism of mitoflash activation. *Journal of General Physiology*, 151(6):708–713, 2019.

[77] D. E. Wingrove and T. Gunter. Kinetics of mitochondrial calcium transport. I. Characteristics of the sodium-independent calcium efflux mechanism of liver mitochondria. *Journal of Biological Chemistry*, 261(32):15159–15165, 1986. PMID: 3771569.

[78] R. Wong, C. Steenbergen, and E. Murphy. Mitochondrial permeability transition pore and calcium handling. In *Mitochondrial Bioenergetics*, pages 235–242. Springer, 2012.

[79] F. Wu, F. Yang, K. Vinnakota, and D. Beard. Computer modeling of mitochondrial tricarboxylic acid cycle, oxidative phosphorylation, metabolite transport, and electrophysiology. *J. Biol. Chem.*, 282(34):24525–24537, 2007.

[80] J. Xi, H. Wang, R. A. Mueller, E. A. Norfleet, and Z. Xu. Mechanism for resveratrol-induced cardioprotection against reperfusion injury involves glycogen synthase kinase 3β and mitochondrial permeability transition pore. *European journal of pharmacology*, 604(1-3):111–116, 2009.